Journal of Engineering

ISSN 1726-4073

A Scientific Refereed Journal
Published by College of
Engineering University of
Baghdad

March
٢٠١5

Number 3

Volume 21

مجلـــة الهندســــــــة

ISSN 1726-4073

مجلة علمية محكمة تصدرها
كلية الهندسة ـ جامعة بغداد

آذار

2015

العدد ٣

المجلد ٢١

ENGINEERING

College of Engineering University of Baghdad Baghdad

List of Contents

English Section: Page

Experimental Study of Interior Temperature Distribution Inside Parked Automobile Cabin 1 -10
Issam Mohammed Ali Aljubury
Ammar Ali Farhan
Munther Abdullah Mussa

Finite Element Investigation on Shear Lag in Composite Concrete-Steel Beams with Web Openings 11 – 33
Dr. Rafa'a Mahmood Abbas
Hayder Jaber Shakir

Retrofitting of Reinforced Concrete Damaged Short Column Exposed to High Temperature 34 -53
Asst. Prof. Dr. Amer Farouk Izzat

Multi-Sites Multi-Variables Forecasting Model for Hydrological Data using Genetic Algorithm Modeling 54 – 72
Prof. Dr. Rafa H. Al-Suhili

Scheduling of Irrigation and Leaching Requirements 73 - 92
Amer Hassan Al-haddad
Alaa Ibraheem Badi Al-Safi

Effect of Initial Water Content on the Properties of Compacted Expansive Unsaturated Soil 93 - 108
Mohammed Yousif Fattah
Aysar Hassan Al-Lami
Mahmood D. Ahmed

Bearing Capacity of Bored Pile Model Constructed in Gypseous Soil 109 - 128
Asst. Prof. Bushra Suhale Al-Busoda
Asst. Lect. Asmaa Hasan Al-Rubaye

Treatment of Furfural Wastewater by (AOPs) Photo-Fenton Method 129 - 141
Dr. Yasmen A. Mustafa
Raid Raho Omran

Digital Orthophoto Production Using Close-Range Photographs for High Curved Objects 142 – 157
Fanar Mansour Abed

قـائـمـة الـمـحـتـويـات

القسم العربي:

العنوان	الصفحة
إعادة تأهيل الأبنية الآثارية و التاريخية و التراثية	**١- 23**
إستراتيجة المشروع الرائد في إعادة تأهيل الأبنية التاريخية و التراثية *أ.د. غادة موسى رزوقي السلق* *هــديـــر أديـب عباس الشامـــي*	

Experimental Study of Interior Temperature Distribution Inside Parked Automobile Cabin

Issam Mohammed Ali Aljubury
Instructor
Mech. Eng. Dept.
Eng. Coll. - Baghdad Univ.
juburyima@gmail.com

Ammar Ali Farhan
Instructor
Mech. Eng. Dept.
Eng. Coll. - Baghdad Univ.
ammarali@uobaghdad.edu.iq

Munther Abdullah Mussa
Instructor
Mech. Eng. Dept.
Eng. Coll. - Baghdad Univ.
munthermech@yahoo.com

ABSTRACT

Temperature inside the vehicle cabin is very important to provide comfortable conditions to the car passengers. Temperature inside the cabin will be increased, when the car is left or parked directly under the sunlight. Experimental studies were performed in Baghdad, Iraq (33.3 ^{o}N, 44.4 ^{o}E) to investigate the effects of solar radiation on car cabin components (dashboard, steering wheel, seat, and inside air). The test vehicle was oriented to face south to ensure maximum (thermal) sun load on the front windscreen. Six different parking conditions were investigated. A suggested car cover was examined experimentally. The measurements were recorded for clear sky summer days started at 8 A.M. till 5 P.M. Results show that interior air temperature in unshaded parked car reaches 70^{o}C and dashboard temperature can approach 100 ^{o}C. While, cardboard car shade inside the car not reduce the air temperature inside it. Suggested car cover with 1 cm part-down side windows reduced temperature of cabin components by 70 % in average compare to the base case.

Key words: automobile cabin, temperature distribution, thermal comfort, greenhouse problem.

دراسة عملية لتوزيع درجات الحرارة داخل مقصورة سيارة متوقفة

عصام محمد علي الجبوري
مدرس
قسم الهندسة الميكانيكية
كلية الهندسة – جامعة بغداد

عمار علي فرحان
مدرس
قسم الهندسة الميكانيكية
كلية الهندسة – جامعة بغداد

منذر عبد الله موسى
مدرس
قسم الهندسة الميكانيكية
كلية الهندسة – جامعة بغداد

الخلاصة

تعتبر درجة الحرارة داخل مقصورة السيارة ضرورية لتوفير ظروف مريحة للركاب داخلها. تزداد درجة الحرارة داخل السيارة عندما تُترك متوقفة مباشرة تحت أشعة الشمس. أجريت دراسة تجريبية في مدينة بغداد، العراق (خط طول 44 وخط عرض 33) لمعرف تأثير الإشعاع الشمسي الساقط على مكونات السيارة الداخلية (لوحة القيادة، المقود، المقعد، الهواء الداخلي). وضعت سيارة الإختبار مواجهة لجهة الجنوب لضمان أقصى قدر من الإشعاع الشمسي الساقط على الزجاج الأمامي للسيارة وكذلك للحصول على أكبر حمل حراري داخل المقصورة.أختبرت ستة حالات مختلفة للسيارة المتوقفة. سُجلت القياسات لأيام الصيف والسماء صافية من الساعة 8 صباحاً وحتى الخامسة بعد الظهر. بينت النتائج أن درجة حرارة الهواء الداخلي في السيارة المتوقفة غير المظللة يصل 70 درجة مئوية وإقتربت درجة حرارة لوحة القيادة من 100 درجة مئوية . أما عند وضع واقية شمسية المصنعة من ورق الالمنيوم من داخل السيارة فإنها لم تقلل من درجة حرارة الهواء داخل المقصورة . وعند إستعمال غطاء السيارة

المقترح مع فتح الزجاج الجانبي 1 سم، فإنه ساهم في خفض درجة حرارة مكونات المقصورة بنسبة 70٪ مقارنة إلى الحالة الأساسية (سيارة مجردة وبدون أي غطاء).

الكلمات الرئيسية: مقصورة السيارة، توزيع درجات الحرارة، الراحة الحرارية، مشكلة الاحتباس الحراري.

1. INTRODUCTION

Recently, after 2003, the private passenger vehicles number in Iraq has been growing significantly. It's the most convenient means of transportation in the country. The high density of private passenger vehicles leads to lack of parking space. This is much clearer at the government offices, universities, and shopping areas. Moreover, the available shaded parking areas do not match the existing numbers of vehicles; hence the alternative choice for those who are unable to park under shaded area is to park in an open parking space.

Parking in an unshaded area gave rise of greenhouse problem. It is the problem of conversion of solar radiation entering through the windows of a car into long wave thermal radiation and trapped inside car cabin causes temperature increase of cabin components. Thereby, use of cardboard car shades to reduce the interior temperatures inside parked automobile has become popular in Baghdad and other hot regions in Iraq.

Temperature inside the vehicle cabin is very important to provide comfortness to the car passenger. The temperature can be controlled by using air conditioning system that can be operated when the car engine is in operation. However, when the car is left or parked directly under the sunlight, temperature inside the cabin will be increased. Sealed automobiles commonly encounter interior temperature conditions that are tremendously uncomfortable to the passengers.

The cabin temperature of unshaded parked car can quickly rise to a level that may damage property and harm children or pets left in the car. According to the findings of **Saidur, et al., 2008** in USA, every year many children die of (hyperthermia) heatstroke after being left unattended in vehicles. Hyperthermia is an acute condition that occurs when the body absorbs more heat than it can handle. Annually, hundreds of children experience varying degrees of heat illness from being left in cars. Similar experimental studies carried out in Australia show that rising air temperature +20 ^{o}C inside a parked car compared to the outside temperature on a hot summer day for periods of the order 30 minutes, children or pets left in such a parked car suffer heat stress and a number of deaths ,**Dadour, et al., 2011**.

Many car users are faced a hot interior after a certain hours of parking in open space or unshaded parking area. The heat under such parking conditions causes the car cabin and interior temperature to reach up to 80 ^{o}C average. The accumulation of thermal energy inside the vehicle with undesired temperature rise would cause the interior parts to degrade because they normally are subjected to wear and tear. Degradation may shorten the life span of the various components inside the car, especially electronic devices. Passengers are also being affected with the thermal condition inside the vehicle itself. The car user is forced to wait for a period of time around 2 – 5 minutes before getting into car to let the interior condition cool down either by rolling the window or running the air conditioner system (A/C) at high speed that really affect the fuel consumption ,**Al-Keyiem, et al.,2010**. The increased of fuel consumption by the A/C system subsequently increased CO_2 emissions , **Jasni** and **Nasir, 2012**.

,Abd-Fadeel and **Hassanein, 2013,** showed that the opening window about 1 – 3 cm during one hour, from 12 P.M. to 1 P.M. reduced the temperature inside the car because the flow rate of fresh air entering the car insufficient and its velocity inside the car approximately neglected. Whereas, the inside car sunshade reduces the temperature at front dashboard by about 40 – 60 ^{o}C compared with closed car. **Al-Kayiem, et al., 2010,** showed that, the effect of sunshades application to the interior windshield on the temperature was significant during six hours of parking time from 9 A.M. to 4 P.M. The maximum dashboard temperature of the parked vehicle with sunshade was found to be 25 ^{o}C lower than the other vehicle without any shades.

The objective of this research is to determine the most technically feasible passive method in reducing the car interior temperature. Six cases were experimentally studied: unshaded, partial shaded (inside and outside), total shaded (shelter and novel cap), and windows part-down by 1 cm. The obtained improvements from suggesting method were increasing in passenger comfort and less thermal stress on car interior components. Also, lower initial automobile air conditioner loads and reduction in fuel consumption and CO_2 emissions.

2. EXPERIMENTAL SETUP (MATERIALS AND METHODS)

2.1 Experimental Procedure: The car was parked in an open parking space and care was taken such that there was no interference from local shadows during the measurements. It was located in the same place and same orientation during the entire experimental measurements so as to obtain consistency during experiments, as in **Fig. 1** Experimental were performed in Baghdad, Iraq (33.3 ^{o}N, 44.4 ^{o}E). The test vehicle was oriented to face south to ensure maximum sun load on the front windscreen. The vehicle chosen in this study was 2000 cc, Daewoo car, 1997. There were no modifications done on the chosen car, and all the factory settings were retained all throughout the experiments.

2.2 Experimental Methodology: Six different parking conditions were investigated consisting of closed and opened glass windows, inside and outside front shield shading and normal parking conditions. The cases are described in **Table 1**. The temperature variation at four places inside the car cabin is measured. Four places are front dashboard, front seats, steering wheel, and inside air. The temperatures were measured by thermocouple wire type K in junction with 12 channel data logger. Only 10 channels were used for the cabin interior surfaces (2 measuring points for dashboard, front sets and 1 for steering wheel), cabin air (4 measuring points) and ambient (1 measuring point) temperatures. The measurements were recorded for clear sky summer days started at 8 A.M. till 5 P.M. and the data was recorded on 30 min. step interval. Hourly solar radiation was measured during the day with a Kipp and Zonen pyranometer model CMP22 having a measuring range of up to 4000 W m^{-2} (error < 5 W m^{-2}).

The suggested cover is consisted from many cardboard car shades which were sew with each other to make cap. A cap is covered the roof and windows of car only as shown in **Fig. 2.** Car windows and roof had the main effect on the car cabin temperature so that it is covered. The cardboard has 5 mm thickness with a silver foil front and back which is available in the markets. More benefits can be achieved from this suggested cover as compared with classical car cover made from leather or cloth. These benefits are: 1. Less in weight and small in size. 2. Cheap and easy to installation 3. Reflect solar radiation. 4. Thermal insulation.

3. RESULTS AND DISCUSSION

All methods of exploitation of solar energy required the knowledge of the average values of the intensity of solar radiation incident on the structure. The intensity of solar radiation on the car cabin in summer was measured with a Kipp and Zonen pyranometer model CMP22. The amount of irradiative heating in Baghdad from 5 A.M. to 7 P.M. in June is shown in **Fig. 3** It could be seen that irradiation increases with time to maximum values between 11 A.M. to 3 P.M. The maximum irradiance reading was 954 W/m^2 approximately at 1 P.M.

Fig. 4 presents the temperature variation of base case for front dashboard, steering wheel, seat, inside air, and ambient. The temperature of measuring points rises in the morning more rapidly than does the ambient. It is also observed that the temperature of these measuring points cools in the afternoon more rapidly than does the ambient. Solar radiation absorptance by the cabin components and greenhouse effects behind the rapidly increase of cabin temperature in the morning. At noon, these measuring reach its maximum temperature due to the maximum value of solar radiation occurs at this time. Dashboard has the maximum temperature between the cabin's components due to the largest projected area of glass is facing to the sun's rays. The maximum temperature of dashboard, inside air, seat, and ambient recorded in June were 99 ^{o}C, 70 ^{o}C, 68 ^{o}C and 44 ^{o}C, respectively. The experimental results of ,**Abd-Fadeel,** and **Hassanein, 2013.** for the dashboard temperature inside unshaded parked car are compared with the present study was shown in **Fig. 5** The behavior of the two curves is in good agreement but, the average percentage error about 20 % was occurred due to the different measured values of solar radiation.

Since experimental tests for the six cases done during different days, and in order to make comparison between these cases, the reductions in maximum temperature of measuring points (dashboard, steering wheel, seat, and inside air) minus ambient temperature are used. The reductions in maximum temperature of measuring points minus ambient temperature are presented in **Table 2.** and **Fig. 6** The maximum temperature difference is recorded at the dashboard (T_D – T_a), which can reach a maximum value of 58^{o}C at noon. At this location, it can be seen that shading application (case # 5 and # 6 in **Table 1.**) are the most effective methods in reducing the dashboard temperature difference from base case by much as 39.2 ^{o}C and 54.4 ^{o}C, respectively as shown in **Fig. 7** and **Table 2**. Also there is a reducing in the temperature at the steering wheel by as much as 51^{o}C and 44.2^{o}C. This could be due to the blockage of a large amount of sun radiation entering the car cabin by the cardboard sun shades. On the other hand, the seat temperature change in case #5 experiment have a significant difference from the base case and it reduces by as much as 17.9 ^{o}C.

The effect of shading and part-down the two side windows by 1 cm on hot days in June was shown in **Fig.8.** It is observed that inside shade (case # 2) had no effect on the inside air temperature due to the greenhouse effect occurs inside car cabin. On other hand, outside shading (case # 4) reduced the inside air temperature by 40 % from the base case. The combination of outside shading and windows part-down by 1 cm (case # 5 and # 6) were observed to be reducing the inside air temperature from the base case by 58 % and 91 % respectively . In short, it can observed from table 2 that the outside shades with part-down by 1 cm the two side windows (case # 5 and # 6) had important effect in reducing the interior temperature. Because they have decreased the interior temperature by 27.2 ^{o}C and 17.2 ^{o}C from the base case, respectively.

4. CONCLUSIONS

The following conclusions were recorded from the experimental study:

1- Use the cardboard car shade from outside with part-down windows by 1 cm has achieved an overall good performance in reducing the average maximum temperature at all interior locations of the test car, with higher difference of reduction at dashboard, steering wheel, seat and inside air ambient locations

2- Interior air temperature in unshaded parked car in a hot climate such as Baghdad, reach 70 ^{o}C and dashboard temperature can approach 100^{o}C.

3- Use the cardboard car shade behind the car windshield reduced dashboard temperature by 40 % from the base case. While, it does not reduced the air temperature inside parked car.

4- Shelter with part-down side windows by 1 cm made car cabin temperature approximately equal to ambient temperature plus 3^{o}C in maximum.

5- The obtained results of case #5 enabled to confirm that the suggested car cover designed with part-down side windows is able to keep comfortable conditions in the car cabin. The average temperature values of cabin components (dashboard, steering wheel, seat, and inside air) were reduced by 70 % from the base case.

REFERENCES

- Abd-Fadeel, Waleed. A., and Hassanein, Soubhi. Ali., 2013, *Temperature Variations in a Parked Car Exposed to Direct Sun During Hot and Dry Climates*, International journal of automobile engineering research and development (IJAuERD), vol. 3, Issue I, 75-80.

- Al-Kayiem, Hussain. H., Sidik, M. Firdaus Bin M. and Munusammy, Yuganthira. R.A.L., 2010, *Study on the Thermal Accumulation and Distribution Inside a Parked Car Cabin*, American journal of applied sciences, 7(6),784-789.

- Dadour, I., Almanjahie, I., Fowkes, N., Grant Keady, and Vijayan, K., 2011, *Temperature Variations in a Parked Car*, Forensic science international, vol. I, no. 207, pp. 205-211.

- Jasni, M. A., and Nasir, F. M., 2012, *Experimental Comparison Study of the Passive Methods in Reducing Car Cabin Interior Temperature*, International conference of mechanical automobile and robotics engineering (ICMAR), Penang, Malaysia.

- Saidur, R., Sattar, M. A., and Masjuki, H. H., 2008, *Performance of an Improved Solar Car Ventilator*, International conference on sustainable development: Issues and prospects for the GMS, Kuala Lumpur, Malaysia, pp. 1-6.

NOMENCLATURE

T_a = ambient temperature, ^{o}C.

T_D = dashboard temperature, ^{o}C.

T_i = inside air temperature, ^{o}C.

T_{se} = seat temperature, ^{o}C.

T_{st} = steering wheel temperature, ^{o}C.

Table 1. Description of the experimental measurements cases.

Test case	Description
1	Unshaded car and all windows are closed (base case) without any temperature-reducing methods applied.
2	Shaded is placed under the front windshield and all windows are closed
3	Shaded is placed above the front windshield and all windows are closed
4	Shaded is placed above the front windshield and two side windows are part-down by 1 cm
5	Shaded is placed above all windows and two side windows are part-down by 1 cm (novel cap)
6	Shaded is placed above all windshield and all windows are part-down by 1 cm

Table 2. Reduction in maximum temperature of different locations.

Experiment	Reduction in maximum temperature of measuring points minus ambient temperature (^oC)			
	Dashboard	Steering wheel	Seat	Inside air
	T_D - T_a	T_{st} - T_a	T_{se} - T_a	T_i - T_a
Case # 1	58.0	53.7	27.4	29.9
Case # 2	34.2	28.3	23.4	30.0
Case # 3	19.1	22.1	21.3	24.7
Case # 4	15.8	17.6	16.4	18.1
Case # 5	10.8	9.5	9.5	12.7
Case # 6	3.6	2.7	1.6	2.7

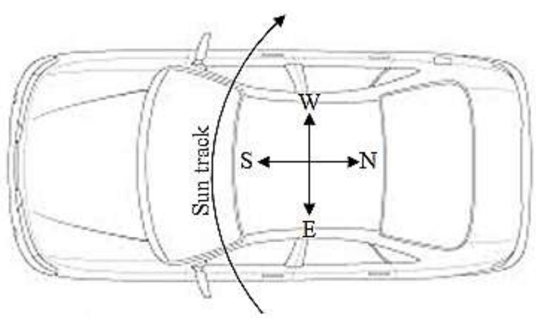

Figure 1. The car orientation during the measurements.

Figure 2. Suggested car cover.

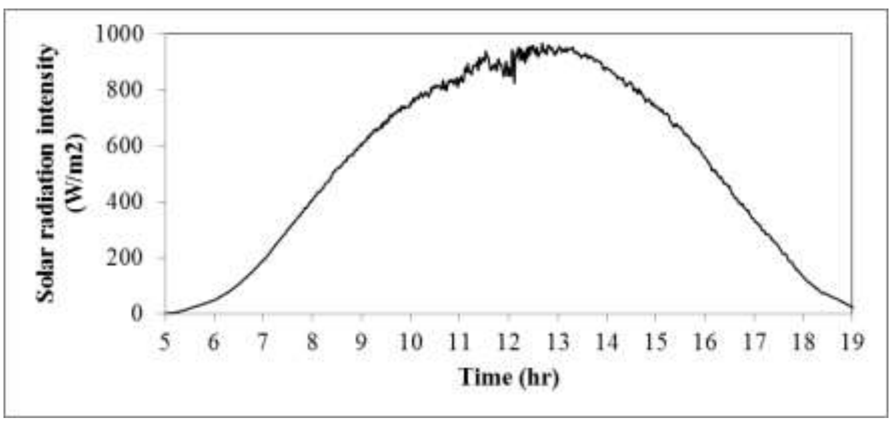

Figure 3. Measured values of solar radiation on the horizontal surface on, 11-6-2014 for clear sky.

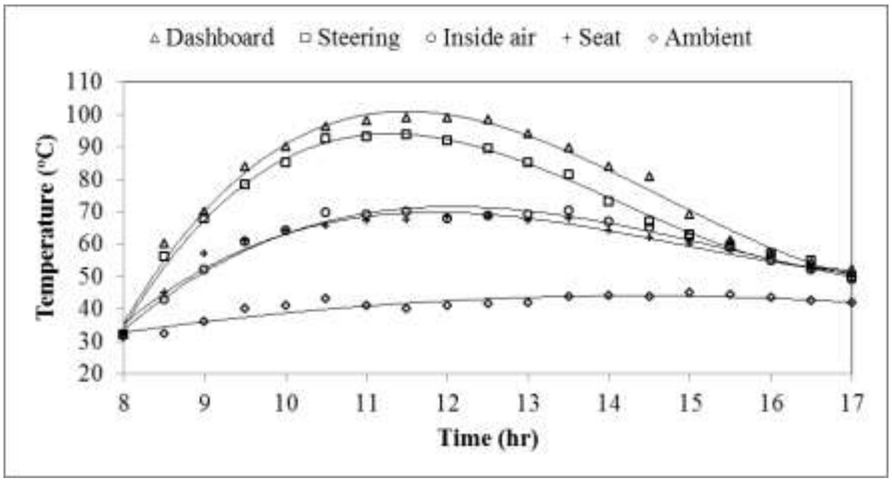

Figure 4. Temperature variations in an unshaded parked car in June.

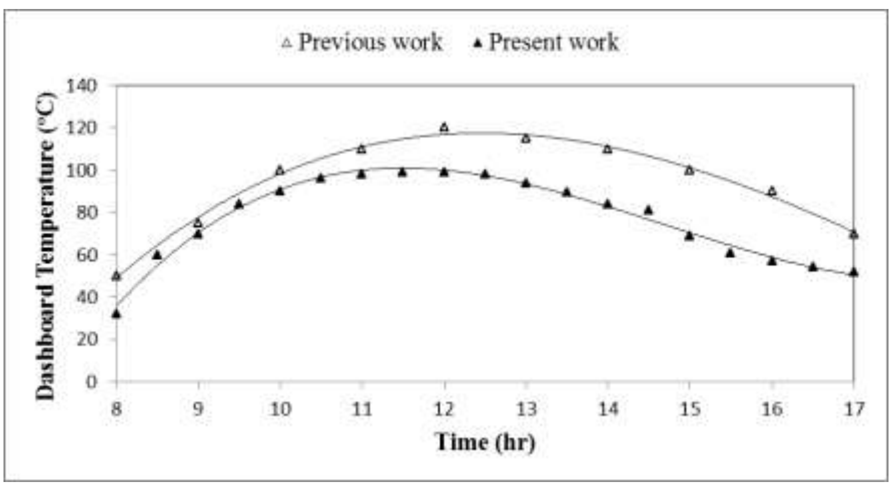

Figure 5. Comparison between present measured dashboard temperature with results measured by ,**Abd-Fadeel,** and **Hassanein, 2013**.

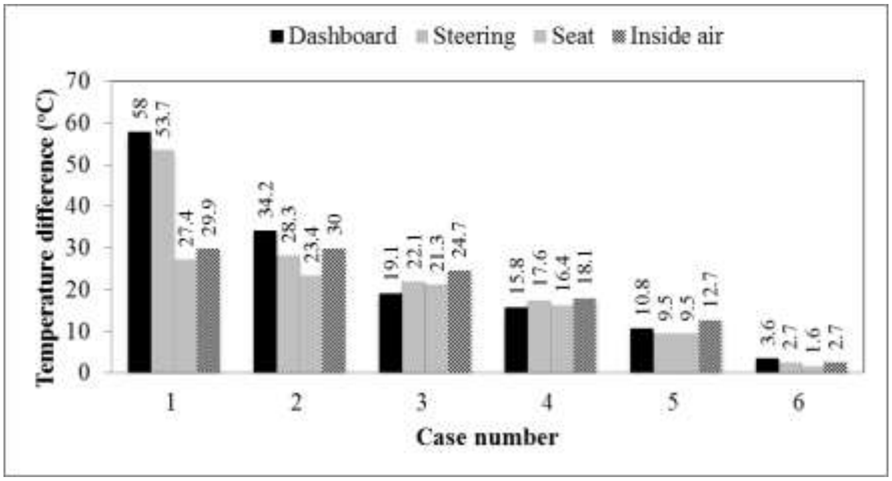

Figure 6. Reduction in maximum temperature of different locations.

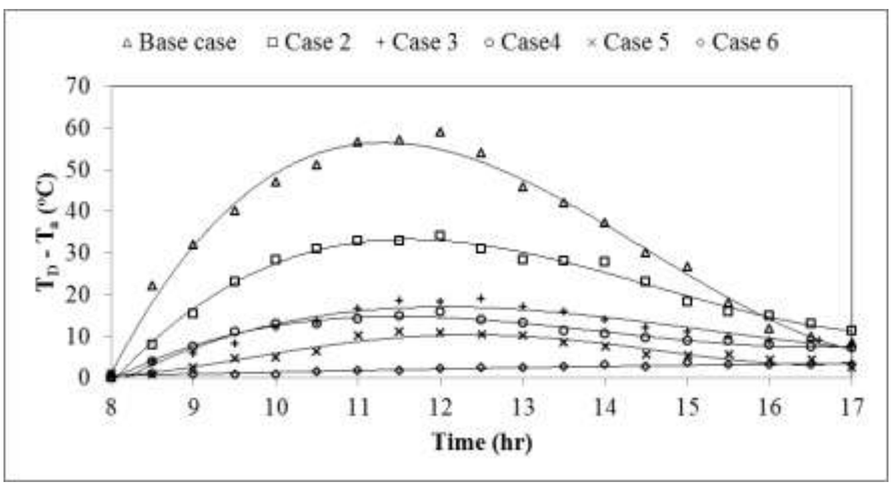

Figure 7. Comparison between temperatures differences for different cases in June.

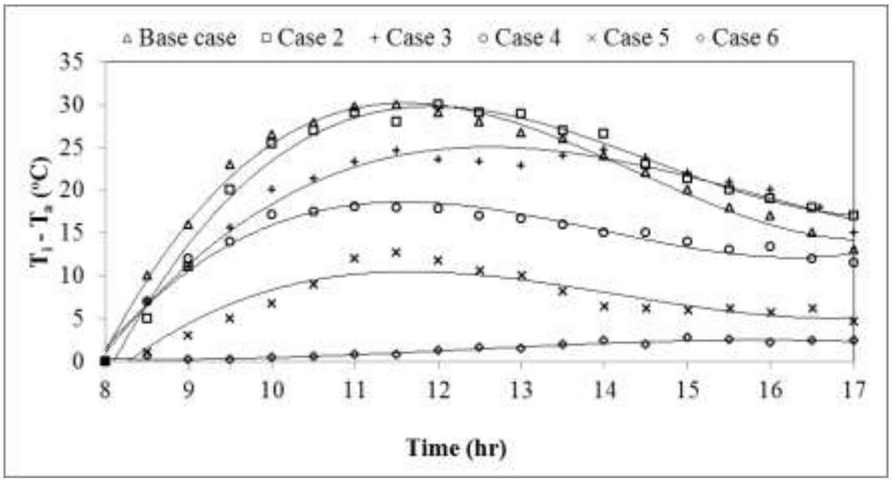

Figure 8. Comparison between temperatures differences for different cases in June.

Finite Element Investigation on Shear Lag in Composite Concrete-Steel Beams with Web Openings

Dr. Rafa'a Mahmood Abbas
Lecturer
College of Engineering-University of Baghdad
rafaamaa@yahoo.com

Hayder Jaber Shakir
M.Sc. Student
College of Engineering-University of Baghdad
hayder_civil_1988@yahoo.com

ABSTRACT

In this paper, effective slab width for the composite beams is investigated with special emphasis on the effect of web openings. A three dimensional finite element analysis, by using finite element code ANSYS, is employed to investigate shear lag phenomenon and the resulting effective slab width adopted in the classical T-beam approach. According to case studies and comparison with limitations and rules stipulated by different standards and codes of practice it is found that web openings presence and panel proportion are the most critical factors affecting effective slab width, whereas concrete slab thickness and steel beam depth are less significant. The presence of web opening reduces effective slab width by about 21%. Concentrated load produces smaller effective slab width when compared with uniformly distributed and line loads. Generally, standard codes of practice overestimate effective slab width for concentrated load effect, while underestimate effective slab width for uniformly distributed and line load effect. Based on the data available, sets of empirical equations are developed to estimate the effective slab width in the composite beams with web openings to be used in the classical T-beam approach taking into account the key parameters investigated.

Key words: composite beam, shear lag, effective slab width, web openings, finite element

التحري بطريقة العناصر المحددة لتخلف القص في العتبات المركبة من الفولاذ والخرسانة بوجود فتحات في وترة الروافد الفولاذية

د.رافع محمود عباس
مدرس
كلية الهندسة-جامعة بغداد

حيدر جابر شاكر
طالب ماجستير
كلية الهندسة-جامعة بغداد

الخلاصة

تم في هذا البحث اجراء دراسة تاثير وجود الفتحات في وترة الروافد المركبة من الفولاذ والخرسانة على العرض الفعال للشفة الخرسانية. تم عمل نماذج ثلاثية الابعاد بطريقة العناصر المحددة, باستعمال برنامج التحليل الجاهز ANSYS, للتحقق من ظاهرة تخلف القص والعرض الفعال للشفة الخرسانية الناتج عنها. بينت نتائج هذه الدراسة والمقارنة مع متطلبات ومحددات المراجع والمدونات القياسية ان تاثير وجود فتحات في وترة الروافد الفولاذية ونسبة ابعاد البلاطة الخرسانية هي اهم العوامل المؤثرة على العرض الفعال للشفة الخرسانية وبدرجة اقل يؤثر سمك البلاطة الخرسانية وعمق الرافدة الفولاذية. ان وجود فتحات في وترة الروافد الفولاذية يقلل العرض الفعال بمقدار 21% وان العرض الفعال للشفة الخرسانية بسبب الاحمال المركزة هو اقل مما في حالة الاحمال المنتظمة او الاحمال الخطية. وبشكل عام, فان المدونات القياسية تبالغ في تقدير العرض الفعال الناتج عن الاحمال المركزة وتقلل من تقديره في حالة الاحمال المنتظمة او الاحمال الخطية. واستنادا الى البيانات

المتوفرة تم اقتراح علاقات رياضية مبسطة تساعد المصمم على احتساب العرض الفعال للبلاطة في العتبات المركبة ذات الفتحات بصورة مباشرة من خلال بعض المتغيرات التي تمت دراستها.

كلمات الرئيسية: العتبات المركبة، تخلف القص، عرض السقف الفعال، فتحات في وترة الروافد، تحليل العناصر المحددة

1. INTRODUCTION

A typical form of composite construction, such as a floor within a building or a bridge deck, consists of a slab connected to a number of parallel beams. It is valid in principle to divide the system into a series of T-beams, the slab width obtained from such a simple division may not be fully effective in resisting the compressive forces from bending. The transmission of shear from the connectors on top flange of the steel beam to the slab becomes less effective as the beam spacing increase. Higher shear is induced near the beam, but falls off towards the center line between two beams. Under the action of the axial compression and eccentric edge shear flows, the flange distorts and does not compress as assumed in simple beam theory with plane sections remaining plane. The amount of distortion depends on both the shape of the flange in plane and on the distribution of shear flow along its edge. A narrow flange distorts little and its behavior approximates what is assumed in simple beam theory. In contrast, the wide flanges distort seriously because the compression induced by the edge shears does not flow very far from the loaded edge, and much of each wide flange is ineffective. The decrease in flange compression away from the loaded edge due to shear distortion is called shear lag.

The longitudinal compressive stresses at top of the slab have a non-uniform distribution, as shown in **Fig.1**. In order that the T-beam approach can be used, a reduced value of the width of the slab, termed effective width, is therefore used in design and analysis. It is defined as that width of slab that, when acted on uniformly by the actual maximum stress, would have the same static equilibrium effects as the existing variable stress. The effective width is affected by various factors such as the type of loading, the boundary conditions at the supports, and the ratio of beam spacing to span.

Eq. (1) is generally used to calculate the effective slab width in composite beams , **Heins, 1976.**

$$2\overline{b} = \frac{2\int_0^b \sigma_z \, dx}{(\sigma_z)_{max}} \tag{1}$$

Where ($2\overline{b}$) is the effective width of the concrete slab, (b) is a half slab width, (σ_z) represents the normal stress in the longitudinal direction in the slab at top surface, and $(\sigma_z)_{max}$is the maximum normal stress between $0 \leq x \leq b$.

2. BACKGROUND

In **2003**, **Fragiacomo, and Amadio** performed experimental tests for the evaluation of the effective width for elastic and plastic analysis of steel-concrete composite beams with both cases of sagging and hogging bending moments. It was shown that for all specimens the effective width increases with the load, approaching the width of whole slab near the collapse. In zones of sagging bending moment, because of the limited ductility and brittle rupture of concrete, it was suggested to keep the conservative equation proposed by the Eurocode-4 for evaluating the quantity of the effective slab width to (l_o/8). In the zones of hogging bending moment, because of the high ductility of the reinforcing bars, a less conservative solution was proposed to (l_o/4), where (l_o) is the distance between the points of zero bending moment.

Chiewanichakorn, 2004, introduced an effective slab width definition through a three-dimensional non-linear finite element analysis employed to evaluate and determine the actual effective slab width of steel-composite bridge girders. The resulting effective width was larger than the ones provided by many design specifications, both nationally and internationally. The revised effective slab width criteria based on the proposed effective slab width definition was compared with other design specifications, specifically AASHTO LRFD, British, Canadian, Japanese, and Eurocode-4 design specifications.

Chun, and Cai, 2008, investigated the shear-lag phenomenon in steel-concrete composite floor model in both elastic and inelastic stages through experimental study. The model consisted of three identical longitudinal girders and two transverse girders at the ends of the longitudinal girders. Each of the three longitudinal girders was subjected to sagging moments through four-point loads. The tested beams were analyzed by finite element method through ANSYS program. It was found that the effective slab width at the ultimate strength is larger than that at the serviceability stage. The ratio of slab width to span length and loading types has significant influence on the degree of shear lag. The shear-lag effect is more obvious under one-point load than other loading types. **Salama and Nassif, 2011,** presented results from an experimental and analytical investigation to determine the effective slab width in steel-concrete composite beams. Beam test specimens had variable flange widths, steel beam sizes and various degrees of composite action. It was observed that the increase of the aspect ratio from 0.25 to 0.75 decreases the effective width ratio about 15%. Also it was observed that the stress distribution for the beams does not change as the depth of steel beams increases.

3. EFFECTIVE WIDTH IN CODE OF PRACTICE

The effective width can be thought of as the width of theoretical flange, which carries a compression force with uniform stress of magnitude equal to the peak stress at the edge of the prototype wide flange when carrying the same total compression force. The effective width concept has been widely recognized and implemented into different codes of practice around the world. The formulas used by various codes are shown in **Table 1**.

4. OBJECTIVE

The aim of this study is to investigate the behavior of the effective slab width and stress distribution (shear lag) on the composite beams with web openings subjected to static load. The composite beams are consisting of a concrete slab connected together with a steel beam by means of headed stud shear connector. The openings are made in the steel section. Three-dimensional finite element model by ANSYS 11.0 program is used for simulating the behavior of composite steel-concrete members within linear elastic range of the behavior of composite beam. The composite beams are analyzed by considering linear behavior of steel beam, concrete slab, shear connectors, and slab reinforcement.

5. VERIFICATION OF THE FINITE ELEMENT IDEALIZATION

The validity and accuracy of the finite element idealization are studied and checked by analyzing Steel-concrete composite beams that have been experimentally tested by **Hamoodi and Hadi, 2011**. Six composite beams of steel I-section and concrete slab connected together by headed shear studs welded to the top flange of the steel section are tested. Each one has an overall length of 2.1m and a clear span of 2.0m and subjected to a concentrated load at mid span. The dimensions and reinforcement details of a typical beam section are shown in **Fig.2**

In the present section, two types of composite beam are chosen, one solid beam without web opening designated as beam (CB0), and beam (CB3) with two web openings. The solid beam (CB0) is chosen to demonstrate the behavior of a typical composite beam and to represent a reference beam when web openings are introduced. The second beam (CB3) is chosen to demonstrate the behavior of composite beam when constructed with openings in the web and to verify finite element idealization with experimental one when openings are present in the web of the steel beam. The configurations of the six tested beams by **Hamoodi and Hadi, 2011** are shown in **Fig.3**.

5.1 Finite Element Modeling and Material Properties

The steel-concrete composite beams are modeled by a three-dimensional eight-node solid element (SOLID 45) is used for the concrete slab, while the steel reinforcement bar is modeled by a spar element (LINK 8). In the modeling of the steel beam; a four-node shell element (SHELL63) is used. A spar element (LINK8) is used to model shear connector to resist uplift, while the dowel action of shear connector is modeled by combine element (COMBIN14). In the modeling of the interface between two surfaces a contact element (CONTA174) and target element (TARGE170) are used. Material properties of the two beams are summarized in **Table 2**. The boundary conditions of these beams are applied to roller and hinged support as shown in **Figs.4 and 5**. The external force is (80kN) modeled as point loads distributed across the concrete slab that is located over the steel section at mid-span.

5.2 Verification of the Results

A comparison between the numerical and the experimental results has been made to verify the accuracy of the numerical models obtained using linear finite element analysis carried out on beams CB0 and CB3. **Tables 3** and **4** show the comparison between experimental and analytical deflection, while experimental and analytical load-deflection curves are shown in **Figs.6** and **7**. From the comparison presented it can be concluded that the adopted finite element idealization and the resulting numerical beam model are adequate and yield results which are accurate and in close agreement with experimental one.

6. PARAMETRIC STUDY

Several important parameters affecting the stress distribution in the concrete slab, and hence the effective slab width for the composite beams with web openings, are investigated using the presently verified FE model. One parameter has been considered to vary while the other parameters being held constant in order to separate the effect of the parameter considered. The simply supported composite beams tested by **Hamoodi and Hadi, 2011,** have been selected to carry out the parametric study. The parameters, which have been studied, can be summarized as follows:

1. Effect of openings location, size and number.
2. Effect of beam slab width to span length ratio (2b/L ratio).
3. Effect of concrete slab thickness.
4. Effect of boundary conditions at the edges of the concrete slab.
5. Effect of steel beam depth.

In this work, three types of loading are investigated:

- Concentrated Load (CL) at mid span (80 kN).
- Line Load (LL) on the longitudinal web axis (40 kN/m).
- Uniform Distributed Load (UDL) on over all slab equivalents to (80 kN).

6.1 Effect of Openings Location, Size and Number

In this section, a comparison is presented between results of beam CB0, a composite beam without web openings, and results of beams CB1 and CB2, composite beams with single central and quarter span opening, respectively, in order to investigate the effect of openings location. Results presented in **Fig.8** shows that introducing a central opening causes an increase by about 26.60% in the slab longitudinal stresses at mid-span section due to CL, while an increase by about 18.8% is observed when a single web opening is introduced at quarter-span section. On the other hand, **Fig.9** indicates that introducing a central web opening causes a maximum decrease of about 21% in the effective slab width at mid-span section, while a maximum decrease of about 18% due to the presence of a single quarter-span section is observed.

The effect of increasing the number of web openings is presented through a comparison between results of beam CB3, a beam with two openings, and results of beam CB4, a beam with three openings. Results presented in **Fig.10** shows that increasing the number of openings from two to three causes a maximum increase in the mid-span section longitudinal slab stresses of about 19% due to CL loading, whereas a maximum decrease in the effective slab width of about 6% at mid-span section is observed when comparing results in **Fig.11** due to increasing number of web openings.

The effect of size of web openings is shown in comparison between results of beam CB4, a beam with (100mm) opening depth and (200mm) width, and results of beam CB5, a beam with (80mm) opening depth and (100mm) width. Results presented in **Fig.12** shows that decreasing the web opening size causes a decrease of about 10% in the slab longitudinal stresses at mid span section due to CL loading. On the other hand, a minor effect for the web opening size on the effective slab width near mid span can be concluded when comparing results presented in **Table 6** for beams CB4 and CB5 for the three types of loadings. The summary on the effect of openings location, size and number on the effective width ratio at mid-span for the six beams and for the three types of loadings is listed in **Table 5**. Comparison of the effective slab width with design specifications is shown in **Table 6**.

6.2 Effect of Beam Slab Width to Span Length Ratio (2b/L ratio)

The effect of panel proportion on the effective slab width at mid-span for beams CB3 and CB4 for the three types of loading is listed in **Table 7**. Comparison of the effective slab width with design specifications is shown in **Table 8**. It can be seen that the maximum effect for uniformly distributed load situation occurs when the panel proportion increases from (0.25) to (0.50) the maximum slab top surface stress decreases by 33%, and 27% for beams CB3 and CB4 as shown in **Figs. 13** and **14** , respectively. The maximum effect of panel proportion on effective slab width occurs under concentrated load and line load situations for beams CB3 and CB4, respectively. When the panel proportion increases from (0.25) to (0.50) the effective slab width decreases by 11.30% and 10% for beams CB3 and CB4, respectively as shown in **Figs. 15** and **16**.

6.3 Effect of Concrete Slab Thickness

The effect of varying slab thickness on the effective slab width at mid-span for beams CB3 and CB4 for the three types of loading is listed in **Table 9**. Comparison of the effective slab width with design specifications for the three values of the slab thickness is shown in **Table 10**. From the obtained results it can be seen that the maximum effect occurs under concentrated load situation. When the slab thickness increases from (60mm) to (120mm), the maximum slab top surface stress decreases by 31%, and 40% for beams CB3 and CB4, respectively as shown in **Figs. 17** and **18**, whereas the maximum effect of varying slab thickness on the effective slab width occurs under line load and concentrated load situations for beams CB3 and CB4, respectively. When the slab thickness increases from (60mm) to (120mm), the effective slab width decreases by 10.40% and increases by 4.50% for beams CB3 and CB4, respectively as shown in **Figs.19** and **20**.

6.4 Effect of Boundary Conditions at the Edges of the Concrete Slab

The aim of this section is to investigate the effect of concrete slab continuity along longitudinal and transverse edges as in actual floor and roof systems on the effective slab width and stress distribution in the slab due to different types of loading and panel proportions. The proposed modeling for slab continuity in the finite element model is simulated by artificial boundary conditions applied along slab edges by providing vertical rollers along these edges and across concrete slab depth as shown in **Fig. 21**.

The results of the effect of slab boundary condition with three values of panel proportions on the effective slab width at mid-span for beams CB3 and CB4 due to three types of loading are listed in **Table 11**. Comparison of the effective slab width with design specification is shown in **Table 12**. From the obtained results, it can be seen that the maximum effect for uniformly distributed load situation occurs when the panel proportions increase from (0.25) to (0.50), the maximum slab top surface stress decreases by 30%, and 25% for beams CB3 and CB4, respectively as shown in **Figs. 22 and 23**. The maximum effect of panel proportion on the effective slab width under concentrated load situation occurs when the panel proportions increase from (0.25) to (0.50), the effective slab width decreases by 11% and 21% for beams CB3 and CB4, respectively as shown in **Figs. 24 and 25**. The results also show a comparison between continuous and discontinuous slabs. Applying the boundary condition to the edge of slab makes an increase in slab top surface stress about 3% and 4% for beams CB3 and CB4, respectively under the uniformly distributed load situation for panel proportion (0.50) and has a minor effect on concentrated load and line load situations. The maximum effect on effective slab width occurs under line load and uniform distributed load for beams CB3 and CB4, respectively. Applying the boundary condition increases the effective slab width by about 7% for beam CB3 with panel proportion of (0.25) and by 2% for beam CB4 with panel proportion (0.50).

6.5 Effect of Steel Beam Depth

The effect of varying steel beam depth on the effective slab width at mid-span for beams CB3 and CB4 for the three types of loading is listed in **Table 13**. Comparison of the effective slab width with design specifications is shown in **Table 14**. From the obtained results, it can be seen that the maximum effect under the uniformly distributed load situation occurs when the steel beam depth increases from (160mm) to (240mm), the maximum slab top surface stress decreases by 42% for both beams CB3 and CB4 as shown in **Figs. 26** and **27**. The maximum effect of varying steel beam depth on the effective slab width under concentrated load situation for both beams CB3 and CB4 occurs when the steel beam depth increases from (160mm) to (240mm), the effective slab width decreases by 13% and 11% for beams CB3 and CB4, respectively as shown in **Figs. 28** and **29**.

7. PROPOSED EFFECTIVE SLAB WIDTH EQUATIONS

The current parametric study provides a database for the effective slab width for composite steel-concrete beams with web openings. This database can be used to develop expressions for the effective slab width. The results presented previously show that web openings location and type of loading on the beam are the most critical factors affecting effective slab width values. Uniformly distributed load and line load generally yields close values for the effective slab width. Therefore, it is suggested to treat both loading type in a uniform manner such that single equation based on uniform load data is adopted. Accordingly, it is intended to provide two sets of equations, one for the case when central span web opening exists and the other for the case of quarter span opening. Moreover, each set consists of two equations, one for effective slab width due to concentrated load effect and the other due to uniform distributed load effect.

Proposed equations include the three major parameters that affect effective slab width ($2\bar{b}$), which are panel width to span length ratio (2b/L ratio), slab thickness (t_{slab}) and steel beam depth (h_{steel}) as shown below:

- **Quarter-span openings**

1. Concentrated Load *:*

$$2\bar{b} = 177.4 + 978.2\ (2b/L) - 0.15\ (t_{slab}) - 0.63\ (h_{steel}) \qquad (2)$$

2. Uniformly Distributed and Line Loads:

$$2\bar{b} = -13.9 + 1864.4(2b/L) - 0.24(t_{slab}) - 0.023(h_{steel}) \qquad (3)$$

- **Mid-span openings**

3. Concentrated Load*:*

$$2\bar{b} = 106.2 + 964.9(2b/L) + 0.22\ (t_{slab}) - 0.44(h_{steel}) \qquad (4)$$

4. Uniformly Distributed and Line Loads *:*

$$2\bar{b} = 40.8 + 1643.3(2b/L) + 0.29\ (t_{slab}) - 0.11(h_{steel}) \qquad (5)$$

In these equations, L is span length (mm), b half slab width (mm), t_{slab} is concrete slab thickness (mm) and h_{steel} is steel beam depth (mm).

Finally, it is proposed to present another set of equations that correlate effective slab width with the most critical factor obtained from the parametric study, i.e., panel aspect ratio (2b/L). These equations take into account implicitly the effect of web opening presence while ignoring concrete slab thickness and steel beam depth. This set of equations is intended to be more simplified than the previously presented equations and more convenient to be used by design authorities and building codes.

Considering that; (S=2b) as in the design codes and panel aspect ratio β= (2b/L), then the effective slab width equations:

1. Due to Concentrated Load:

$$2\bar{b} = (0.7 - 0.3\beta) \times S \qquad (6)$$

2. Due to Uniformly Distributed and Line Loads:

$$2\bar{b} = (1.0 - 0.3\beta) \times S \qquad (7)$$

These equations take into account the effect of span length (L) and spacing of the beams (S) as stipulated by various codes presented in **Table 1**.

8. VERIFYING PROPOSED EQUATION RESULTS

To verify the validity of the proposed equations, comparison was made between the results obtained from the developed equations and the results from the current finite element analysis. **Figs.30-35** show plots of the comparison of the effective slab width ($2\bar{b}$) obtained from the finite element analysis and those obtained from Eqs. (2), (3), (4), and (5) for the three types of loading. **Figs.36** and **47** show plots of the comparison of the effective slab width ($2\bar{b}$) obtained from the finite element analysis and those obtained from the simplified Eqs. (6) and (7). It can be observed that the proposed equations have good agreement with the finite element results which indicates that the proposed equations have good correlation with numerical result.

9. CONCLUSIONS

An extensive study is carried out on the behavior of composite steel-concrete beams in which the upper flange of the steel beam is attached to reinforced concrete slab. Stress distribution and effective slab width for the composite beams are investigated with special emphasis on composite beams with openings in the steel web. The finite element analysis has been used to investigate shear lag phenomenon and the resulting effective slab width adopted in the classical T-beam approach. Comparison is made with available limitation and regulations stipulated by different codes of practice. According to the case studies and comparison presented in this study, the following conclusions are drawn:

1. The results presented show that the effective slab width strongly depends on the type of loading with the minimum values obtained due to concentrated load, while uniformly distributed load and line load generally yield similar values approaching full slab width.
2. For the different types of loading considered, effective slab width depends on the position along the span of the beam. Effective slab width is reduced to minimum values near mid span, support and opening locations, while it tends to reach full slab width elsewhere.
3. Introducing central span web opening causes a maximum decrease in the effective slab width of about 21%, whereas a maximum decrease of about 18% is observed due to presence of quarter span web opening.
4. Increasing the number of web openings has a minor effect on the effective slab width with a maximum decrease of 6% at mid span section observed when the number of openings is increased from two to three.
5. Varying standard web opening size has negligible effect on the effective slab width.
6. Increasing steel beam depth to twice values causes a decrease in the effective slab width of about 11% to 13% for different web opening configurations. Almost the same effect is observed when concrete slab thickness is increased twice.
7. Results indicate that the standard codes of practice, and hence the T-beam theory, generally overestimate the effective slab width due to concentrated loads especially for small values of panel proportions, i.e., 2b/L=0.25. On the other hand, close agreement is observed for higher panel aspect ratios.
8. Uniformly distributed load and line load results reveal that the standard codes of practice and the T-beam theory underestimate the effective slab width especially for high values of panel proportion, i.e., 2b/L=0.50. On the other hand, close agreement is observed for smaller panel aspect ratios.
9. Sets of empirical expressions to estimate effective slab width are developed. These equations can be used to estimate effective slab width for different types of loading, web opening locations, panel proportion, concrete slab thickness and steel beam depth.

REFRERENCES

- ANSYS 11.0 Inc., 2002, *ANSYS Manual*, Version 11.0, U.S.A.

- American Concrete Institute, 2008, *Building Code Requirements for Structural Concrete*, ACI-318M-08, Detroit, Michigan, USA.

- AASHTO-LRFD, 2004, *Bridge Design Specification*, American Association of State Highway and Transportation Officials (AASHTO), Third Edition, Washington D.C.

- AISE, 1986, *Load Resistance Factor Design (LRFD)*, Manual of Steel Construction, First Edition, American Institute of Steel Construction, pp.1124.

- BSI, 1997, *Structure Use of Concrete, Part 1: Code of Practice for Design and Construction*, BSI8110, British Standard Institution, London.

- Chiewanichakorn**,** M., and Chen, S. S., 2004, *Effective Flange Width Definition for Steel-Concrete Composite Bridge Girder*, Journal of Structure Engineering, ASCE, Vol.130, No. 12, pp.2016-2031.

- Chun-Yu Tian, and Cai, C. S., 2008, *Effective Width of Steel-Concrete Composite Beam at Ultimate Strength State*, Journal of Engineering Structure, Vol.30, pp.1396-1407.

- Fragiacomo**,** M. and Amadio, C., 2003, *Experimental Evaluation of Effective Width in Steel-Concrete Composite Beams*, Journal of Construction Steel Research, Vol.60, pp.199-220.

- Heins, C. P. and Fan, H. M., 1976, *Effective Composite Beam Width at Ultimate Load*, Journal of the Structure Division, Proceedings of the ASCE, Vol.102, pp. 2163-2179.

- Hamoodi, M. J., and Hadi, W. K., 2011, *Tests of Composite Beams with Web Openings*, Engineering and Technology Journal, Vol.29, No.10, pp.2073-2086, Iraq.

- Salama, T. and Nassif, H., 2011, *Effective Flange Width for Composite Steel Beams*, Journal of Engineering Research, Vol.8, No.1, pp.28-43.

Table 1. Effective slab width formulas in various codes.

Code	Formula
AASHTO	**$2\bar{b}$ is least of:** **1. L/4** **2. s** **3. 12hc**
ACI	**$2\bar{b}$ (interior girder) is least of:** **1. L/4** **2. s** **3.bw + 16hc** **$2\bar{b}$ (exterior girder) is least of:** **1. L/12+bw** **2. 6hc+bw** **3. s/2+bw**
AISC	**$2\bar{b}$ is the least of:** **1. L/4** **2. s** **3. 2be**
BSI 8110	**$2\bar{b}$ is least of:** **1. L/5+bw** **2. s**

Where:
(**L**) span length, (**s**) spacing of beams, (**h_c**) concrete slab thickness, (**b_w**) width of web for reinforced concrete T-beams, (**b_e**) distance from beam center to the free edge of the slab.

Table 2. Material properties used for composite steel-concrete beam verification study, **Hamoodi and Hadi, 2011**.

	Symbol	Definition	Value
Concrete	f'_c	Compressive Strength (MPa)	23.20
	E_c	Young's Modulus (MPa)	22540
	f_{ct}	Tensile Strength (MPa)	1.59
	v	Poisson's Ratio	0.15
Reinforcement	f_Y	Yield Stress (MPa)	650
	E_s	Young's Modulus (MPa)	198000
	υ	Poisson's Ratio	0.30
Steel Beam	f_Y	Yield Stress (MPa)	337
	E_s	Young's Modulus (MPa)	196000
	υ	Poisson's Ratio	0.30
Shear Connector	H	Overall Height (mm)	45
	φ	Diameter (mm)	8
	S_{stud}	Spacing (mm)	150
	N_f	Number of Studs per row	15
	E_s	Young's Modulus (MPa)	200000

Table 3. Comparison between experimental and numerical results of beam CB0.

Beam	Load (kN)	Deflection (mm)		Absolute Error %
		Experimental	Analytical	
(CB0)	20	1.2511	1.2467	0.35
	40	2.5321	2.4912	1.6
	60	3.7678	3.8755	2.85
	80	4.9592	4.9838	0.14

Table 4. Comparison between experimental and numerical results of beam CB3.

Beam	Load (kN)	Deflection (mm)		Absolute Error %
		Experimental	Analytical	
(CB3)	20	1.391	1.438	3.38
	40	2.792	2.876	3.10
	60	4.131	4.313	2.85
	80	5.731	5.751	0.348

Table 5. Effective slab width ratio.

Beam Type	Effective Slab Width Ratio $\bar{b}/b$		
	Mid-span		
	CL	LL	UDL
CB0	0.725	0.889	0.951
CB1	0.578	0.858	0.861
CB2	0.593	0.891	0.948
CB3	0.611	0.909	0.930
CB4	0.576	0.855	0.904
CB5	0.580	0.853	0.905

Table 6. Comparison of effective slab width at mid-span with design specifications.

Beam Type	$2\bar{b}$ (mm)			AASHTTO	ACI	AISC
	CL	LL	UDL			
CB0	362.286	444.693	475.621	500	500	500
CB1	289.02	429.217	430.545	500	500	500
CB2	296.594	445.473	438.287	500	500	500
CB3	305.426	454.327	465.031	500	500	500
CB4	288.232	427.251	452.225	500	500	500
CB5	289.906	426.560	452.302	500	500	500

Table 7. Effect of panel proportioning on the effective slab width.

Beam Type	Panel (*) Proportion	Effective Slab Width Ratio $\bar{b}/b$		
		Mid-span		
		CL	LL	UDL
CB3	0.25	0.611	0.909	0.930
	0.40	0.602	0.908	0.914
	0.50	0.543	0.885	0.908
CB4	0.25	0.577	0.855	0.905
	0.40	0.548	0.797	0.873
	0.50	0.529	0.770	0.867

(*) Panel proportion = 2b/L, L = 2000mm

Table 8. Comparison of effective slab width at mid-span with design specifications.

Beam Type	Panel [(*)] Proportion	$2\bar{b}$ (mm)			AASHTTO	ACI	AISC
		CL	LL	UDL			
CB3	0.25	305.426	454.327	465.130	500	500	500
	0.40	481.214	727.100	731.223	500	500	500
	0.50	542.874	885.393	935.342	500	500	500
CB4	0.25	288.232	427.251	452.225	500	500	500
	0.40	438.156	637.716	698.748	500	500	500
	0.50	528.760	769.982	867.167	500	500	500

(*) Panel proportion = 2b/L, L = 2000mm

Table 9. Effect of varying slab thickness on the effective slab width ratio.

Beam Type	Slab Thickness(mm)	Effective Slab Width Ratio $\bar{b}/b$		
		Mid-span		
		CL	LL	UDL
CB3	60	0.611	0.909	0.930
	90	0.613	0.847	0.945
	120	0.606	0.815	0.930
CB4	60	0.577	0.855	0.905
	90	0.600	0.879	0.927
	120	0.602	0.890	0.939

Table 10. Comparison of effective slab width with design specifications for different values of slab thickness.

Beam Type	Slab Thickness(mm)	$2\bar{b}$ (mm)			AASHTTO	ACI	AISC
		CL	LL	UDL			
CB3	60	305.426	454.327	465.130	500	500	500
	90	306.566	454.446	472.731	500	500	500
	120	303.112	407.583	475.376	500	500	500
CB4	60	288.232	427.251	452.225	500	500	500
	90	299.916	439.604	463.705	500	500	500
	120	301.200	444.992	469.596	500	500	500

Table 11. Effect of slab boundary conditions on the effective width ratio.

Beam Type	Panel Proportion	Effective Slab Width Ratio Ratio $\bar{b}/b$					
		Mid-span					
		Continues Slab			Discontinues Slab		
		CL	LL	UDL	CL	LL	UDL
CB3	0.25	0.613	0.910	0.931	0.611	0.847	0.930
	0.40	0.588	0.912	0.910	0.602	0.908	0.914
	0.50	0.548	0.896	0.925	0.543	0.885	0.935
CB4	0.25	0.578	0.855	0.909	0.577	0.855	0.905
	0.40	0.535	0.799	0.878	0.548	0.797	0.873
	0.50	0.518	0.777	0.880	0.529	0.770	0.867

Table 12. Comparison of effective slab width at mid-span with design specifications.

Beam Type	Panel Proportion	$2\bar{b}$ (mm)			AASHTTO	ACI	AISC
		CL	LL	UDL			
CB3	0.25	306.451	454.844	464.928	500	500	500
	0.40	470.290	729.235	728.036	500	500	500
	0.50	547.811	895.587	924.898	500	500	500
CB4	0.25	289.185	427.286	454.356	500	500	500
	0.40	407.615	638.822	702.552	500	500	500
	0.50	457.871	776.699	880.362	500	500	500

Table 13. Effect of steel beam depth on the effective slab width.

Beam Type	Steel Beam Depth (mm)	Effective Slab Width Ratio Ratio $\bar{b}/b$		
		Mid-span		
		CL	LL	UDL
CB3	160	0.611	0.909	0.930
	200	0.564	0.893	0.926
	240	0.527	0.879	0.920
CB4	160	0.577	0.855	0.905
	200	0.537	0.833	0.898
	240	0.512	0.820	0.903

Table 14. Comparison of effective slab width with design specifications for different values of steel beam depth.

Beam Type	Steel Beam Depth mm)	$2\bar{b}$ (mm)			AASHTTO	ACI	AISC
		CL	LL	UDL			
CB3	160	305.426	454.327	465.130	500	500	500
	200	282.219	446.745	463.013	500	500	500
	240	263.635	439.604	460.266	500	500	500
CB4	160	288.232	427.251	452.225	500	500	500
	200	268.517	416.249	448.992	500	500	500
	240	256	410.143	451.514	500	500	500

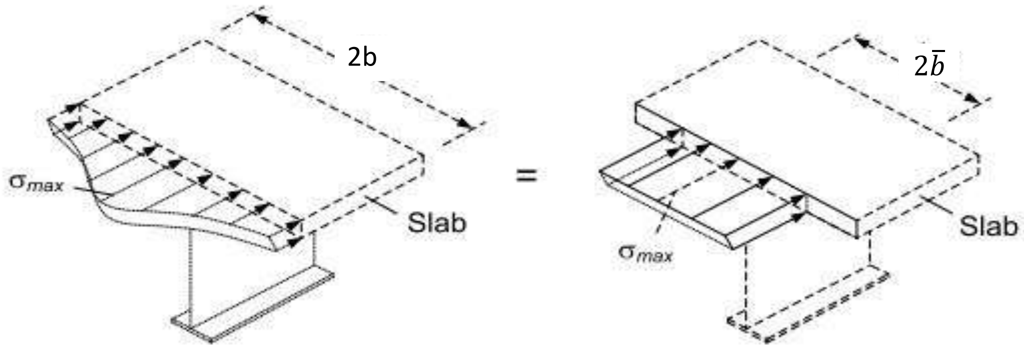

Figure 1. Shear lag effect.

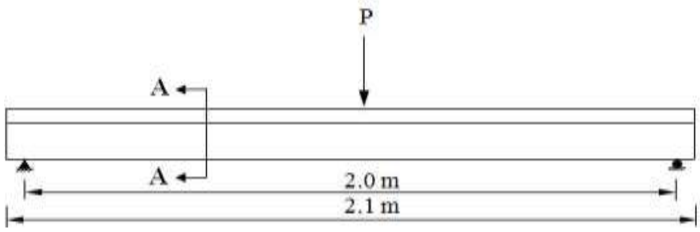

(a) Typical dimensions of a composite beam.

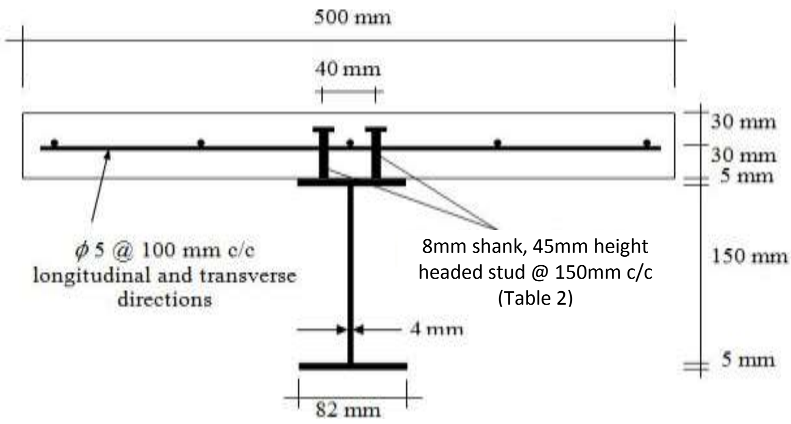

(b) Section A-A.

Figure 2. Typical cross section of the composite beam, **Hamoodi and Hadi, 2011**.

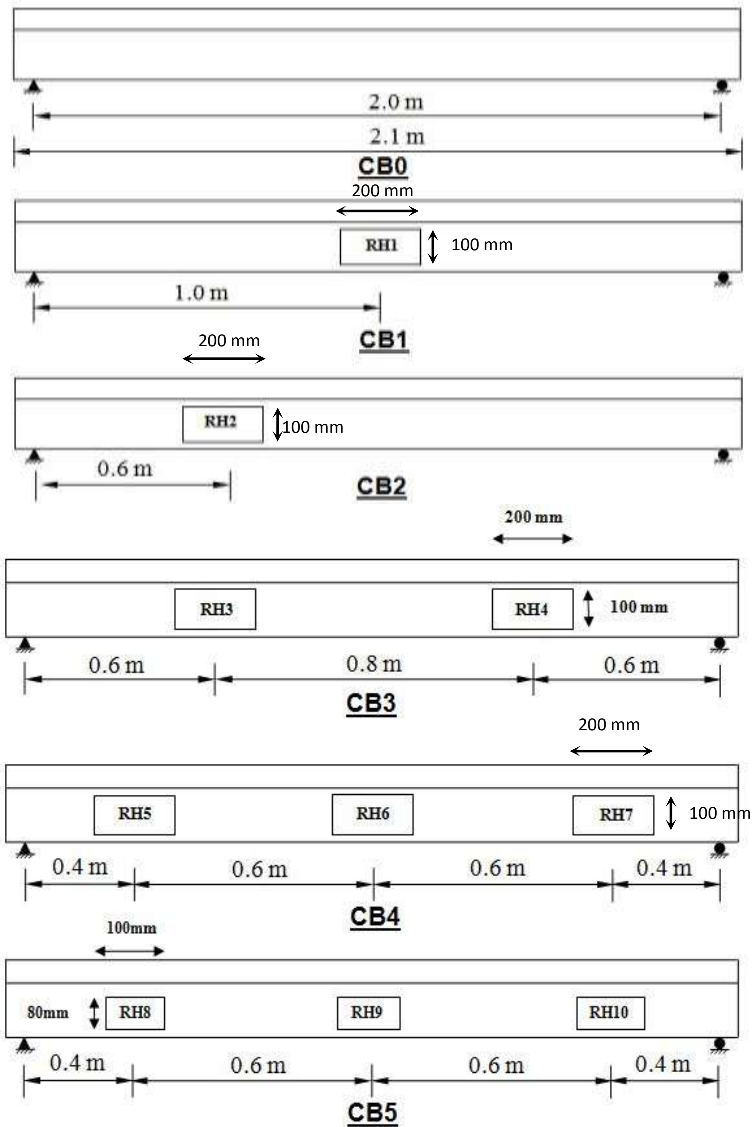

Figure 3. Configurations and locations of web openings, **Hamoodi and Hadi, 2011**.

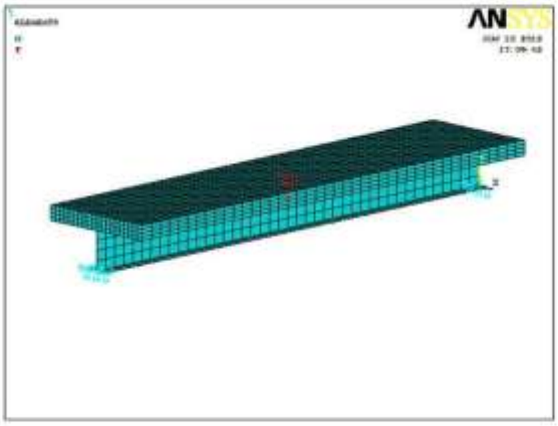

Figure 4. Three-Dimensional finite element mesh for the composite beam CB0.

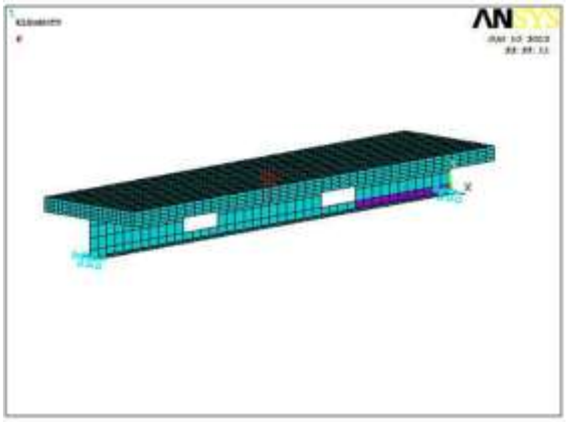

Figure 5. Three-dimensional finite element mesh for composite beam CB3.

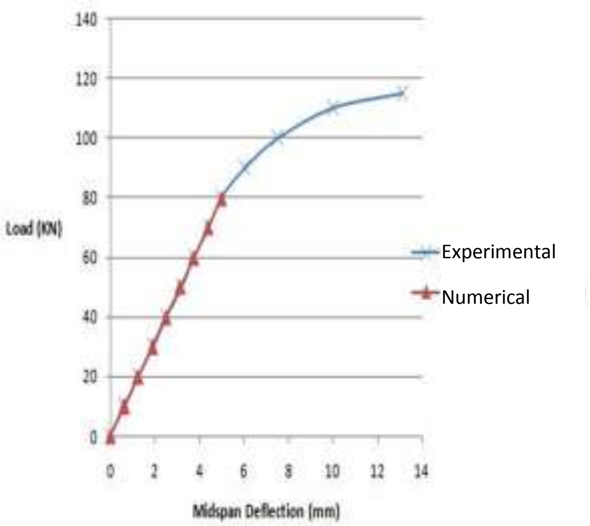

Figure 6. Experimental and numerical load- deflection curve for beam CB0.

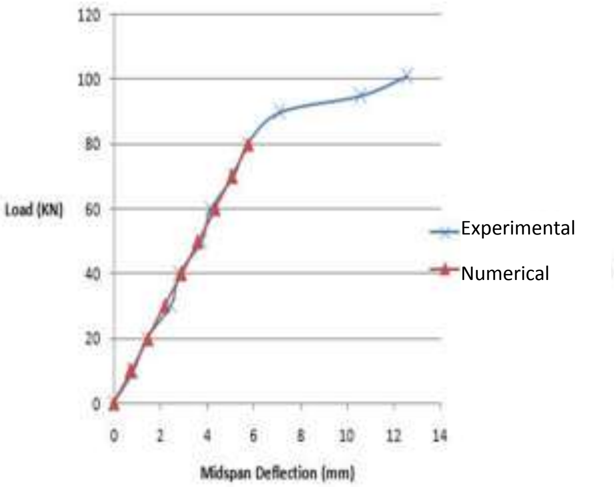

Figure 7. Experimental and numerical load-deflection curve for beam CB3.

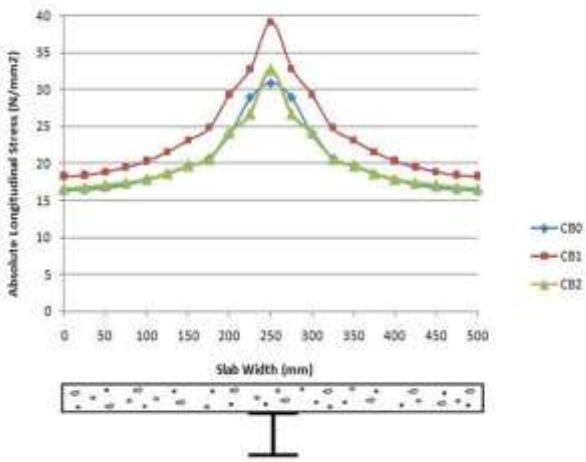

Figure 8. Slab stress distributions of beams CB0, CB1 and CB2 due to (CL) loading.

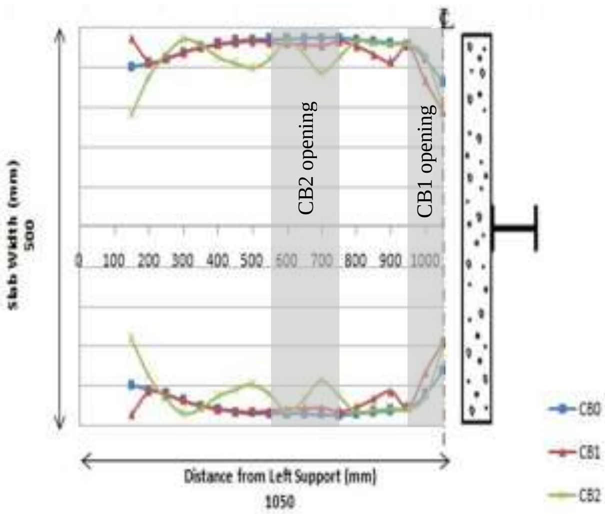

Figure 9. Effective slab width of beams CB0, CB1, and CB2 due to (CL) loading.

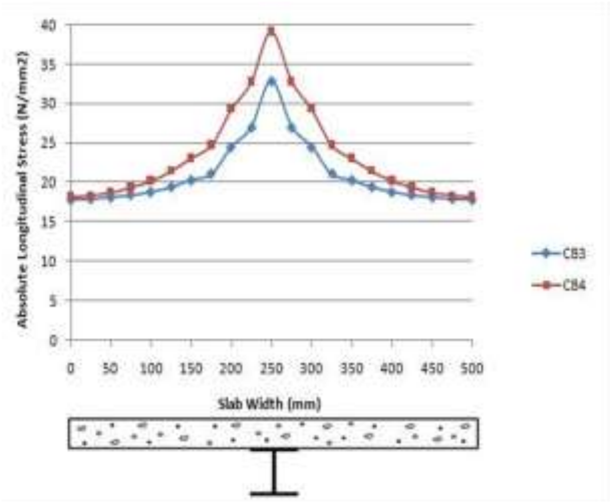

Figure 10. Slab stress distribution at mid-span of CB3 and CB4 beams due to (CL) loading.

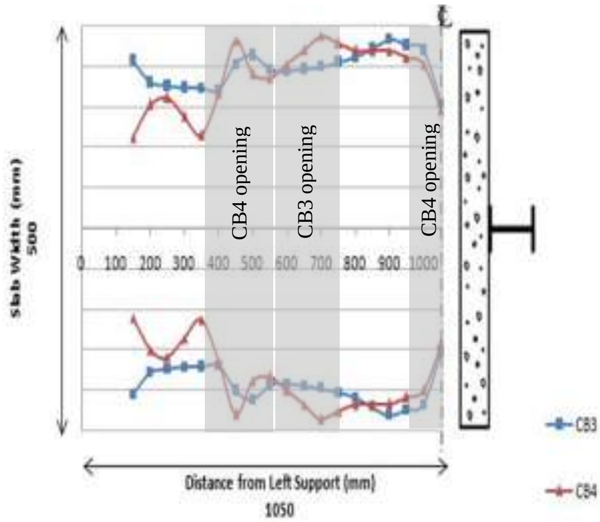

Figure 11. Effective slab width of beams CB3 and CB4 due to (CL) loading.

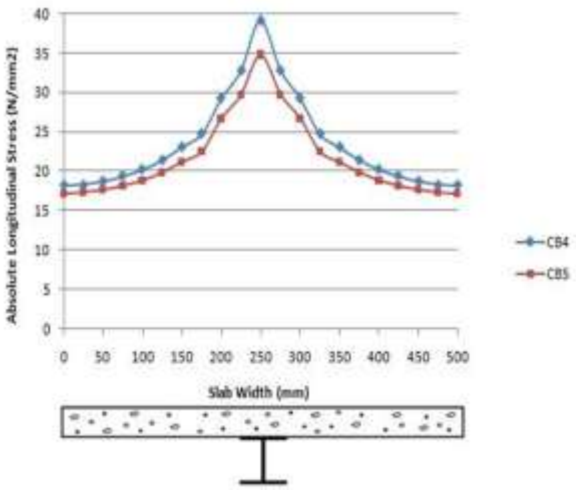

Figure 12. Slab stress distribution at mid-Span of CB4 and CB5 Beams Due to (CL) Loading.

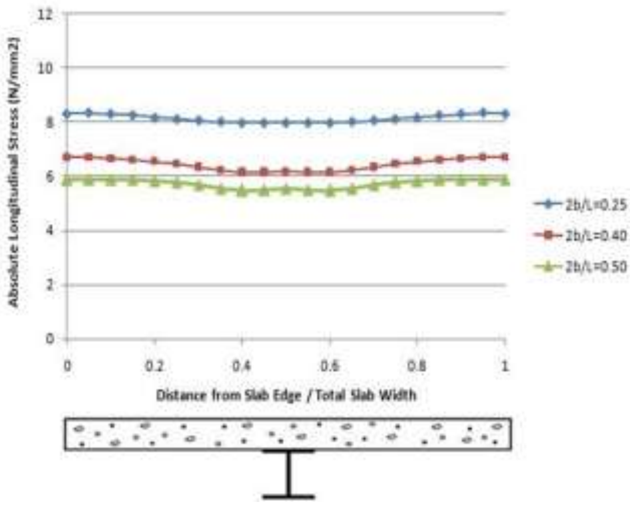

Figure 13. Slab stress distribution of CB3 for various panel proportions due to (UDL) loading.

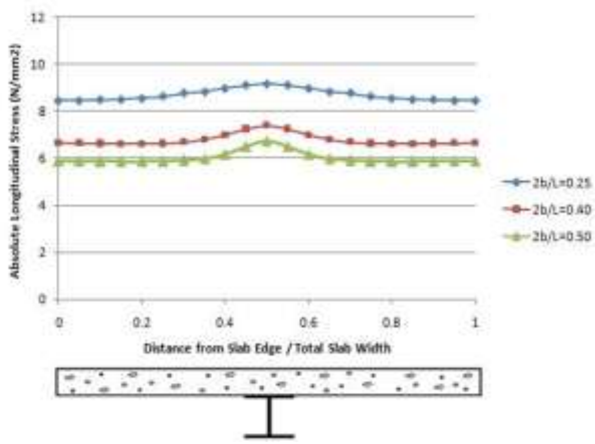

Figure 14. Slab stress distribution of CB4 for various panel proportions due to (UDL) loading.

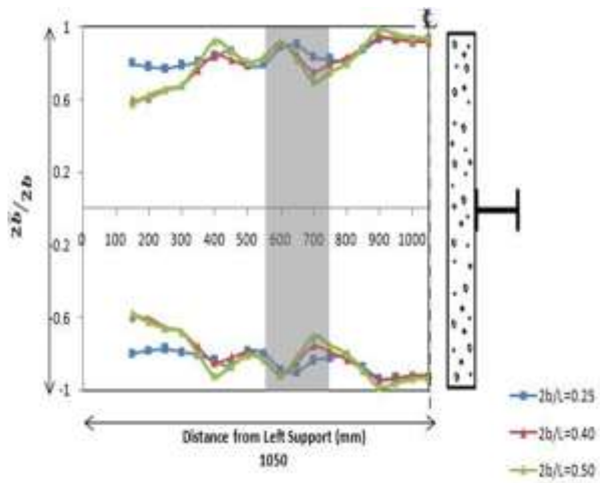

Figure 15. Effective slab width for CB3 for various panel proportions due to (UDL) loading.

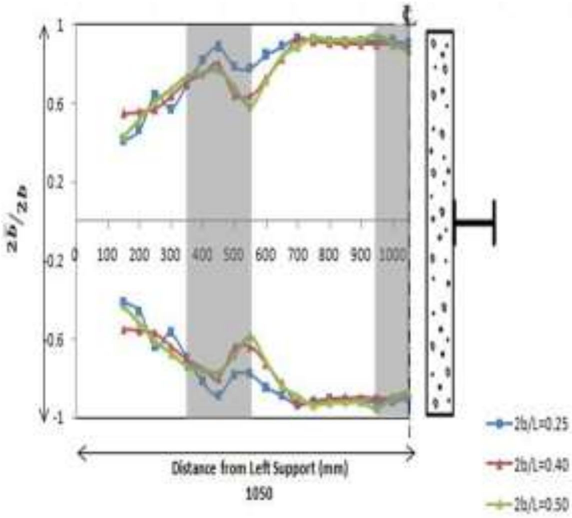

Figure 16. Effective slab width for CB4 for various panel proportions due to (UDL) loading.

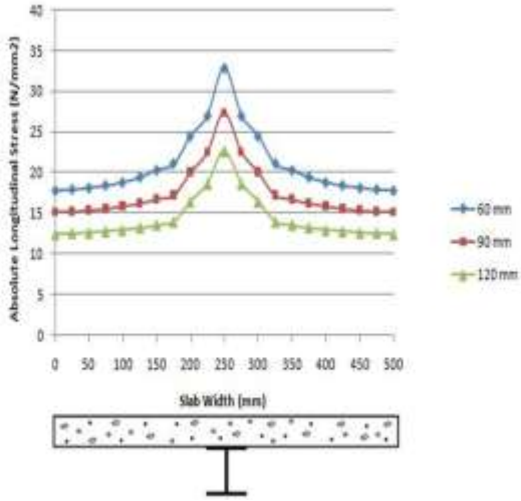

Figure 17. Slab stress distribution of CB3 for various slab thicknesses due to (CL) loading.

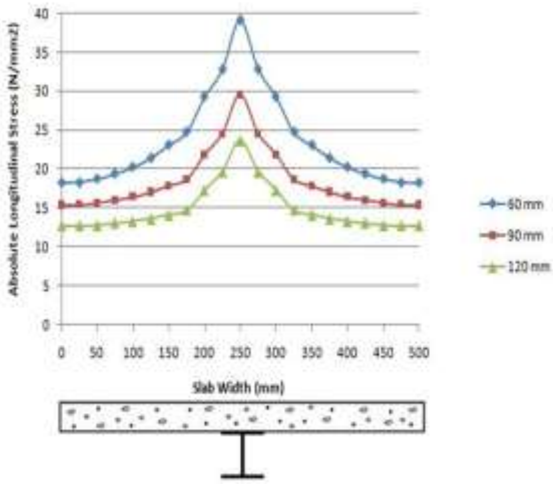

Figure 18. Slab stress distribution of CB4 for various slab thicknesses due to (CL) loading.

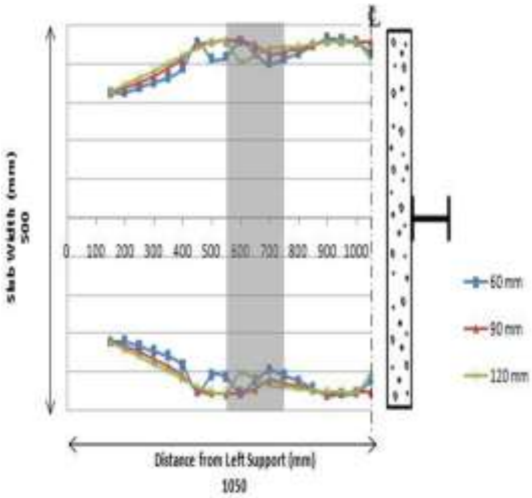

Figure 19. Effective slab width for CB3 for various slab thicknesses due to (LL) loading.

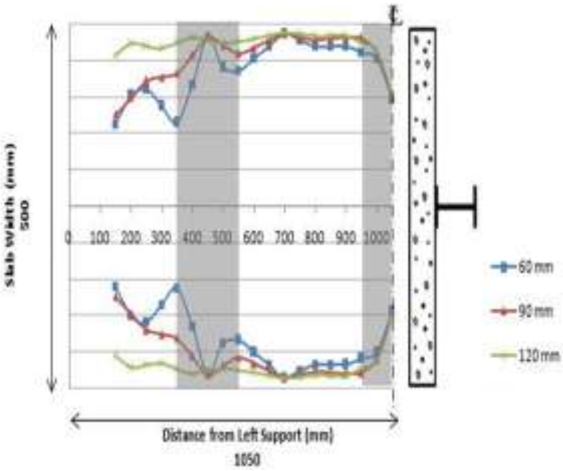

Figure 20. Effective slab width for CB4 for various slab thicknesses due to (CL) loading.

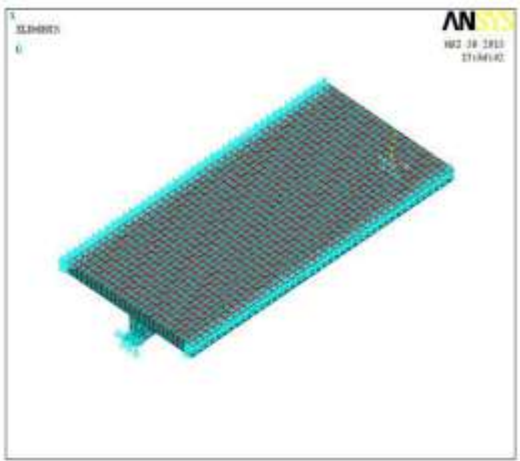

Figure 21. Boundary conditions modeling adopted to simulate concrete slab continuity.

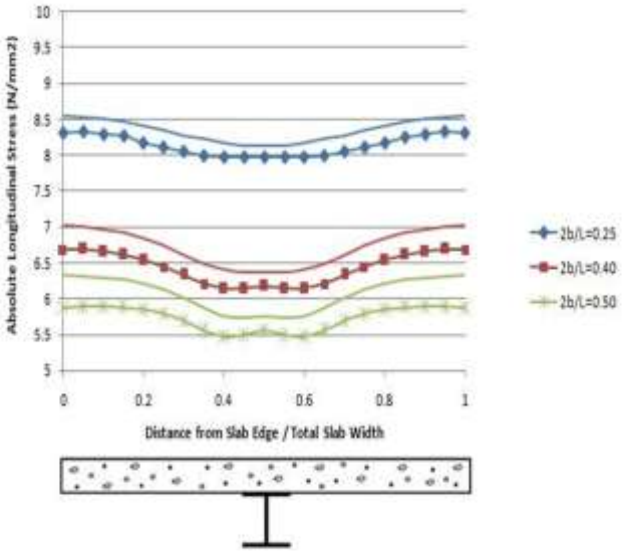

Figure 22. Slab stress distribution for CB3 for discontinuous slab (marked line) and continuous slab (unmarked line) due to (UDL) loading.

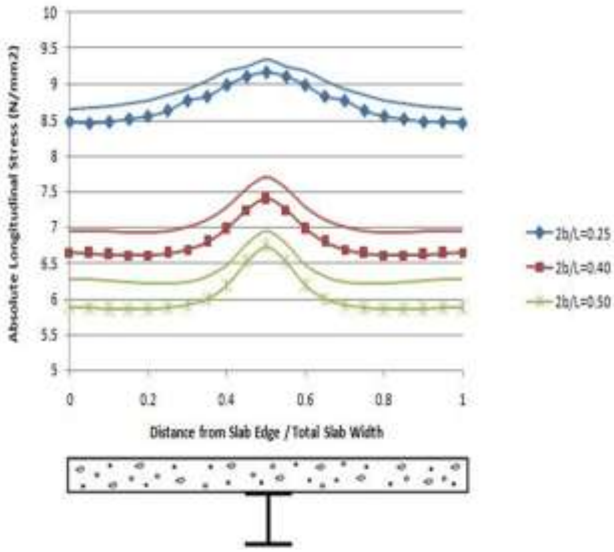

Figure 23. Slab stress distribution for CB4 for discontinuous slab (marked line) and continuous slab (unmarked line) due to (UDL) loading.

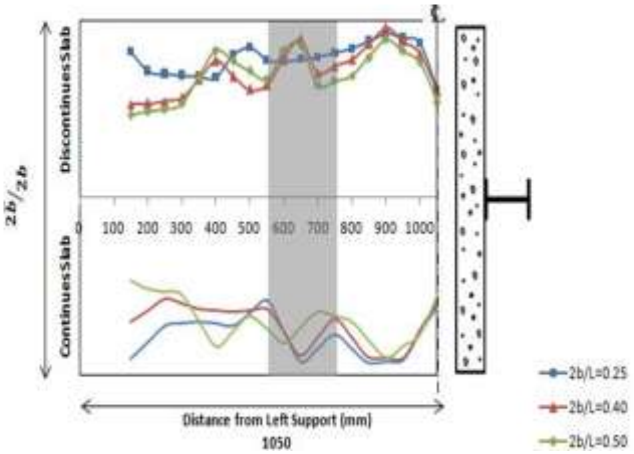

Figure 24. Slab stress distribution for CB3 for discontinuous slab (marked line) and continuous slab (unmarked line) due to (CL) Loading.

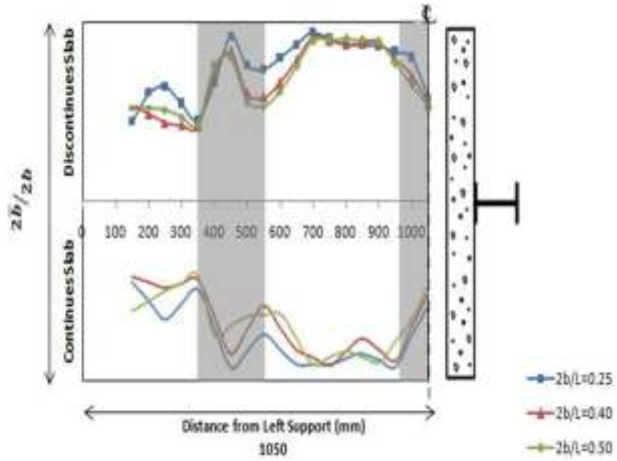

Figure 25. Slab stress distribution for CB4 for discontinuous slab (marked line) and continuous slab (unmarked line) due to (CL) Loading.

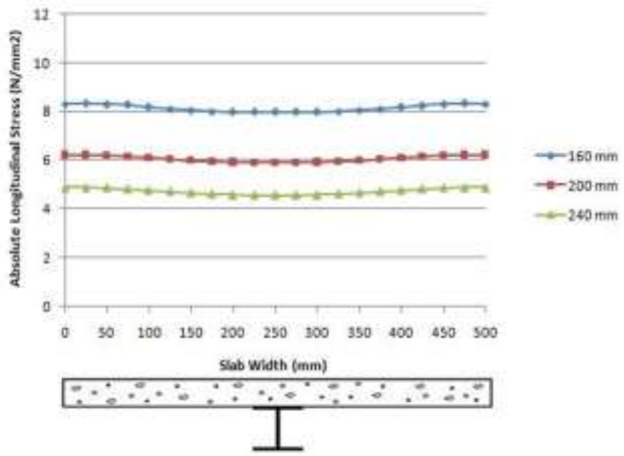

Figure 26. Slab stress distribution of beam CB3 for various steel beam depths due to (UDL) loading.

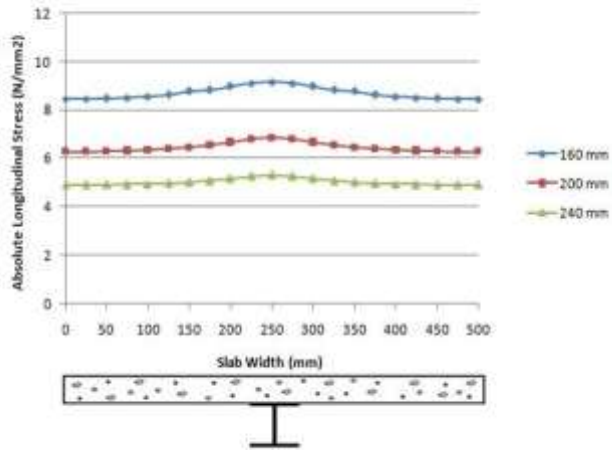

Figure 27. Slab stress distribution of beam CB4 for various steel beam depths due to (UDL) loading.

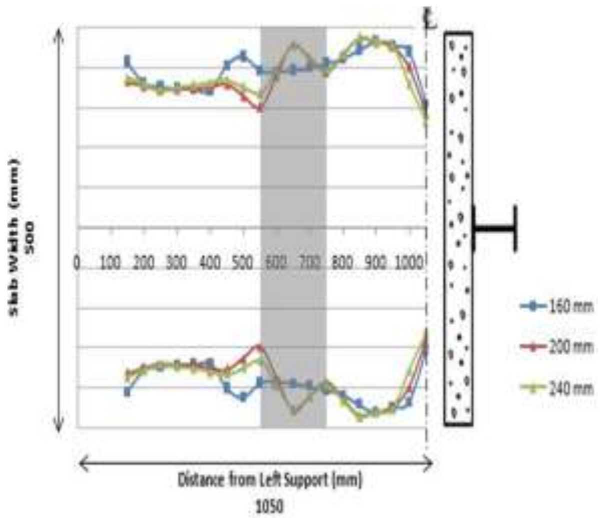

Figure 28. Effective slab width for CB3 for various steel beam depths due to (CL) loading.

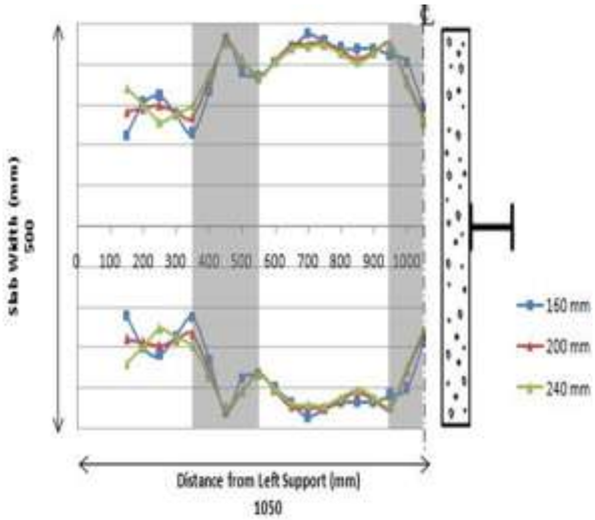

Figure 29. Effective slab width for CB4 for various steel beam depths due to (CL) loading.

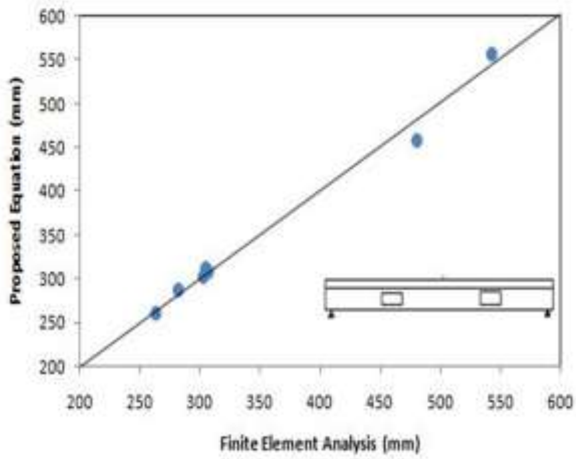

Figure 30. Effective slab width obtained from FEA and proposed equation (2) for beam CB3 due to concentrated load.

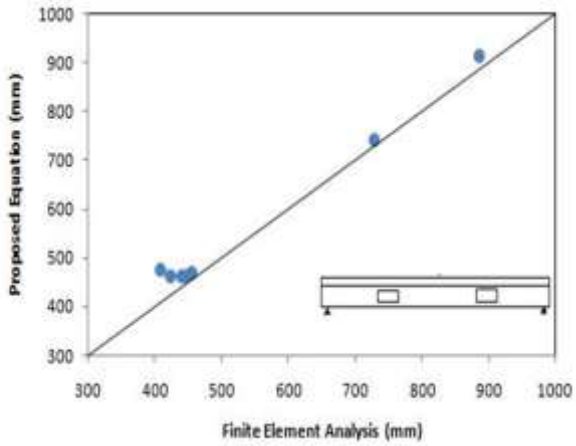

Figure 31. Effective slab width obtained from FEA and proposed equation (3) for beam CB3 due to concentrated load.

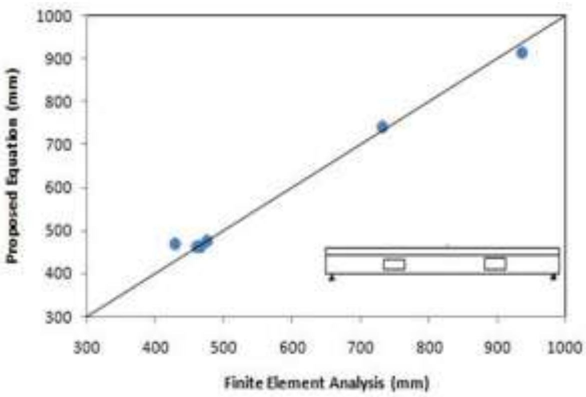

Figure 32. Effective slab width obtained from FEA and proposed equation (3) for beam CB3 due to uniformly distributed load.

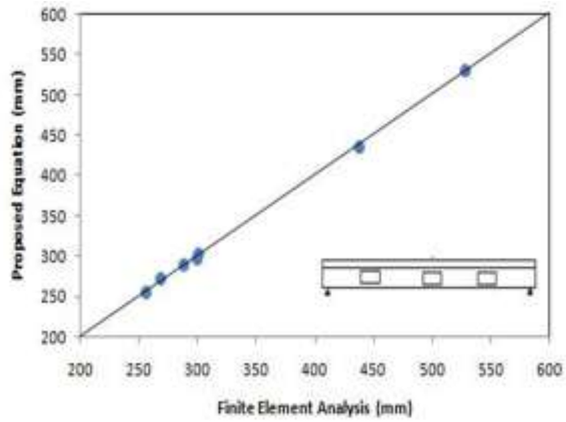

Figure 33. Effective slab width obtained from FEA and proposed equation (4) for beam CB4 due to uniformly distributed load.

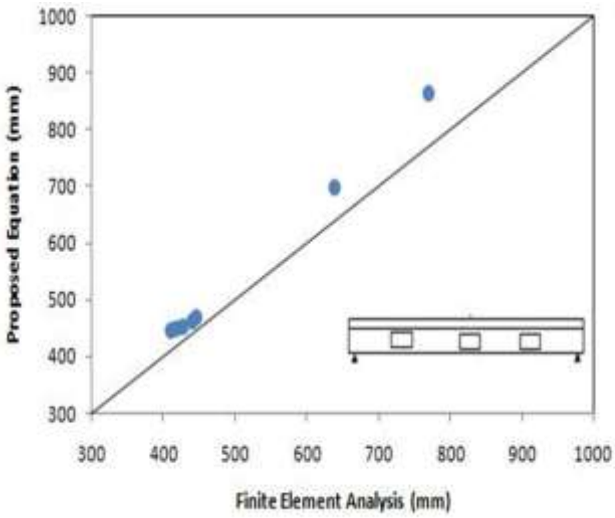

Figure 34. Effective slab width obtained from FEA and proposed equation (5) for beam CB4 due to line load.

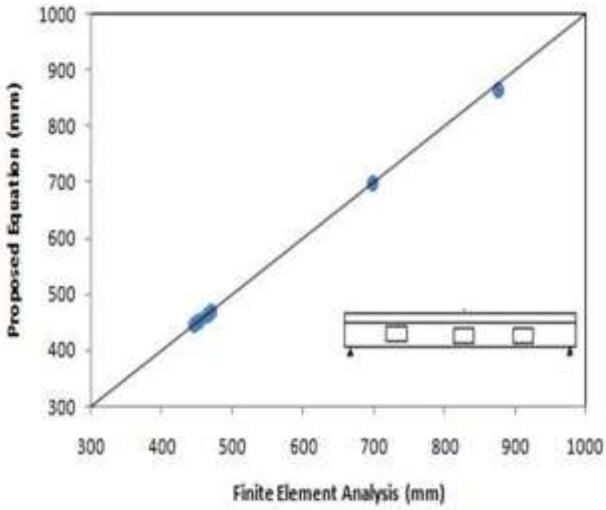

Figure 35. Effective slab width obtained from FEA and proposed equation (5) for beam CB4 due to uniformly distributed load.

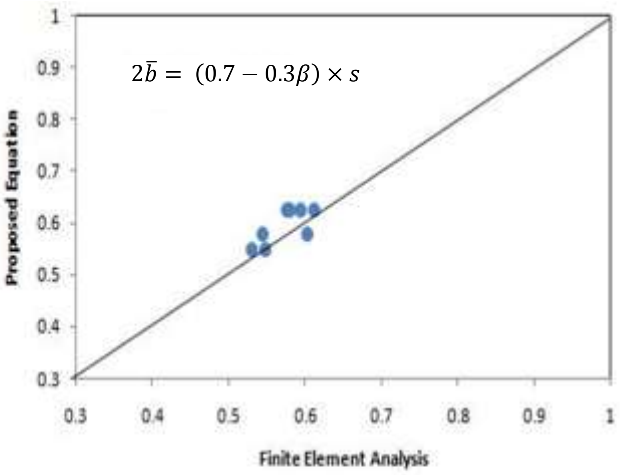

Figure 36. Effective slab width obtained from FEA and simplified equation (6) for beam CB4 due to concentrated load.

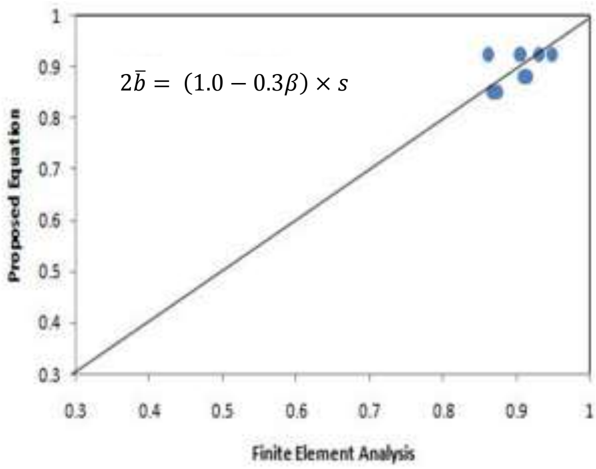

Figure 37. Effective slab width obtained from FEA and simplified equation (7) for beam CB4 due to uniformly distributed load.

Retrofitting of Reinforced Concrete Damaged Short Column Exposed to High Temperature

Asst. Prof. Dr. Amer Farouk Izzat
Department of Civil Engineering
College of Engineering
University of Baghdad
amerfarouk@yahoo.com

ABSTRACT

Experimental research was carried out to investigate the performance of CFRP wrapping jackets used for retrofitting twelve square reinforced concrete (CR) column specimens damaged by exposure to fire flame, at different temperatures of 300, 500 and 700ºC, except for two specimens that were not burned. The specimens were then loaded axially till failure after gradual or sudden cooling. The specimens were divided into two groups containing two main reinforcement ratios, $\rho= 0.0314$ and $\rho= 0.0542$. This was followed by the retrofitting procedure that included wrapping all the specimens with two layers of CFRP fabric sheets. The test results of the retrofitted specimens showed that the fire damaged RC column specimens can be retrofitted efficiently by using CFRP wrap jackets, as they provided good confinement of the damaged concrete core. Also, the ultimate load capacity of each retrofitted specimen was increased compared to that before retrofitting by about 16, 34 and 44% for the specimens burned at 300, 500 and 700ºC respectively, and cooled gradually, whereas this increase was 44% and 111% for the specimens subjected to burning temperatures of 500 and 700ºC, respectively, but cooled suddenly. This ability of each column specimen to absorb energy before and after retrofitting was also improved. The average improvement in modulus of toughness before and after retrofitting was 8% for the specimens not exposed to fire flame and 10, 100, 250% for the specimens exposed to 300, 500 and 700ºC respectively.

Key words: retrofitting, reinforced concrete column, CFRP, high temperature

اعادة تاهيل الاعمدة القصيرة الخرسانية المسلحة المتضررة المعرضة الى درجات حرارية عالية

أ.م .د. عامر فاروق عزت
قسم الهندسة المدنية
كلية الهندسة / جامعة بغداد

الخلاصة

بحث عملي اجري لغرض فحص قابلية استخدام لف سترة من CFRP لتطويق اعمدة استخدم لاعادة تاهيل اثنا عشر عمود خرساني مسلح مقطعه العرضي مربع،والتي تضررت نتيجة التعرض الى لهب بدرجات حرارة عالية مختلفة تصل الى 300, 500 و 700مº , عدا نموذجين لم يتم حرقهما. ثم تم تحميلها محوريا لحد الفشل بعد تبريدها بصورة سريعة او تدريجية. تم تقسيم النماذج الى مجموعتين حسب محتوى الحديد الطولي $\rho= 0.0314$ and $\rho= 0.0542$. بعده تم اجراء خطوات اعادة التاهيل, والتي تضمنت لف جميع النماذج بطبقتين من CFRP . اظهرت النتائج ان النماذج المحروقة يمكن بكفاءة عالية اعادة تاهيلها باستخدام CFRP لانها توفر تقييد جيد للخرسانة في وسط العمود. كذلك زيادة في تحمل الاعمدة بحوالي 16, 34 و 44% للنماذج المحروقة بدرجة 300, 500 و 700مº والمبردة تدريجا على التوالي بينما كانت 44و 111% للنماذج المحروقة

في 500و 700م ولكن المبردة فجائيا . قابلية امتصاص الطاقة لكل نموذج بعد و قبل اعادة التاهيل اظهرت ارتفاع بمقدار 8% للنماذج غير المحروقة بينما كانت 10, 100و 250% للنماذجد المحروقة في 300, 500 و 700م° .

الكلمات الرئيسية: اعادة التاهيل ، عمود خرساني مسلح،CFRP، الحرارة العالية

1. INTRODUCTION

Columns are among the most important structural elements, as their collapse or damage affects the safety of the structure they support. Exposure of reinforced concrete buildings to an accidental fire may result in cracking and loss in the bearing capacity of their major components, i.e. slabs, beams, and columns. Structural engineers are faced with the challenge of developing efficient retrofitting techniques that enable restoring the structural integrity of RC columns exposed to intense fires for long periods of time. Increasing the confinement of the column is the most effective approach to retrofitting reinforced concrete columns.

The use of fiber reinforced polymer (FRP) composites for external reinforcement has proved to be a very effective means of strengthening and retrofitting reinforced concrete (RC) structures over the last two decades , **Jian-Guo D. et al., 2011.**

Many researchers have focused on circular shaped columns. As rectangular sections are not uniformly confined, they have recommended that the high stresses should be concentrated at the corners. Also, they have preferred to develop plastic hinges at the ends of the column, with FRP wraps being used over most of middle length of the column ,**Benzaid et al.,2008. Wang and Wu, 2008,** investigated the effect of corner radius on the performance of CFRP confined square columns. They concluded that the corner radius directly influences the efficiency of confinement of square columns. Their results showed that confinement provided by a jacket with sharp corners is insignificant in increasing column strength. Furthermore, most research has dealt with reinforced columns strengthened by FRP jackets against lateral seismic motion to find out how to improve their shear capacity ,**Yoshimura, et al.,2000.**

Yoshimura, et al.,2000, conducted an experimental study on the behavior of short RC columns strengthened externally by (CFRP). Eight different specimens measuring 150x150x300mm with no transverse ties were tested under constant gravity load and repeated lateral forces. It was concluded that brittle shear failure was prevented by using CFRP jackets.

Ye et al.,2002 , tested short square RC columns strengthened with CFRP under lateral cyclic loading. Two of the specimens were fully wrapped with continuous CFRP sheets along the column height, while four were wrapped with discontinuous CFRP wraps with different widths and spacings. The results showed that the ductile behavior of the strengthened specimens was better in comparison to that of those not treated.

The retrofitting of short square columns exposed to fire flame using fiber-reinforced polymer (FRP) materials has not been studied extensively. Therefore the objective of this study was to evaluate the performance of retrofitting short reinforced concrete columns exposed to fire flame. Twelve reinforced concrete column specimens were cast and exposed to fire flame at different temperatures. All the characteristics of the specimens are given in **Table 1** and **Fig.1.** In this study, these columns were retrofitted and strengthened by CFRP laminate then tested up to failure.

2. EXPERIMENTAL PROGRAM

2.1 Material Properties

- The coarse aggregate used was natural aggregate with a maximum grain size of 10mm.
- Glenium51: (modified polycarboxylic ether) was used as a water reducing and stabilizing agent with a specific gravity of 1.1, at 20^{o}C, pH = 6.5 as announced by the producer.
- Silica fume mineral admixture or micro silica composed of ultrafine, amorphous glassy spheres of silicon dioxide (SiO_2), produced by Crosfield Chemicals, Warrington, England. Properties are shown in **Table 2**.
- Deformed steel bars with diameters of 10mm and 12mm were used for longitudinal reinforcement. To reduce the effect of rebar tie confinement, tie reinforcement was provided by smooth 3 mm diameter bars spaced at 100mm. The mechanical properties are shown in **Table 3**.
- Unidirectional SikaWrap Hex-230C is an externally applied retrofitting system for RC columns. The properties of carbon fiber fabric SikaWrap Hex- 230C and epoxy based impregnating resin Sikadur-330 are shown in **Tables 4.** and **5.** as announced by the manufacturer**.**

2.2 Concrete Mix Proportions

The mix proportions used were 1:1.5:1.6 with a water cement ratio of 0.5 in addition to 3 liters of glenium-51 admixture for each 100kg of cement. The mixture proportions are summarized in **Table 6**.

The slump flow for the self-compacting concrete was 685mm (using cone test ASTM C1611-05) and the slump test for the normal concrete was 100mm (ASTM C143-00).

2.3 Setting up the Column Specimens

Twelve approximately 1/4 scale models of reinforced concrete columns were cast. The overall length was 700 mm and the cross-sectional area was 100 x 100 mm, as shown in **Fig. 1-A**, and reinforced with four longitudinal steel bars, see details in **Table 1**. The ties consisted of 3mm diameter smooth bars spaced at 100mm in all specimens with a clear cover of 6mm. All column specimens were fitted with a top and bottom bearing hat with a square tie ring made of 2mm thick steel plate to prevent end bearing failure and ensure that the loads were distributed uniformly over the column ends. To prevent differences in concrete strength between the specimens, the latter were all cast at the same time.

Two column specimens were left unburned as control specimens C_1 and C_7. The other specimens were burned in a furnace constructed of 3mm thick steel plate, as shown in **Fig. 2**. One column was burned at a time with three control cube specimens (100mm x 100mm x 100mm). Also three cubes were used to determine the strength of the concrete before burning. Furnace dimensions were: height: 800mm; width: 500mm; length: 400mm. These dimensions were appropriate for the dimensions of the specimens, to maintain enough space to allow the flames to reach them from the fire sources (nozzles). The nozzles were positioned eccentrically, four on each side of the furnace, as shown in **Fig. 2-A**, to distribute the fire flame over the entire height of the specimen. The specimen was rotated and positioned in the furnace, as shown in

Fig. 2-B to direct the flames from a series of methane burners positioned on two sides of the furnace onto the four faces of the specimen.

The specimens were cast, then moist cured for seven days after which they were air dried in the laboratory. Ten specimens were subjected to burning by fire flame at age 45 days at three temperature levels, 300, 500 and 700$^{\circ}C$, as described in **Table 1.** for similar exposure periods of 1 hour after reaching the target temperature. After this period, the fire flame was turned off, the steel case of the furnace removed and the specimen was cooled gradually by leaving it in the air or suddenly by splashing it with water till reaching normal temperature. The temperature was monitored using digital thermometers inside the furnace and a Nickel-Chromium thermocouple wire (Type K) covered with cement to resist the temperature, with a digital temperature reader. Afterwards, the specimens were loaded till failure in the structural lab of Al-Mustanseria University. The results are shown in **Table 7**.

2.4 Retrofitting Procedure

Column specimens damaged by exposure to the fire flame were loaded till failure after cooling. Cracks had formed throughout the burning and cooling processes, and spalling of the concrete covers had occurred, especially at corners. This phenomenon was observed at high temperature exposure of 700$^{\circ}C$,**Khoury , 2000**. Also some specimens spalled during the loading stages. Furthermore, the color of the concrete had changed to pink, perhaps due to the hydration of iron oxide and other minerals in the cement and the aggregate ,**Nevile,1995**, as shown in **Fig 3**. Failure of the burned concrete specimens occurred in all cases due to crushing under different axial loads, as shown in **Table 7.** and **Fig. 4**.

As shown in **Fig.5** the retrofitting procedure was as follows:
The unsound concrete was removed by using a steel brusher and the surface of the concrete was cleaned of all pink and sooty damaged concrete and any dust. Then the reinforcement was repositioned in its original place and ties were fixed. The damaged concrete that had been removed was replaced with concrete having the same mix properties. After 28 days, the corners of the column specimens were chamfered (rounded) at a width of 15 mm by grinding.

Two-component epoxy impregnation resin was mixed by hand according to the manufacturer’s instructions and applied to the prepared concrete surfaces by brush. The fabric carbon fibers were cut out and wrapped around the specimen. A roller was used parallel to the direction of the fabric until the resin was squeezed between and through the carbon fibers. Two layers of CFRP were wrapped around the entire length of the column. According to the manufacturer’s instructions, the CFRP fabric sheet must be covered by a second layer of epoxy.

The retrofitted column specimens were left for about ten days at lab temperature before loads were applied.

The column specimens were tested in the rig shown in **Fig.6** using a testing machine with a 100 ton hydraulic jack capacity.

3. RESULTS AND DISCUSSION

3.1 Maximum Load Bearing Capacity

The results showed that concrete compressive strength decreased as exposure to temperature increased. The average percentage of residual compressive strength after exposure to 300, 500 and 700 $^{\circ}$C was 82%, 65% and 43%, respectively, for the specimens cooled gradually. The results agreed with those obtained by other researchers for normal concrete,**Nevile and Brooks,1987** . The decrease in the compressive strength of concrete was due to the breakdown of interfacial bonds caused by the change in volume between the concrete components during heating and cooling, ,**Venecanin,1977**. However, for the specimens cooled suddenly (high cooling rate), the residual compressive strength was slightly lower, with 61% 39% for exposure to temperatures of 500 and 700 C°, respectively. The results are shown in **Table 8**.

Column number **2** in **Table 7.** shows that the ultimate axial load capacity before retrofitting decreased with increasing fire flame temperature. At burning temperature levels of 300, 500 and 700 ºC, the average residual ultimate load capacities for gradually cooled specimens were 95%, 81% and 74%, respectively. As the temperature increased, the number of cracks and crack growth also increased. This led to lower bond strength between the concrete components as well as between the concrete and the reinforcing bars due to the difference in the thermal expansion coefficients of these different materials. The steel expanded while the concrete was subject to shrinkage. At 500 $^{\circ}$C and for the same longitudinal reinforcement ratio, the ultimate load capacities of the specimens cooled rapidly were lower than those of the specimens cooled gradually, by about 5% for C_4 in comparison to to C_3 and 10% for C_{10} in comparison to C_9. At 700 $^{\circ}C$ the two longitudinal reinforcement ratios of the specimens cooled suddenly were about 32% lower than those of the specimens cooled gradually.

After retrofitting, **Table 7.** (column number **3**) shows the ultimate load capacity. By comparing each column specimen with its non burned control specimen as shown in (column number **4**), the ratio was higher than that before retrofitting (column number **2**). The values for the specimens burned at temperatures of 300, 500 and 700 $^{\circ}$C, and for gradually cooled specimens were 95%, 93% and 87% respectively. However for the retrofitted specimens cooled suddenly, it was slightly lower than that for the gradually cooled ones, by about 2% for specimens C_6 and C_9 in comparison to C_5 and C_{10}, respectively. This means the confinement of the two wrapped CFRP sheet layers improved the ultimate load capacity of the columns.

The comparison (column number **5**) for each specimen with the control specimen before burning shows an increase in ultimate load capacity. Except for column specimens C_{11} and C_{12}, there was a slight decrease of about 3%. Whatever the case, this was higher than that before retrofitting, as shown in (column **2**). This was due to the greater damage caused by the destruction of bonds between the inner composition of the concrete in the first period of burning and cooling. However, the ratios of ultimate load capacity were 97% and 96% for C_{11} and C_{12}, respectively, which can be considered to be higher than that of 74% and 48%, respectively, before the retrofitting of the same specimens. This finding means that a retrofitting system using CFRP fabric sheets enhances the ultimate load capacity of the columns.

The last column in **Table 7.** shows the improvement in the ratio of each specimen before and after retrofitting (confinement efficiency). In specimens C_2 and C_8 the ratios were 17% and 14% respectively, which are the lowest because these two specimens had been subject to the least damage due to burning effects. This average ratio increased as the burning temperature increased: it was 34% and 44% for the specimens burned at 500 and 700 C°, respectively, and gradually cooled. Also, it was 44% and 111% for the specimens subjected to the same burning temperature cooled but suddenly. Therefore, confinement by CFRP results in improved compressive strength of the burned and damaged concrete.

3.2 Column Specimen Failure Mode (Failure Mechanism)

Cracks could not be monitored due to the CFRP sheets wrapping the entire height of the specimens. Failure was sudden in all the specimens, with the explosion of the CFRP sheet and the destruction of the concrete core, as reported by ,**Ogata and Osada, 2000 and ,Massone, and Wallace, 2004** . However, this happened after recording a large scale of axial deformation compared to that recorded after burning and before using the CFRP sheets for retrofitting the specimens.

Failure occurred suddenly in a rapid progressive process. It was not possible to determine which event occurred before the other, namely the explosion of the CFRP wrapping, the crushing of the concrete core or the rapid buckling of the longitudinal steel reinforcement. **Fig. 7** shows the failure of retrofitted specimens with the same longitudinal reinforcement: C_1, C_2, C_5 and C_7. The control column specimens not exposed to fire flame are compared to the specimens exposed to different temperature levels, 300, 500 and 700 respectively. Specimens that exploded laterally after smashing the CFRP sheets of all the column specimens were recorded. Failure was more explosive and sudden in specimens C_5 and C_7 than that in specimen C_1. This means that the damage to concrete increases when increasing the exposure temperature, causing a greater burden on the CFRP sheet confining the column. Also, in most of the specimens, failure was observed at the outer, upper or lower third of the column, due to the flow of the axial stresses transmitted from the end bearing toward the middle of the column.

Axial deformation caused the specimens to expand laterally. After the first earlier loading period, this deformation occurred along with the destruction of the CFRP sheets as the load applied was increased. The epoxy-CFRP-epoxy sandwich behaved like a stiff, brittle composite layer. The load was shared by the rehabilitated concrete and the CFRP layers wrapped around it. The axial load was transmitted by the shear stress from the reinforced concrete core to the CFRP jacket. As load was increased and the specimen shortened (axial deformation), lateral deformation increased, acting on the CFRP which reacted by confining the concrete. On the other hand, the applied axial load was shared between the reinforced concrete column and the composite CFRP fabric sheet. Obviously, the composite CFRP fabric sheets had very little axial compressive stiffness, because of their small thickness in comparison to the concrete column. This caused the epoxy layer to break. Thus the main component of the composite sheet was the uniaxial fibers of the CFRP, which could not bear any axial compression load. Therefore the contribution of the axial load applied on the CFRP composite sheet was borne by the epoxy alone; however this value is so small it can be ignored. Thus, when a CFRP confined concrete column is subjected to axial load, the CFRP wrapping jacket is loaded by hoop tension while the concrete is subjected to triaxial compression ,**Nicolae, and Gabriel,2008.**

3.3 Load-axial Deformation Curves:

Figs. 8 and 9 show the axial load deformation curves for the retrofitted column specimens versus the specimens reinforced with 8 longitudinal bars (4xØ10mm and 4xØ12mm).. The curves show an almost linear relationship, as recorded by **Triantafillou, 2003**, but the slope of the curves near the ultimate load fell little. Also, the figures show that the stiffness of the specimens decreases with increased exposure to fire flame temperature. As shown in **Fig. 8**, the stiffness of column specimen C_2 burned at 300ºC, is slightly lower than that of unburned specimen C_1. While in **Fig .9**, for the same compression between specimens C_8 and C_7, stiffness was approximately the same with a slight difference near ultimate load capacity. In both **Figs. 8 and 9**, the stiffness of the retrofitted column specimens decreased with increasing exposure temperature. **Fig. 8** shows that the percentage decreases in stiffness in comparison to the retrofitted unburned specimen C_1, were 5, 17, 24, 24 and 28% for specimens C_2, C_3, C_4, C_5 and C_6, respectively. While with the same comparison in **Fig. 9**, the percentage decreases were lower, with 2, 15, 21, 19 and 23% for specimens C_8, C_9, C_{10}, C_{11} and C_{12}, respectively, with respect to C_7. This means that the confinement by the CFRP jacket becomes the main reinforcement and delays buckling.

The stiffness of the retrofitted specimens increased in comparison to the same specimens before retrofitting. **Figs. 10 to 15** show the difference in stiffness before and after retrofitting the column specimens exposed to the same burning conditions. The average difference was 10% for the specimens not exposed to fire flame and 14, 12, 10% for specimens exposed to 300, 500 and 700 ºC, respectively**. Sandeep et al., 2007,** concluded that CFRP helps to increase strength without excessive increase in stiffness.

Comparing the modulus of toughness of each column specimen (defined as the area under the curve) before and after retrofitting permits determining the material's capacity to absorb energy. As shown in **Figs.10 to 15,** the average improvement in modulus of toughness before and after retrofitting was 8% for specimens not exposed to fire flame and 10, 100, 250% for specimens exposed to 300, 500 and 700ºC respectively.

4. CONCLUSIONS

The test results showed that burned- damaged RC column specimens can be retrofitted efficiently by using CFRP wrap jackets, as they provide good confinement of the damaged concrete core.

- Comparing the ultimate load capacity of each specimen before and after retrofitting shows high confinement efficiency. In specimens C2 and C8, the ratio was 17% and 14%, respectively. This average ratio increased as burning temperature increased, it was 34% and 44% for the specimens burned at 500 and 700 Cº, respectively, and cooled gradually. Moreover, it was 44% and 111% for the same burning temperature but with sudden cooling Therefore CFRP confinement improved the compressive strength of the burned-damaged concrete core.
- The stiffness of the retrofitted specimens increased in comparison to the same specimens before retrofitting.
- Regarding the difference in stiffness before and after retrofitting the column specimens exposed to the same burning conditions, the average difference was 10% for the specimens not exposed to fire flame and 14, 12, 10% for specimens exposed to 300, 500 and 700ºC, respectively.
- Furthermore, the stiffness of the retrofitted specimens decreased with increasing exposure to fire flame temperature. The percentage decreases in stiffness in comparison to the retrofitted unburned specimen C_1, were 5, 17, 24, 24 and 28% for specimens C_2, C_3, C_4, C_5 and C_6, respectively, for specimens with $\rho = 0.0314$ bars (main longitudinal reinforcement ratio). Regarding the same comparison for specimens with $\rho = 0.0542$ bars, the percentage decrease was lower, with 2, 15, 21, 19 and 23% for specimens C_8, C_9, C_{10}, C_{11} and C_{12}, respectively, in comparison to C_7. This means that the confinement by a CFRP jacket strengthens the main reinforcement and delays its buckling.

- Comparing the modulus of toughness (ability of to absorb energy) of each column specimen before and after retrofitting showed an improvement. The average improvement in modulus of toughness before and after retrofitting was 8% for specimens not exposed to fire flame and 10, 100, 250% for specimens exposed to 300, 500 and 700ºC, respectively.

REFFERENCES

- Al Kafaji, M., 2010, *Effect of Burning on Load Carrying Capacity of Reinforced Concrete Columns*, Ph.D. Thesis Presented to the University of Baghdad.
- Benzaid, R., Chikh, N.E. and Mesbah, H., 2008 *Behaviour of Square Concrete Columns Confined with GFRP Composite Wrap*, Journal of Civil Engineering and Managament, Vol. 14, No. 2, pp115-120.
- Jian-Guo, D. , Lik, L., and Tamon U., 2011, *Seismic Retrofit of Square RC Columns with Polyethylene Terephthalate (PET) Fibre Reinforced Polymer Composites Construction and Building Materials*, 27 (2012) 206–217, www.elsevier.com/locate/conbuildmat.
- Khoury, K. O., 2000, *Effect of Fire on Concrete and Concrete Structure*, Progress in Structure Engineering and Materials, pp429-447.
- Massone, L. M., and Wallace, J. W., *2004*, *Load-deformation Responses of Slender Reinforced Concrete Walls*, ACI Structural Journal, 101(1):103–13.
- Nevile, A. M., 1995, *Properties of Concrete*, Longman group, Ltd., 4th and final edition, pp388.
- Nevile, A. M. and Brooks, J. J., *1987*, *Concrete Technology*, First Edition, P318.
- Nicolae, T., and Gabriel, O., March 2008, *Fibre Reinforced Polymer Composities as Internal and External Reinforcement for Building Elements*, Technical University, Jassy, Departement of Civil and Industrial Engineering.
- Ogata, T., Osada, K., 2000, *Seismic* retrofitting of expressed bridges in Japan. Cem Concr Compos; 22, pp. 17–27.
- Sandeep, S. , Pendhari, Tarun Kant, Yogesh M. Desai, 2007, *Application of Polymer Composites in Civil Construction*: A general review , www.elsevier.com/locate/ compstruct
- Triantafillou, T. C. 2003, *Seismic Retrofitting using Externally Bonded*
- *Fibre Reinforced Polymers*, (FRP", fib course, 4-5, Athens, ttriant@upatras.gr.
- Venecanin, S.D., 1977, *Influence of Temperature on Deterioration of Concrete in the Middle East*, Concrete Journal, V.11, No.8, Augest, pp31-33.
- Wang, L.M., and Wu, Y.F., 2008, *Effect of Corner Radius on the Performance of CFRP Confined Square Concrete Columns:Test* ,Engineering Structures, 30, , pp 493-505.
- Ye, L., Yue, Q., Zhao, S., and Li, Q., 2002, *Shear Strength of Reinforced Concrete, Columns Strengthened with Carbon-Fiber-Reinforced Plastic Sheet.* ASCE Journal of Structural Engineering ,128(12):pp.1527–1534.

- Yoshimura, K, Kikuchi, K., Kuroki, M., Ozawa, K., and Masuda, Y., *2000* , *Experimental Study on Seismic Behavior of R/C Short Columns Strengthened by Carbon Fiber Sheets.in: Composite and Hybrid Structures:* Proceedings of the sixth ASCCS international conference on steel–concrete composite structures, pp. 927–934.

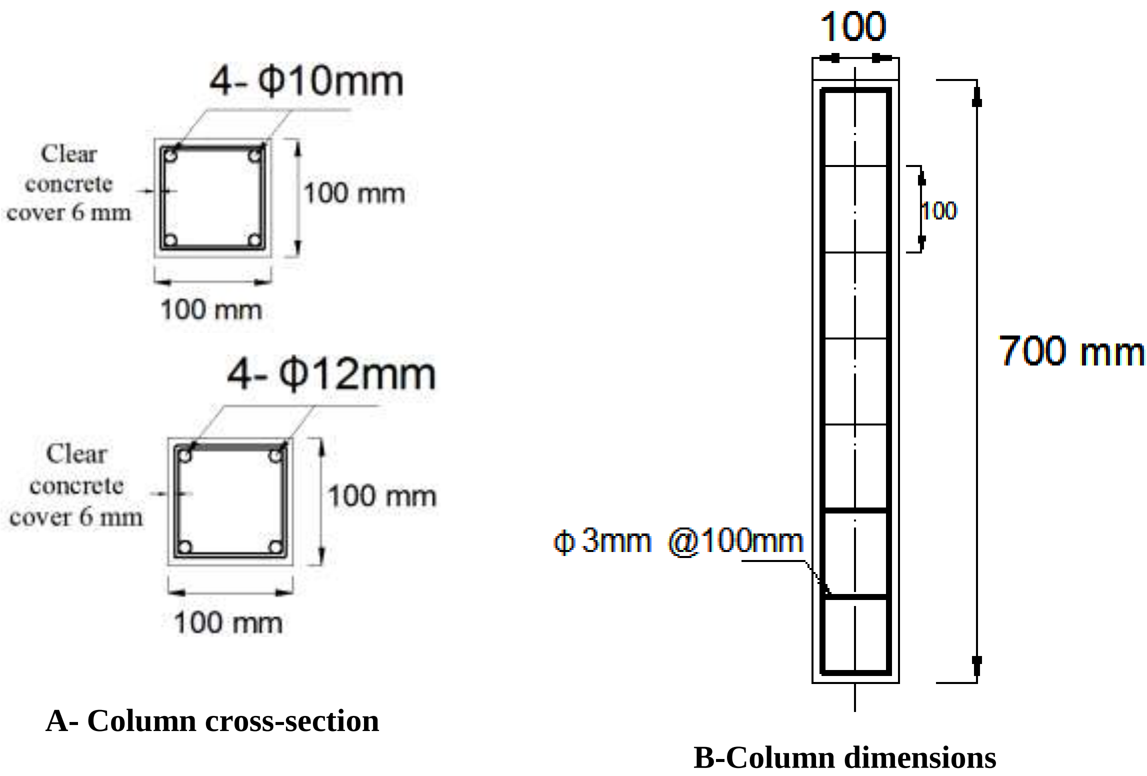

Figure 1. Details of dimensions and reinforcement of concrete column specimens.

A- furnace with nozzles

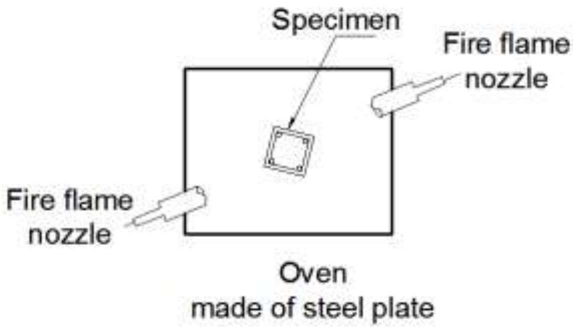

B- Specimen positioning in the furnace

Figure 2. Details of furnace, distribution of the nozzles and specimen position in the furnace during burning

A- Column specimen C_4 after exposure to 500 $^{\circ}C$ and cooled suddenly

B- specimen C_6 after exposure to 700 $^{\circ}C$ and cooled suddenly

C- specimen C_5 after exposed to 700 $^{\circ}C$ and cooled gradually

Figure 3 . Crack formation at different conditions of cooling and exposure temperature before the loading test.

A- Column specimen C_5

B- Column specimen C_6

A- Column specimen C_{11}

B- Column specimen C_{12}

Figure 4. Failure mode of several column specimens after burning and loading till failure

A-Brushing the concrete to remove unsound materials and dust.

B-Repositioning the main reinforcement **C-** Rounding of columns corners
rounding

D-Replacement of **E-** Wrapping the CFRP fabric sheet using a roller
damaged concrete to coat the CFRP Sheet with additional epoxy layer

Figure 5. Column specimen retrofitting procedure.

Figure 6. Test set-up ,Structural Lab - University of Al-Mustanseria.

A-Column specimen C_1

B- Column specimen C_2

C- Column specimen C_5

D- Column specimen C_7

Figure 7. Failure of column specimens by rupturing of the two layers of CFRP.

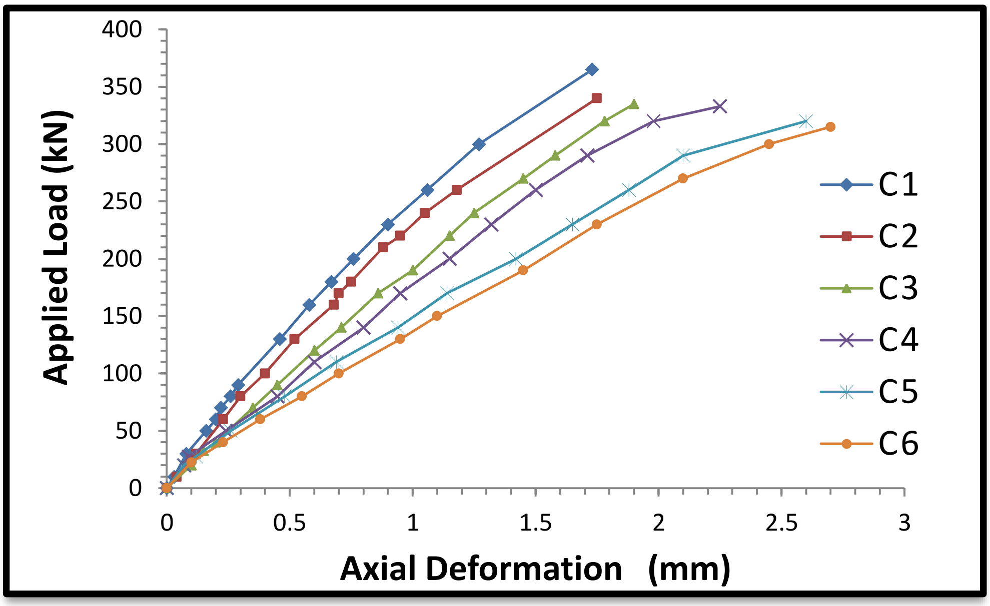

Figure 8. Load-Axial deformation curves for specimens with (4-*Ø10mm*) longitudinal bars . After retrofitting with CFRP fabric sheet.

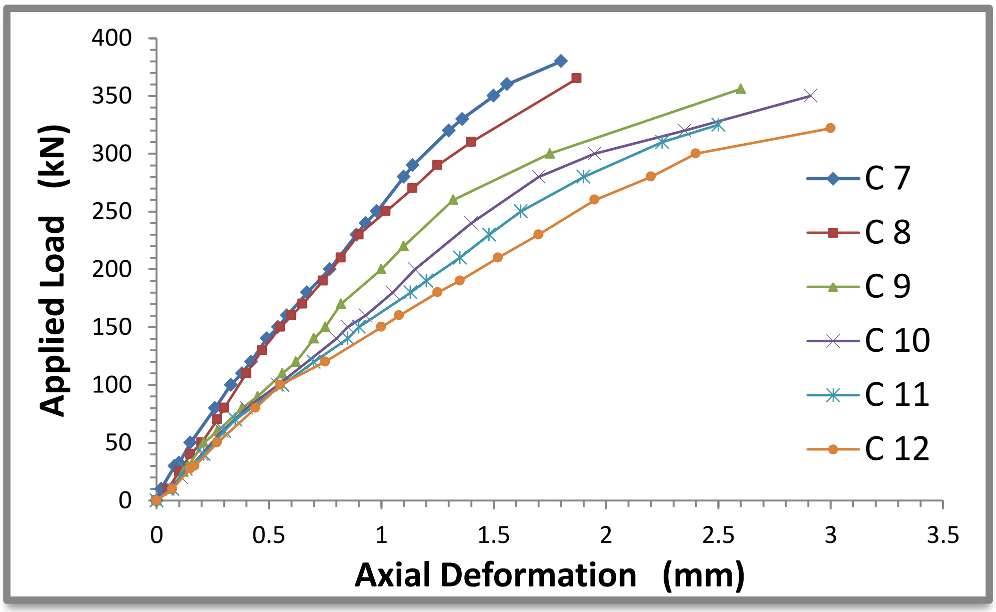

Figure 9. Load-Axial deformation curves for specimens with (4-*Ø12mm*) longitudinal bars
After retrofitting with CFRP fabric sheet.

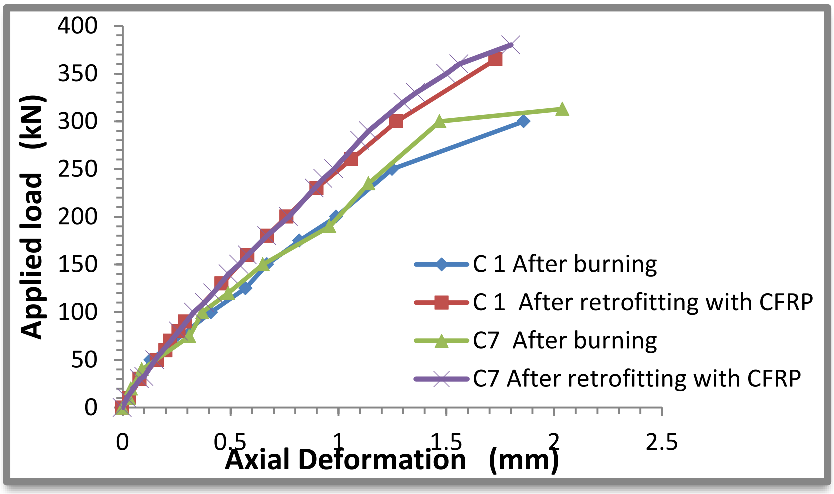

Figure 10. Load-Axial deformation curves for unburned column specimens After retrofitting with CFRP fabric sheet.

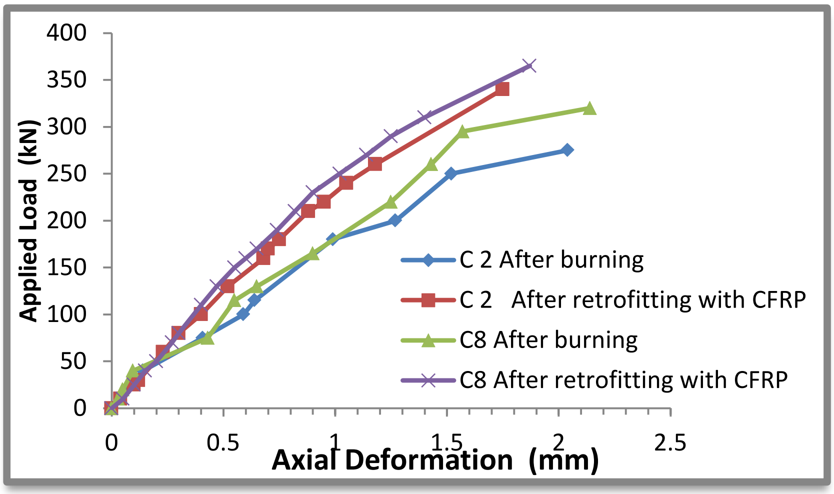

Figure 11. Load-Axial deformation curves for column specimens exposed to 300ºC After retrofitting with CFRP fabric sheet.

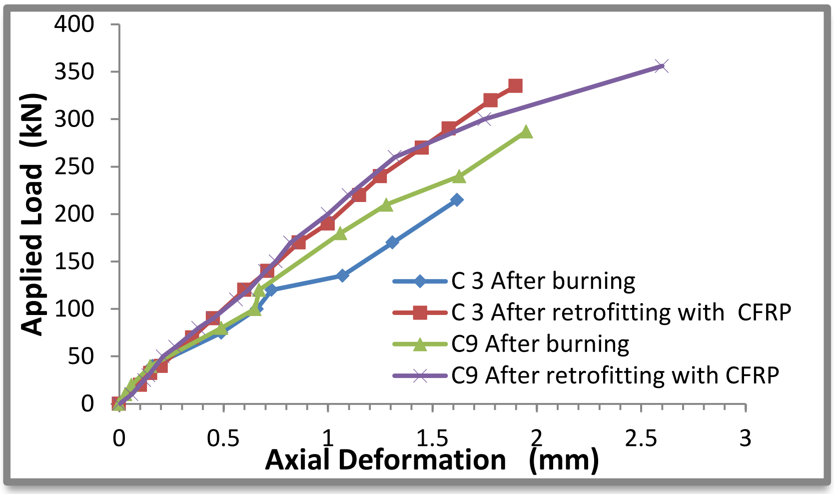

Figure 12. Load-Axial deformation curves for column specimens exposed to 500ºC and cooled gradually
After retrofitting with CFRP fabric sheet.

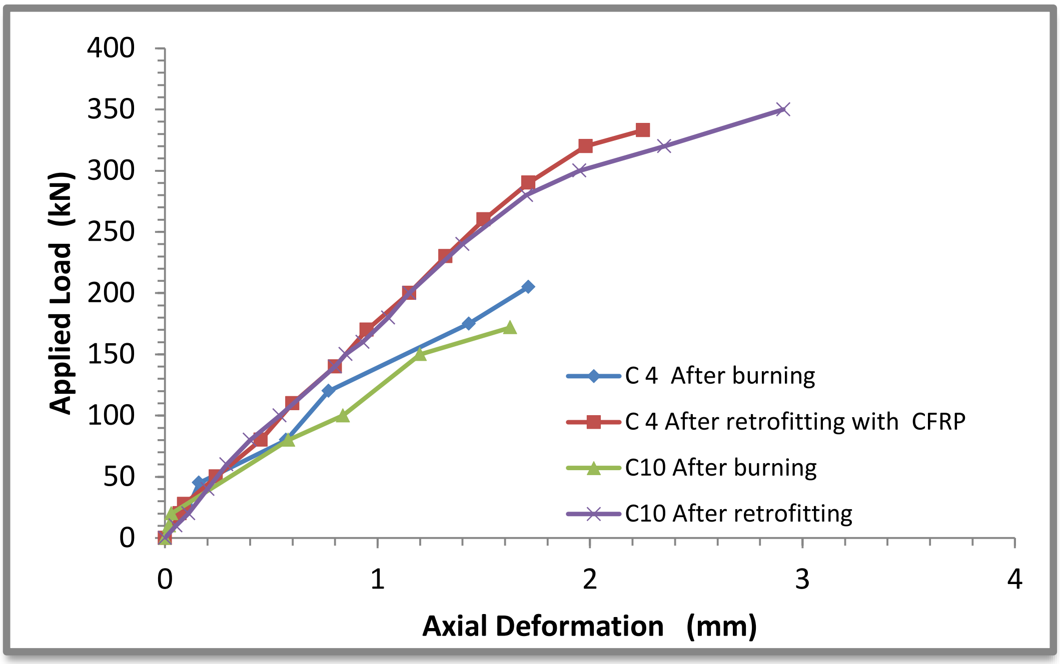

Figure 13. Load-Axial deformation curves for column specimens exposed to 500ºC and cooled suddenly
After retrofitting with CFRP fabric sheet.

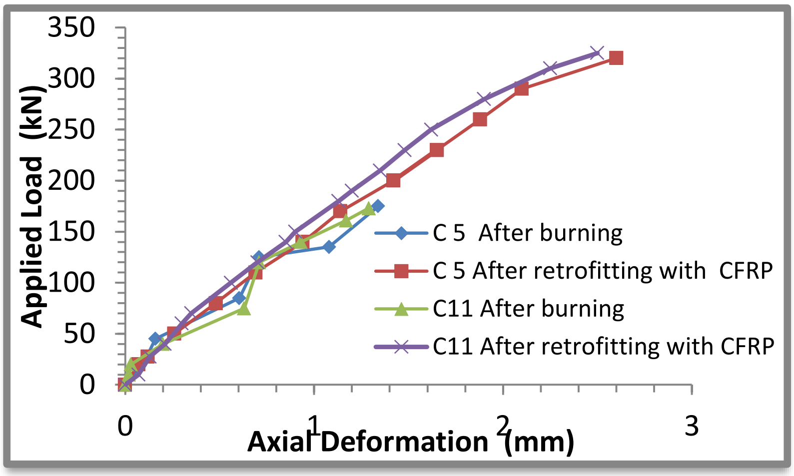

Figure 14. Load-Axial deformation curves for column specimens exposed to 700ºC and cooled gradually
After retrofitting with CFRP fabric sheet.

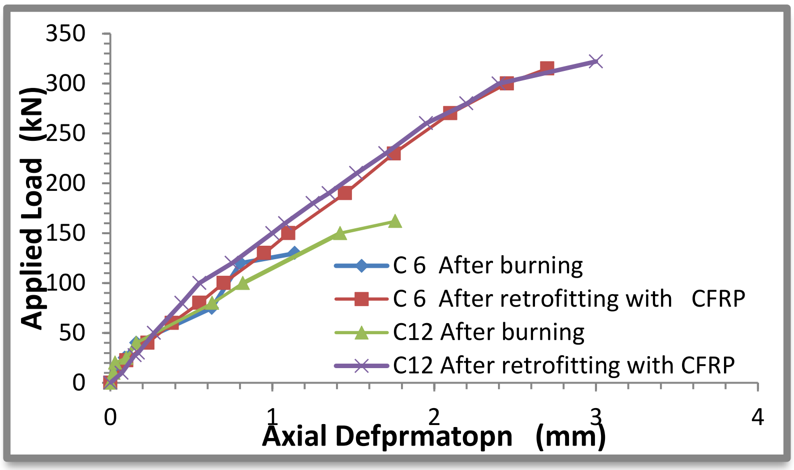

Figure 15. Load-Axial deformation curves for column specimens exposed to 700ºC and cooled suddenly
After retrofitting with CFRP fabric sheet.

Table 1. Details of the column specimens.

Column designation	Longitudinal reinforcement	Longitudinal bar diameter (mm)	Tie reinforcement	Burning temperature C	Type of cooling
C1	4 –Ø10mm.	10	Ø3mm / 100mm	-	-
C2	4 –Ø10mm.	10	Ø3mm / 100mm	300	gradual
C3	4 –Ø10mm.	10	Ø3mm / 100mm	500	gradual
C4	4 –Ø10mm.	10	Ø3mm / 100mm	500	sudden
C5	4 –Ø10mm.	10	Ø3mm / 100mm	700	gradual
C6	4 –Ø10mm.	10	Ø3mm / 100mm	700	sudden
C7	4 –Ø12mm.	12	Ø3mm / 100mm	-	-
C8	4 –Ø12mm.	12	Ø3mm / 100mm	300	gradual
C9	4 –Ø12mm.	12	Ø3mm / 100mm	500	gradual
C10	4 –Ø12mm.	12	Ø3mm / 100mm	500	sudden
C11	4 –Ø12mm.	12	Ø3mm / 100mm	700	gradual
C12	4 –Ø12mm.	12	Ø3mm / 100mm	700	sudden

- All specimens were made of SCC: self-compacting concrete.
- Average concrete strength before burning was 49MPa for the cubes 100 x 100 x 100mm.
- Steel reinforcement ratio $\rho = 0.0314$ for specimens with 4-Ø10mm longitudinal bars.
- Steel reinforcement ratio $\rho = 0.0452$ for specimens with 4-Ø12 longitudinal bars.
- The period of exposure temperature was one hour after reaching the target temperature.
- Sudden cooling was done by splashing with water till reaching normal temperature.

Table 2. Chemical and physical properties of Silica fume.

Properties	SikaWarp® Hex-230C
SiO_2	90 %
SO_3	0.15 %
Cao	0.8 %
Surface area	25000-28000
Grading below 1µm	90%

Table 3. Mechanical properties of steel bars.

Bar diameter (mm)	Yield stress (MPa)	Strain at yield stress (microstrain)	Ultimate stress (MPa)
3	542	2710	632
10	512	2497	622
12	504	2571	618

Table 4. Technical properties of CFRP sheets [manufacturer's data].

Properties	SikaWarp® Hex-230C
Tensile strength (MPa)	4100
E-modulus (GPa)	230
Elongation at break (%)	1.7
Width (mm)	300/600
Thickness (mm)	0.12

Table 5. Technical properties of impregnation resin [manufacturer's data].

Properties	Sikadur®-330
Tensile strength , MPa	30
Density	1.30kg/l$_{\pm.1}$ kg/l
E-modulus , GPa	4.5
Open time , min.	30 (at +35^{o}C)
Full cure , days	7(at +35^{o}C)
Mixing ratio	1:4
Elongation at break	0.9%

Table 6. Concrete mix proportions.

Contents of Materials		
Water	kg/m^3	200
Superplasticizer	lit./100kg (powder)	3
Cement	kg/m^3	392
Silica fume	kg/m^3	8
Total powder	kg/m3	400
Gravel	kg/m3	640
Sand	kg/m3	600

Table 7. Columns test results.

Column designation	After Burning		After Retrofitting			Load capacity after Retrofitting / load capacity after burning before retrofitting
	1	2	3	4	5	
	Ultimate load capacity kN	Load capacity /reference column %	Ultimate load capacity kN	Load capacity /reference column %	Load capacity /reference column **£** %	
C1	305 **£**	100	365	100	120	1.20
C2	290	95	340	93	111	1.17
C3	232	76	335	92	110	1.44
C4	220	72	333	92	109	1.51
C5	207	68	320	88	105	1.55
C6	142	46	315	86	103	2.22
C7	335 **£**	100	380	100	113	1.13
C8	320	96	365	96	109	1.14
C9	287	86	356	94	106	1.24
C10	258	77	350	92	104	1.36
C11	247	74	325	86	97	1.32
C12	162	48	322	85	96	1.99

£ Reference Column not exposed to fire flame

Table 8. Cube compressive strength before and after exposure to high temperature.

Burning temperature C°	Type of cooling	Compressive strength MPa	Residual compressive strength %
-	-	49	100
300	gradual	40	82
500	gradual	32	65
700	gradual	21	43
500	sudden	30	61
700	sudden	19	39

- The results are average of three cubes

Multi-Sites Multi-Variables Forecasting Model for Hydrological Data using Genetic Algorithm Modeling

Prof. Dr. Rafa H. Al-Suhili
The Senior Prof. of the Civil Engineering Dept., University of Baghdad, Baghdad, Iraq
A Visiting Prof. to the City College of New York, New York, USA.
Email:rafeaalsuhili@yahoo.com

ABSTRACT

A two time step stochastic multi-variables multi-sites hydrological data forecasting model was developed and verified using a case study. The philosophy of this model is to use the cross-variables correlations, cross-sites correlations and the two steps time lag correlations simultaneously, for estimating the parameters of the model which then are modified using the mutation process of the genetic algorithm optimization model. The objective function that to be minimized is the Akiake test value. The case study is of four variables and three sites. The variables are the monthly air temperature, humidity, precipitation, and evaporation; the sites are Sulaimania, Chwarta, and Penjwin, which are located north Iraq. The model performance was checked by comparing it's results with the results of six forecasting models developed for the same data by Al-Suhili and khanbilvardi, 2014.The check of the performance of the new developed model was made for three forecasted series for each variable, using the Akaike test which indicates that the developed model is more successful, since it gave the minimum (AIC) values for (91.67 %) of the forecasted series. This indicates that the developed model had improved the forecasting performance. For the rest of cases (8.33%), other models gave the lowest AIC value, however it is slightly lower than that given by the developed model. Moreover the t-test for monthly means comparison between the models indicates that the developed model has the highest percent of succeed (100%).
Keywords: forecasting, multi-sites, multi-variables, cross sites correlation, serial correlation, cross variables correlations, hydrology.

نموذج تنبأ بالمعلومات الهيدرولوجية متعدد المواقع ومتعدد المتغيرات باستخدام تقنية الجينات الوراثية

رافع هاشم السهيلي
استاذ
كلية الهندسة- جامعة بغداد

الخلاصة

تم في هذا البحث اشتقاق نموذج تنبأ بالبيانات الهيدرولوجية متعدد المواقع متعدد المتغيرات ويعتمد على خطوتين زمنيتين وتم برهنته باستخدام حالة دراسية. ان فلسفة هذا النموذج تعتمد على استخدام معاملات الأرتباط بين المتغيراتوبين المواقع ومعاملات الأرتباط الزمني لخطوتين زمنيتين سابقتين بشكل اني لأيجاد معاملات النموذج ومن ثم يتم تغيير قيمها باستخدام عملية المعايرة الخاصة بتقنبة الجينات الوراثية . كما هو معروف هن تقنية الجينات الوراثية هي تقنية تستخدم لأيجاد القيمة المثلى لدالة الهدف حيث ان الالة المستخدمة هنا والتي يتم ايجاد القيمة الصغرى لهى هي دالة اختبار اكايكي. ان الحالة الدراسية المأخوذة هس لأربع متغيرات في ثلاث مواقع . المتغيرات هي درجة حرارة الهواء والرطوبة والسقيط والتبخر الشهرية والمواقع هي السليمانية وجوارتة وبنجوين التي تقع في شمال العراق. تم مقارنة اداء النموذج مع نتائج ستة نماذج تنبأ ولنفس حالة الدراسة. هذه المقارنة تمت لثلاثة متسلسلات زمنية لكل متغير في كل موقع تم التنبأ بها بستخدام كل من النماذج الستة السابقة والنموذج الجديد وباستخدام الأختبار المشار اليه اعلاه واشارت النتائج بان النموذج الجديد اكثر نجاحا لانه اعطى اقل قيم للأختبار بنسبة 91.76 %. وهذا يدل على ان النموذج الجديد قد حسن عملية التنبأ.

الكلمات الرئيسية: التنبؤ، مواقع متعددة، متغيرات متعددة، ارتباط المواقع المتقاطعة، ارتباط متسلسل، ارتباط المتغيرات المتقاطعة، هيدرولوجي.

1. INTRODUCTION

Forecasting models of hydrological data series have been used successfully for different water resources studies. By now it is used in different research topics, including, water resources projects planning and design, climate changes studies and reservoirs operation. They can generate series of climatic data that reflects the same statistical properties as the observed ones. Moreover, weather generators are able to produce series for longer length in time than the observed ones, and hence gives much more significance on the decision making process. This allows a better identification of the consequences of extreme events, such as extreme flood, extreme draught, and hence allowing sufficient water resources management to make the required preparations for the expected draught or flood events. Different types of forecasting models are available in the literature that can be used for weather data forecasting.

Single variable single site forecasting models (SVSS) are used for forecasting a hydrological variable at a single site independent of the same variable at the near sites ignoring the spatial dependence that may exist in the observed data. This model, also ignore the cross variables relations that may physically exist between these variables. Generally correlation between variables in different sites with different variables may exist in real applications**. ,Matals, 1967.** had developed a single variable multi-sites model (SVMS) using cross site correlations between one variable at different sites. This model can be applied as a multi-variable single site (MVSS) model that uses multi variables cross correlation in a given site. ,**Richardson, 1981.** had developed a multi-variables stochastic weather models for daily precipitation, maximum temperature, minimum temperature, and solar radiation, as cited in, ,**Wilks, 1999.** The Multi-variables models are similar to the multi-sites model but simulate the cross variables dependency that exists between some variables at a certain site. Recently progress had been made especially in the last twenty years to come up with theoretical frameworks for spatial analysis ,**Khalili, 2007**. **Lee, et al., 2010.** had developed a space–time model to regionalize the weather generators. In these models, the precipitation is linked to the atmospheric circulation patterns using conditional probability distributions and conditional spatial covariance functions. The multi-site weather generators presented above are designed using relevant statistic information. Most of these models are either complicated or some are applicable with a certain conditions. There exist in the literature some relatively recent trials to account for the spatial variation in multi-sites, and variables correlations among different variables in the same site and in the other sites.

In a reliable hydrological system the cross variables and cross sites correlation may exist between different hydrological variables at different sites, in addition to the time lag correlations. ,**Al-Suhili, et al., 2010,** had presented a multivariate multisite model for forecasting different water demand types at different areas in the city of Karkouk, north Iraq. This model use in advance regression analysis to relate each demand type with explanatory variables that affect its type, then obtaining the residual series of each variable at each site. These residual are then modeled using a multisite, **Matalas, 1967,** models for each type of demand. These models were then coupled with the regression equation to simulate the multi-variables multi-sites simulation. The last two cited research are those among the little work done on forecasting models of multi-sites multi-variables types. However these model are rather complicated, and/or do not model the process of cross site, cross variables correlation and time lag correlation simultaneously, which as mentioned above is the real physical case that exist. Hence researches are further required to develop a simplified multi-sites multi-variables model. ,**Al-Suhili, and Mustafa, 2013,** had proposed a multi-variables multi-sites model that uses relative correlation matrix and a residual matrix as the model parameters to relate the dependent and independent stochastic components of the data. This model represents the dependent stochastic of each variable at a time step as a weighted sum of the dependent stochastic component at the preceding time step and the present independent stochastic components. However these weights are not summed to one, while logically they should be. ,**Al-Suhili, and Khanbilvardi, 2014,** had developed a model as modification of ,**Al-Suhili, and Mustafa model, 2013,** using one degree time step model and relative weighted correlations, with one time degree, and weights that sums to 1.

In this research a modified multi-variables multi-sites approach is proposed to develop a model that describe the cross variables, cross sites correlation and lag-time correlation structure in the forecasting of multi variables at multi sites simultaneously. This model represents a modification of ,**Al-Suhili, and Khanbilvardi model, 2014,** by extending the time dependence to the second degree, and apply the mutation process of the genetic algorithm model to these parameters, such that to minimize the Akaike test value. The modification is done such that the total weights of the lag 1 and lag 2 correlations and the residual correlations are summed to 1, i.e. each variable is resulted from the weighted sum of the other variables in the same site and those in the other sites in addition to the same and other variable at the preceding two time steps. This was done by adopting a different method for estimating the parameters of the model using lag 1 and lag 2, time correlations rather than using only lag 1 time correlation, moreover these parameters were then subjected to a mutation process of the genetic algorithm model but with keeping the sum of the weights to 1 as a constraint. The mutation process continues until minimizing the Akaike test value as an objective function. This model was applied to the same case study used by ,**Al-Suhili, and Khanbilvardi, 2014,** model for the sake of comparison. The case study is for the monthly data of four hydrological variables, air temperature, humidity, precipitation and evaporation at three sites located north Iraq, Sulaimania, Chwarta, and Penjwin.

2.THE MODEL DEVELOPMENT

The multivariate multisite model developed herein, utilizes single variable time lag one and lag two correlations, cross variables lag-one and lag- two correlations, and cross sites lag-one and lag-two correlations. In order to illustrate the model derivation consider **Fig. 1a,** where the concept of these correlations is shown, ,**Al-Suhili, and Khanbilvardi, 2014**. This figure illustrates the concept for two variables, two sites and first order lag-time model. This simple form is used to simplify the derivation of the model. However, the model could be easily generalized using the same concept. For instant, **Fig. 1b**, is a schematic diagram for the multi-variables multi-sites model of two variables, three sites and first order lag-time. The concept is that if there will be two-variables, two sites, and one time step (first order), then there will exist (8) nodal points. Four of these represent the known variable, i.e. values at time (t-1); the other four are the dependent variables, i.e. the values at time (t). As mentioned before, **Fig. 1**, shows a schematic representation of the developed model and was abbreviated as MVMS (V, S, O), where V: stands for number of variables in each site, S: number of sites, and O: time order, hence the model representation in figure (1a and b) can be designated as MVMS (2, 2, 1), and MVMS (2, 3, 1), respectively.

This model can be extended further to (V-variables) and / or (S-sites) and / or (O- time) order. The model concept assume that each variable dependent stochastic component at time t can be expressed as a function of the independent stochastic component for all other variables at time (t), and those dependent component for all variables at times (t-1)and (t-2) at all sites. The expression is weighted by the first two time lags serial correlation coefficients, cross-site correlation coefficients, cross-variable coefficients and cross-site, cross-variable correlation coefficients. In addition to that; the independent stochastic components are weighted by the residuals of all types of these correlations. These residual correlations are expressed using the same concept of autoregressive second order model (Markov chain). Further modification of this model is to use relative correlation matrix parameters by using correlation values relative to the total sum of absolute lag-1 and lag-2correlations for each variable, and the total sum of the absolute residuals as a mathematical filter ,as will be shown later.

A model matrix equation for second order time lag, O=2, number of variables=V, and number of sites=S, could be put in the following form:

$$[\epsilon_t]_{v*s,1} = [\phi 1]_{v*s,v*s} * [\epsilon_{t-1}]_{v*s,1} + [\phi 2]_{v*s,v*s} * [\epsilon_{t-2}]_{v*s,1} + [\sigma]_{v*s,v*s} * [\xi_t]_{v*s,1} \quad (1)$$

Which for V=2,S=3,and O=2, can be represented by the following equation:

$$[\epsilon_t]_{6,1} = [\phi 1]_{6,6} * [\epsilon_{t-1}]_{6,1} + [\phi 2]_{6,6} * [\epsilon_{t-2}]_{6,1} + [\sigma]_{6,6} * [\xi_t]_{6,1} \quad (2)$$

Where:

$$\begin{pmatrix} \epsilon_{(v1,s1)} \\ \epsilon_{(v2,s1)} \\ --- \\ \epsilon_{(v1,s2)} \\ \epsilon_{(v2,s2)} \\ --- \\ \epsilon_{(v1,s3)} \\ \epsilon_{(v2,s3)} \end{pmatrix}_{\mathbf{t}} = [\epsilon_t]_{6,1} \quad (3)$$

$$\begin{pmatrix} \epsilon_{(v1,s1)} \\ \epsilon_{(v2,s1)} \\ --- \\ \epsilon_{(v1,s2)} \\ \epsilon_{(v2,s2)} \\ --- \\ \epsilon_{(v1,s3)} \\ \epsilon_{(v2,s3)} \end{pmatrix}_{\mathbf{t-1}} = [\epsilon_{t-1}]_{6,1} \quad (4)$$

$$\begin{pmatrix} \epsilon_{(v1,s1)} \\ \epsilon_{(v2,s1)} \\ --- \\ \epsilon_{(v1,s2)} \\ \epsilon_{(v2,s2)} \\ --- \\ \epsilon_{(v1,s3)} \\ \epsilon_{(v2,s3)} \end{pmatrix}_{\mathbf{t-2}} = [\epsilon_{t-2}]_{6,1} \quad (5)$$

$$\begin{bmatrix} \xi_{(v1,s1)} \\ \xi\epsilon_{(v2,s1)} \\ --- \\ \xi_{(v1,s2)} \\ \xi\epsilon_{(v2,s2)} \\ --- \\ \xi_{(v1,s3)} \\ \xi\epsilon_{(v2,s3)} \end{bmatrix}_t = [\xi_t]_{6,1} \qquad (6)$$

$$\begin{pmatrix} \phi1_{1,1} & \phi1_{1,2} & \phi1_{1,3} & \phi1_{1,4} & \phi1_{1,5} & \phi1_{1,6} \\ \phi1_{2,1} & \phi1_{2,2} & \phi1_{2,3} & \phi1_{2,4} & \phi1_{2,5} & \phi1_{2,6} \\ \phi1_{3,1} & \phi1_{3,2} & \phi1_{3,3} & \phi1_{3,4} & \phi1_{3,5} & \phi1_{3,6} \\ \phi1_{4,1} & \phi1_{4,2} & \phi1_{4,3} & \phi1_{4,4} & \phi1_{4,5} & \phi1_{4,6} \\ \phi1_{5,1} & \phi1_{5,2} & \phi1_{5,3} & \phi1_{5,4} & \phi1_{5,5} & \phi1_{5,6} \\ \phi1_{6,1} & \phi1_{6,2} & \phi1_{6,3} & \phi1_{6,4} & \phi1_{6,5} & \phi1_{6,6} \end{pmatrix} = [\phi\ 1]_{6,6} \qquad (7)$$

$$\begin{pmatrix} \phi2_{1,1} & \phi2_{1,2} & \phi2_{1,3} & \phi2_{1,4} & \phi2_{1,5} & \phi2_{1,6} \\ \phi2_{2,1} & \phi2_{2,2} & \phi2_{2,3} & \phi2_{2,4} & \phi2_{2,5} & \phi2_{2,6} \\ \phi2_{3,1} & \phi2_{3,2} & \phi2_{3,3} & \phi2_{3,4} & \phi2_{3,5} & \phi2_{3,6} \\ \phi2_{4,1} & \phi2_{4,2} & \phi2_{4,3} & \phi2_{4,4} & \phi2_{4,5} & \phi2_{4,6} \\ \phi2_{5,1} & \phi2_{5,2} & \phi2_{5,3} & \phi2_{5,4} & \phi2_{5,5} & \phi2_{5,6} \\ \phi2_{6,1} & \phi2_{6,2} & \phi2_{6,3} & \phi2_{6,4} & \phi2_{6,5} & \phi2_{6,6} \end{pmatrix} = [\phi\ 2]_{6,6} \qquad (8)$$

$$\begin{pmatrix} \sigma_{1,1} & \sigma_{1,2} & \sigma_{1,3} & \sigma_{1,4} & \sigma_{1,5} & \sigma_{1,6} \\ \sigma_{2,1} & \sigma_{2,2} & \sigma_{2,3} & \sigma_{2,4} & \sigma_{2,5} & \sigma_{2,6} \\ \sigma_{3,1} & \sigma_{3,2} & \sigma_{3,3} & \sigma_{3,4} & \sigma_{3,5} & \sigma_{3,6} \\ \sigma_{4,1} & \sigma_{4,2} & \sigma_{4,3} & \sigma_{4,4} & \sigma_{4,5} & \sigma_{4,6} \\ \sigma_{5,1} & \sigma_{5,2} & \sigma_{5,3} & \sigma_{5,4} & \sigma_{5,5} & \sigma_{5,6} \\ \sigma_{6,1} & \sigma_{6,2} & \sigma_{6,3} & \sigma_{6,4} & \sigma_{6,5} & \sigma_{6,6} \end{pmatrix} = [\sigma\ ]_{6,6} \qquad (9)$$

Now if we define the followings:
$\rho1_{1,1}$ = ρ1 [(x1, x1), (s1, s1), (t, t-1)]= population serial correlation coefficient of variable 1 with itself at site 1 for time lagged 1

$\rho1_{1,2}$ = ρ1 [(x1, x2), (s1, s1), (t, t-1)]= population cross correlation coefficient of variable 1 at site 1 with variable 2 at site 1, for time lagged 1

$\rho1_{1,3}$ = ρ1 [(x1, x1), (s1, s2), (t, t-1)]= population cross correlation coefficient of variable 1 at site 1 with variable 1 at site 2, for time lagged 1

$\rho1_{1,6}$ = ρ1 [(x1, x2), (s1, s3),(t,t-1)]= population cross correlation coefficient of variable 1 at site 1 with variable 2 at site 3, for time lagged 1,
the definition continues for all the variables and all the sites. Similarly the lag 2 correlations are:

$\rho2_{1,1}$ = ρ2 [(x1, x1), (s1, s1), (t, t-2)]= population serial correlation coefficient of variable 1 with itself at site 1 for time lagged 2

$\rho2_{1,2}$ = ρ2 [(x1, x2), (s1, s1), (t, t-2)]= population cross correlation coefficient of variable 1 at site 1 with variable 2 at site 1, for time lagged 2

ϵ: is the stochastic dependent component.

ξ: is the stochastic independent component.

The coefficients of the matrices in Eqs. (7) (8) and (9) are estimated according to the correlation structure in the auto regressive models filtered by a division mathematical absolute summation filter, that makes the dependent component of each variable in each site at time t expressed as a weighted sum of the dependent components of the variables in the same site and the other sites at time steps t-1 and t-2 with additional weighted terms of the independent stochastic component of each variable and all sites. The following equations were resulted:

$$\boldsymbol{\phi 1_{i,j}} = \frac{\rho 1_{i,j}(1-\rho 2_{i,j})/(1-\rho 1_{i,j}^2)}{\sum_{j=1}^{n=v*s} abs\,(\rho 1_{i,j})+abs(\rho 2_{i,j})+abs(\sigma_{i,j})}. \tag{10}$$

$$\boldsymbol{\phi 2_{i,j}} = \frac{(\rho 2_{i,j}^2-\rho 1_{i,j}^2)/(1-\rho 1_{i,j}^2)}{\sum_{j=1}^{n=v*s} abs\,(\rho 1_{i,j})+abs(\rho 2_{i,j})+abs(\sigma_{i,j})}. \tag{11}$$

σ values are estimated using the following equation:

$$\boldsymbol{\sigma_{i,j}} = \frac{\left(1+\phi 2_{i,j}\right)(1-\phi 2_{i,j}^2-\phi 1_{i,j}^2)/\left(1-\phi 2_{i,j}\right)}{\sum_{j=1}^{n=v*s} abs\,(\rho 1_{i,j})+\mathrm{abs}(\rho 2_{i,j})+abs(\sigma_{i,j})}. \tag{12}$$

3.THE GENETIC ALGORITHM MODEL

The estimated parameters in Eqs. (7),(8), and (9), are considered as a first estimation and then subjected to a mutation process of the genetic algorithm technique. The mutation process was done by adding and/or subtracting small values to the parameters such that the absolute sum of each row in matrices,1,**ϕ**2,and σ, is kept to be 1. This is the constraint of the optimization process performed by the mutation process of the genetic algorithm technique and can be represented by the following equation, for the first variable at the first site.

$$\sum_{j=1}^{v*s}(\boldsymbol{\phi 1_{f,j}} \pm \boldsymbol{u1_{f,j}})+\sum_{j=1}^{v*s}(\boldsymbol{\phi 2_{f,j}} \pm \boldsymbol{u2_{f,j}}) + \sum_{j=1}^{v*s}(\boldsymbol{\sigma_{f,j}} \pm \boldsymbol{u3_{f,j}}) = 1 \tag{13}$$

With f=1, similar expression can be obtained for the other variables , by setting f=2,3, …,v*s.
And $\boldsymbol{u1_{f,j}}, \boldsymbol{u2_{f,j}}, \boldsymbol{u3_{f,j}}$: are the mutation levels of row f, and column j, of the **ϕ**1,**ϕ**2,andσ matrices, respectively.

The objective functions to be each minimized are the Akaike test value for each variable in each site as given by the following equation:

$$\boldsymbol{min\ AIC_f = 2K + n\ Ln\frac{Rss}{n}} \quad ,f=1,2,\ldots..v*s \qquad (14)$$

Where:
n: is the number of the total forecasted values .
K: number of parameters of the model plus 1.
Rss: is the sum of square error between the forecasted value and the corresponding observed value. If the values of Rss/n is less than one the AIC value may be negative and the performance is better if the absolute AIC value is larger.

This means that the minimization process is done for each variable and each site , using row by row process. The number of AIC functions to be minimized is v*s.

4.THE CASE STUDY AND APPLICATION OF THE MODEL

In order to apply the developed two degree time step, MVMS(4,3,2) model explained above the Sulaimania Governorate was selected as a case study, which is the same case study used by Al-Suhili and **Khanbilvardi, 2014,** as mentioned before. This was done in order to compare the results of the new developed model with the previous models which was applied by those authors for the same case study. The following description of this case study was fully taken from this refrence. Sulaimania Governorate is located north of Iraq with total area of (17,023 km2) and population, 2009**,** 1,350,000. The city of Sulaimania is located (198) km north east from Kurdistan regional capital (Erbil) and (385) km north from the federal Iraqi capital (Baghdad). It is located between (33/43- 20/46) longitudinal parallels, eastwards and 31/36-32/44 latitudinal parallels, westwards. Sulaimania is surrounded by the Azmar range, Goizja range and the Qaiwan range from the north east, Baranan mountain from the south and the Tasluje hills from the west. The area has a semi-arid climate with very hot and dry summers and very cold winters, **Barzanji, 2003** .The variables used in the model are the monthly air temperature, humidity, precipitation and evaporation .These variables that are expected to be useful for catchment management and runoff calculation. Data were taken from three meteorological stations (sites) inside and around Sulaimania city, which are Sulimania, Chwarta and Penjwin. These stations are part of the metrological stations network of Sulaimania governorate north Iraq. This network has eight weather stations distributed over an approximate area of (17023 km^2). **Table 1**, shows the names, latitudes, longitudes and elevations of these stations. **Fig. 2**, shows a Google map of the locations of these stations. **Table 2**, shows the approximate distances between these stations and all of the metrological stations in Sulaimania governorate.

The model was applied to the data of the case study described above. The available length of the records for the four variables and the three stations is (8) years of monthly values, (2004-2011). The data for the first (5) years, (2004-2008) were used for the estimation and the mutation of the model parameters matrices **ϕ**1,2, and σ, while the left last 3 years data, (2009-2011) were used for verification. The data includes the precipitation as a variable which has zero values for June, July, August and September, in the selected area of the case study. These months are included in the analysis, by adding a constant value to the precipitation series of 0.1 to avoid the problems that may be created by these zeros.

In all similar analysis and before applying the forecasting model shown in eq. (1), a prior analysis should be made for each variable at each site to estimate it's dependent stochastic component .These steps were done for each variable at each site of the case study by ,**Al-Suhili, and khanbilvardi, 2014.** These steps are test of homogeneity using method proposed by ,**Yevjevich,1972.** trend test and normalization transformation. The results indicate that most of the variables in all sites are homogeneous and non-homogeneity is only exist in Sulaimania air temperature, Penjwin humidity, Penjwin air temperature, and Penjwin evaporation series. These non homogeneous series were homogenized using the method proposed by Yevjevich(1972). Trend analysis indicates that all of the data variables in all of the sites are free from trend. The well known Box-Cox transformation Box and ,**Jenkins, 1976,** was used for the purpose of normalization of data and was found successful.

The estimation of the stochastic dependent component of the series, was done using eq.(15), as follows:

$$\epsilon_{i,j}=\frac{XN_{i,j}-Xb_j}{Sd_j} \qquad (15)$$

Where:
$\epsilon_{i,j}$: is the obtained dependent stochastic component for year i, month j.
Xb_j : is the monthly mean of month j of the normalized series XN.
Sd_j : is the monthly standard deviation of month j of the normalized series XN.

For more details of these analysis one can refer to **Al-Suhili and Khanbilvardi,2014**. The next step in the modeling process is to estimate the parameters of the model. The $\epsilon_{i,j}$ obtained series are used to estimate the Lag-1 and lag-2 serial and cross correlation coefficients and then estimate $\phi k_{i,j}$, k=1,and 2, and $\sigma_{i,j}$ of matrix Eqs. (7) ,(8)and (9) respectively, but with each matrix size of 12*12, using the developed Eqs.(10), (11)and (12),but with each matrix size 12*12, respectively. This step is definitely different than this used by Al-Suhili and Khanbilvardi(2014), since the model developed herein is different. Moreover these parameters are then muted using the genetic algorithm model developed above.The expected results from this development is a better performance model since the development includes the use of two time steps correlations rather than only one time step used by the previous model. The estimated and muted parameters of the model are shown in **Tables 3,4 and 5.**

5.FORECASTING RESULTS AND DISCUSSION

The developed model mentioned above was used for data forecasting, recalling that the estimated parameters above are obtained using the 5 years data series (2004-2008). The forecasted data are for the next 3- years (2009-2011), that could be compared with the observed series available for these years, for the purpose of model validation. The forecasting process was conducted using the following steps which are the typical steps for forecasting:

1. Generation of an independent stochastic component (ξ) using normally distributed generator, for 3 years, i.e., (3*12) values.
2. Calculating the dependent stochastic component ($\epsilon_{i,j}$) using equation (2),with v=4,s=3 and the matrices of $\phi k_{i,j}$, k=1 and 2, and $\sigma_{i,j}$.
3. Reversing the standardization process by using the same monthly means and monthly standard deviations which were used for each variable using Eq. (15) after rearranging.
4. Applying the inverse power normalization transformation (Box and Cox) for calculating un-normalized variables using normalization parameters for each variable.

For forecasting models, accuracy of results is considered as the overriding criterion for selecting a model. The word “accuracy” refers to the “goodness of fit,” which in turn refers to how well the forecasting model is able to reproduce the data that are already known. The model validation is done by using the following typical steps:

1. Checking if the developed monthly model resembles the general overall statistical characteristics of the observed series.
2. Checking if the developed monthly model resembles monthly means using the t-test.
3. Checking the performance of the model of the hole forecasted series using Akaike test.

For the purpose of comparison of the forecasting performance between the new multi-variables multi-sites model developed herein and the other models the Akaike test can be used. This performance comparison was made to investigate whether the new model can produce better forecasted data series. For this purpose the Akaike (AIC), given by the equation (14), without minimization for the six models and with minimization for the present developed model.

For each site and variable three sets of data are generated, using the seven different models mentioned above. The overall statistical characteristics are compared with those observed, for each of the generated series. It is observed that the seven models can all give good resemblances for these general statistical properties. For all variables and sites the generated sets resemble the statistical characteristics not exactly with the same values of the observed series but sometimes larger or smaller but within an acceptable range. No distinguishable performance of any of the model can be identified in this comparison of the general statistical properties. **Tables 6,7. and 8**. show the t-test percent of succeed comparison summary for all of the variables and sites, for the three generated series. As it is obvious from the results of these tables, the generated series for the first six model succeed in (t-test) with high percentages except for the Penjwin station where sometimes low percentage is observed. It is also clear that the developed model had increased the percent of succeed. The developed model had the highest overall percent of succeed among the other models (100%). However the differences are small.

For purpose of the comparison between the developed model performance and that of the available forecasting models and the developed model for the data as mentioned above, the Akaike(1974) test was used. **Table 9**, shows the Akaike test results for all of the forecasted variables, in each site, obtained using the six models and those obtained by the developed model. It is obvious that the developed model had produced for most of the cases the lowest test value, i.e., the better performance. These cases represent (91.67%). However for these cases where the lowest AIC value is given by a model other than the developed model, the developed model had gave the next lowest AIC values. Moreover for these cases it is observed that very small differences are exist between these test values of the new model and the minimum obtained one.

6.CONCLUSIONS

From the analysis done in this research, the following conclusion could be deduced:
The model parameters estimation and mutation processes are simple and the sum of each row of the **ϕ**1, 2, and σ matrices is equal to 1, which reflects the weighted sum of the variables.The model can preserve the monthly means of the observed series with excellent accuracy, evaluated using the t-test with overall success (100%). However, the differences between the percent success is not so high between the developed model and the other models.

The comparison of the model performance with the other models performances using the Akaike test had proved that the developed model had a better performance for the most cases (91.67%). Moreover for those remaining cases where other model had the better performance (minimum AIC value); the test value of the developed model is slightly higher than this minimum value.

REFERENCES

- Al-Suhili, R. H. and Mustafa, N.F, 2003, *A Multi- variables Multi-sites Model for Hydrological Series Data Forecasting,* accepted for publication at the Journal of Eng. College of Engineering, University of Baghdad.

- Al-Suhili R.H., Al-Kazwini, M. J., and Arselan, C. A, 2010. *Multivariate Multisite Model MV.MS. Reg. for Water Demand Forecasting,* Eng. and Tech. Journal Vol. 28, No. 13, pp 2516-2529.

- Al-Suhili R.H., and Khanbilvardi R., 2014, *A Multi-Sites Hydrological Forecasting Model Using Relative Correlations,* American Journal of Engineering Research Vol.3, Issue 6, pp154-168.

- Akaike, H., 1974, *A New Look at the Statistical Model Identification,* IEEE T. Automat. Contr., 19 (6), pp716–723.

- Barzinji K. T., 2003, *Hydrogic Studies for Goizha Dabashan and Other Watersheds in Sulimani Governorate* , M.Sc. thesis submitted to the college of Agriculture, University of Sulaimania.

- Box, G.E., and Jenkins, G. M., 1976. *Time Series Analysis and Control,* San Francisco, California: Holden-Day, Inc.

- Khalili M, Leconte R. and Brissette F., 2007, *Stochastic Multisite Generation of Daily Precipitation Data Using Spatial Autocorrelation,* J. Hydrometeorology, Vol.8, pp 396-412.

- *Lee S. J. and Wents E. A., 2010. Space-Time Forecasting Using Soft Geo statistics: A Case Study in Forecasting Municipal Water Demand for Phonex, Arizona,* Journal of Stochastic Environ Risk Assess vol. 24: pp 283- 295.

- *Matalas N.C, 1967. Mathematical Assessment of Synthetic hydrology,* Journal of Water Resources Researches vol. 3: pp 937-945

- *Richardson C. W. and Wright D. A., 1984. WGEN: A Model for Generating Daily Weather Variables,* United States Department of Agriculture, Agriculture Research Service ARS-8.

- *Wilks D. S., 1999. Simultaneous Stochastic Simulation of Daily Precipitation, Temperature and Solar Radiation at Multiple Sites in Complex Terrain,* Journal of Elsevier, agricultural and forest meteorology 96:pp 85-101,.

- *Yevjevich, V. M., 1972***.** *The structure of Hydrologic Time Series,* Fort Collins, Colorado State University**.**

ABBREVIATIONS

SulAt: Air temperature at Sulaimania.
SulHu: Humidity at Sulaimania.
SulPr: Precipitation at Sulaimania.
SulEv: Evaporation at Sulaimania.
ChwAt: Air temperature at Chwarta.
ChwHu: Humidity at Chwarta.

ChwPr: Precipitation at Chwarta.
ChwEv: Evaporation at Chwarta.
PenAt: Air temperature at Penjwin.
PenHu: Humidity at Penjwin.
PenPr: Precipitation at Penjwin.
PenEv: Evaporation at Penjwin
SVSS: Single variable, single site model.
SVMS: Single variable, multi-sites model.
MVSS: Multi variables, single site model.

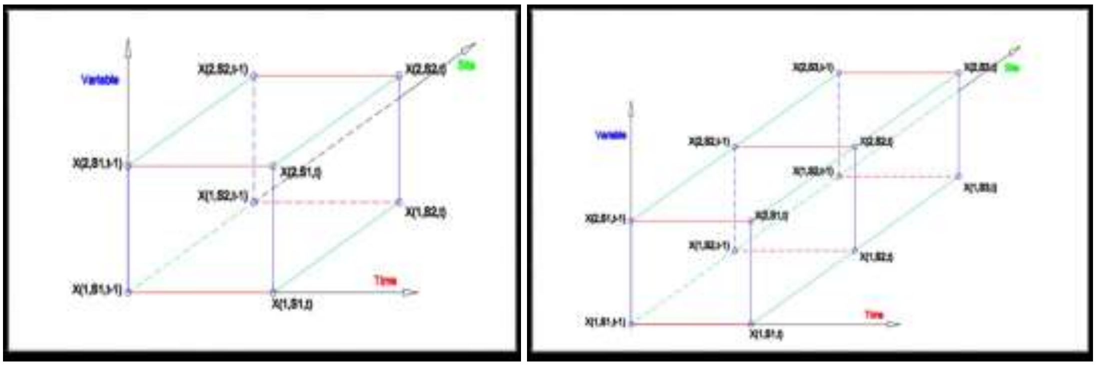

(a) **(b)**

Figure 1. Schematic representation of the developed multi-variables multi-sites model, a)MVMS(2,2,1), b) MVMS(2,3,1),**Al-Suhili and Khanbilvardi,2014**.

Table 1. North and east coordinates of the metrological stations selected for analysis.

Metrological station	N	E
Sulaimania	35° 33′ 18″	45° 27′ 06″
Dokan	35° 57’ 15”	44° 57′ 10″
Derbenikhan	35° 06′ 46″	45° 42′ 23″

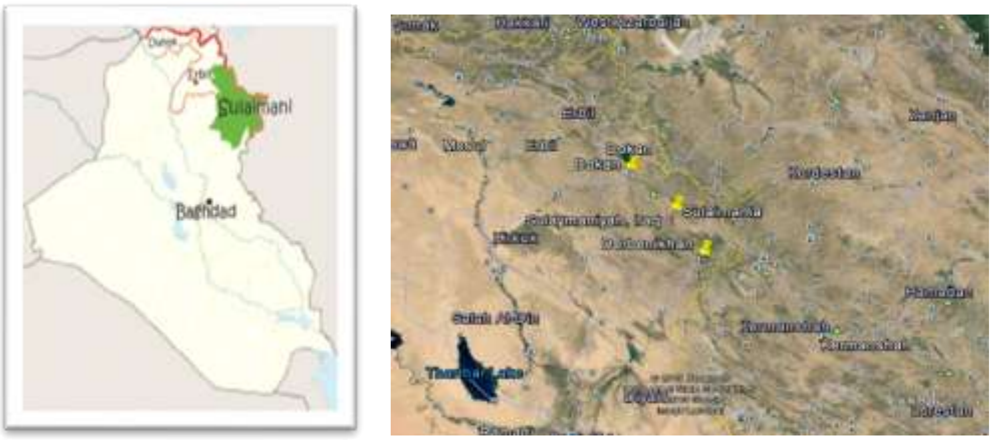

Figure 2. Locations of the metrological stations selected for analysis.

Table 2. Approximate distances between the Sulaimania weather stations network (km.), **Barzingi, 2003.**

Name of Weather Station	Sulaimani	Dukan	Darbandikhan	Penjwin	Chwarta	Halabjah	Bazian	Chamchamal
Sulaimani	0	62.76	54.00	45.88	20.85	63.36	29.17	56.10
Dukan	62.76	0	114.73	97.10	61.20	125.85	42.00	47.90
Darbandikhan	54.00	114.73	0	61.40	68.68	28.36	73.98	90.57
Penjwin	45.88	97.10	61.40	0	36.53	48.22	74.15	102.12
Chwarta	20.85	61.20	68.68	36.53	0	69.73	41.30	69.90
Halabjah	63.36	125.85	28.36	48.22	69.73	0	89.50	111.05
Bazian	29.17	42.00	73.98	74.15	41.30	89.50	0	28.41
Chamchamal	56.10	47.90	90.57	102.12	69.90	111.05	28.41	0

Table 3. Model Coefficients Matrix **ϕ**1.

	SulAt	SulHu	SulPr	SulEv	ChwAt	ChwHu	ChwPr	ChwEv	PenAT	PenHu	PenPr	PenEV
SulAT	9E-05	0.00083	0.001216	-0.00089	0.001039	0.003111	0.00092	0.00302	0.0004902	0.00264	0.00306	0.00334
SulHu	-0.002	-7E-05	0.00179	0.001458	0.0009656	0.001133	0.00162	0.00496	0.0033658	0.00154	0.00154	0.00349
SulPr	-7E-04	-0.0005	4.68E-05	0.004946	-0.000473	-0.00016	0.00014	0.00396	-0.000569	0.00029	-0.0005	0.00166
SulEv	-5E-04	-0.0004	0.005277	-3.8E-06	0.0002179	0.002646	0.00466	0.00075	-3.75E-06	0.00187	0.00471	0.00024
ChwAT	0.0009	0.00258	0.001425	-2.3E-05	-8.26E-05	0.006609	0.00122	0.00363	0.0007436	0.00244	0.00387	0.0041
ChwHu	-5E-04	0.00087	0.001276	0.001938	0.0018334	0.000174	0.00074	0.00164	0.0040532	0.00201	0.00097	0.0069
ChwPr	-8E-04	-0.0007	0.00026	0.005164	-0.000885	-0.00038	1.1E-05	0.00429	-0.000984	0.00032	-0.0003	0.00085
ChwEv	0.0003	0.00237	0.002408	-0.00049	0.0010564	0.001358	0.0025	-0.00077	-0.002271	0.0058	0.00344	0.00269
PenAT	0.0015	0.00069	0.000239	0.000859	0.0022123	0.003494	3.6E-05	0.00097	0.0001551	-9E-05	0.00223	0.00031
PenHu	0.0006	0.00113	0.002238	-8.4E-05	0.0012027	0.000747	0.00159	0.00713	-0.000475	-0.0003	0.00182	0.01189
PenPr	-0.001	8E-05	0.000863	0.002284	-0.00036	-0.0001	0.00066	0.00315	-0.000664	0.00112	-9E-07	0.00138
PenEv	0.0035	0.00207	0.000333	-0.00015	0.0037207	0.00343	0.00039	0.00388	-0.00017	0.01135	0.002	0.00089

Table 4. Model Coefficients Matrix ϕ2.

	SulAt	SulHu	SulPr	SulEv	ChwAt	ChwHu	ChwPr	ChwEv	PenAT	PenHu	PenPr	PenEV
SulAT	0.0406	0.00348	-0.00121	0.014164	0.0326137	0.001676	-0.0008	0.01678	0.0185219	0.00054	-0.002	0.00431
SulHu	0.0027	0.04271	0.011687	0.005042	0.005783	0.024246	0.01223	0.00617	0.0033607	0.0054	0.01746	-0.0021
SulPr	-3E-05	0.01266	0.036896	0.004796	0.001517	0.013677	0.03391	0.00397	0.0005742	0.00959	0.02605	-0.0008
SulEv	0.0147	0.00584	0.005347	0.04445	0.012055	0.004235	0.00797	0.01529	0.0110532	0.00074	0.00392	0.00246
ChwAT	0.0302	0.00539	0.000757	0.010837	0.0406819	0.003852	0.00041	0.01726	0.0194488	0.00117	0.00087	0.00519
ChwHu	0.0031	0.02582	0.013814	0.004269	0.0066439	0.039592	0.01164	0.00467	0.0033397	0.0083	0.01733	-1E-04
ChwPr	-7E-04	0.01256	0.032747	0.006544	0.0007594	0.010903	0.03839	0.00448	-0.000249	0.00835	0.02783	-3E-05
ChwEv	0.0163	0.00665	0.004293	0.012837	0.0188531	0.004149	0.00504	0.04542	0.001972	0.00373	0.00526	0.01221
PenAT	0.0199	0.00542	0.000964	0.011641	0.0221966	0.004502	0.00089	0.00505	0.0455255	0.00065	0.00148	0.0022
PenHu	0.0024	0.00686	0.009741	0.001986	0.002636	0.010262	0.00924	0.00478	0.0003667	0.04882	0.01738	-0.0004
PenPr	0.0006	0.01691	0.023759	0.00423	0.003011	0.015529	0.02632	0.00541	0.0019096	0.0142	0.03727	0.00115
PenEv	0.0064	0.00135	0.001288	0.002988	0.0098815	0.004767	0.00086	0.01719	0.0025273	0.00219	0.00166	0.04873

Table 5. Model Coefficients Matrix σ.

	SulAt	SulHu	SulPr	SulEv	ChwAt	ChwHu	ChwPr	ChwEv	PenAT	PenHu	PenPr	PenEV
SulAT	0.1622	0.04904	0.039409	0.074906	0.1322718	0.044986	0.04027	0.08161	0.0870505	0.04273	0.03765	0.05055
SulHu	0.0467	0.17091	0.067669	0.051751	0.0534633	0.103785	0.06908	0.05358	0.0477855	0.05256	0.08332	0.03671
SulPr	0.0384	0.068	0.14765	0.047889	0.0416035	0.070726	0.13617	0.04636	0.0396642	0.06007	0.10822	0.03682
SulEv	0.0787	0.05682	0.054907	0.177799	0.0717521	0.053052	0.06104	0.08019	0.0692286	0.04579	0.05195	0.04943
ChwAT	0.1231	0.05148	0.041675	0.064794	0.1627617	0.046955	0.04099	0.08132	0.0884664	0.04243	0.04157	0.05071
ChwHu	0.0473	0.10868	0.073023	0.04967	0.0550543	0.158355	0.06737	0.05059	0.0472773	0.05893	0.08276	0.03944
ChwPr	0.0372	0.06779	0.131862	0.051848	0.0401359	0.0635	0.15355	0.0475	0.0381013	0.05711	0.1143	0.03853
ChwEv	0.08	0.05497	0.049646	0.070487	0.0871308	0.049449	0.05128	0.18249	0.0446837	0.04759	0.0516	0.06853
PenAT	0.0949	0.058	0.048481	0.072703	0.1012188	0.055655	0.04833	0.05715	0.1820766	0.04785	0.04942	0.05105
PenHu	0.0522	0.062	0.068644	0.051373	0.0527015	0.070048	0.06753	0.05605	0.0480483	0.19546	0.0883	0.04359
PenPr	0.0382	0.07864	0.099759	0.045894	0.0433918	0.07468	0.10837	0.04838	0.0410341	0.07089	0.14909	0.03942
PenEv	0.0648	0.05418	0.054126	0.057668	0.0727816	0.06122	0.05325	0.09105	0.0566975	0.05327	0.0548	0.19451

Table 6. Comparison between the percent of succeed in t-test for differences in monthly means of the generated and observed data for set 1 generated series, by each model.

	SVSS	SVMS	MVSS	**Matalas, 1967**	**Al-Suhili and Mustafa, 2013**	**Al-Suhili and Khanbilvardi, 2014**	The Developed Model
SulAT	100	91.667	100	91.66667	100	100	100
SulHu	100	100	100	91.66667	83.3333333	100	100
SulPr	83.33	100	100	100	91.6666667	91.667	100
SulEv	100	100	100	100	100	100	100
ChwAT	100	91.667	91.667	91.66667	91.6666667	91.667	100
ChwHu	100	100	91.667	91.66667	100	100	100
ChwPr	91.67	91.667	83.333	100	91.6666667	91.667	100
ChwEv	91.67	91.667	91.667	91.66667	91.6666667	91.667	100
PenAT	83.33	100	91.667	91.66667	100	91.667	100
PenHu	66.67	66.667	83.333	75	83.3333333	83.333	100
PenPr	100	91.667	91.667	91.66667	100	100	100
PenEv	66.67	83.333	100	91.66667	100	91.667	100
Overall	90.28	92.361	93.75	92.36111	94.4444444	94.444	100

Table 7. Comparison between the percent of succeed in t-test for differences in monthly means of the generated and observed data for set 2 generated series, by each model.

	SVSS	SVMS	MVSS	**Matalas, 1967**	**Al-Suhili and Mustafa, 2013**	**Al-Suhili and Khanbilvardi, 2014**	The Developed Model
SulAT	100	100	100	100	100	100	100
SulHu	91.67	91.667	100	100	91.6666667	91.667	100
SulPr	100	100	100	100	100	91.667	100
SulEv	100	100	100	100	100	100	100
ChwAT	83.33	100	91.667	75	91.7	91.7	100
ChwHu	100	91.667	91.67	100	100	100	100
ChwPr	91.67	91.667	91.667	91.66667	91.6666667	91.667	100
ChwEv	91.67	91.667	91.667	83.33333	91.6666667	91.667	100
PenAT	100	100	100	91.66667	100	91.667	100
PenHu	66.67	66.667	75	91.66667	75	83.3	100
PenPr	100	100	100	91.66667	91.6666667	100	100
PenEv	100	91.667	91.667	91.66667	100	100	100
Overall	93.75	93.75	94.445	93.05556	94.4472222	94.444	100

Table 8. Comparison between the percent of succeed in t-test for differences in monthly means of the generated and observed data for set 3 generated series, by each model.

	SVSS	SVMS	MVSS	**Matalas, 1967**	**Al-Suhili and Mustafa, 2013**	**Al-Suhili and Khanbilvardi, 2014**	The Developed Model
SulAT	83.33	91.667	100	100	100	100	100
SulHu	100	91.667	83.333	100	83.3333333	91.667	100
SulPr	100	100	91.667	100	91.6666667	100	100
SulEv	100	100	100	100	100	100	100
ChwAT	100	100	91.667	91.66667	91.6666667	100	100
ChwHu	91.67	100	100	91.66667	91.6666667	91.667	100
ChwPr	91.67	100	91.667	91.66667	100	100	100
ChwEv	100	83.333	91.667	91.66667	91.6666667	91.667	100
PenAT	91.67	100	91.667	100	100	91.667	100
PenHu	75	66.667	66.667	75	75	75	100
PenPr	91.67	91.667	91.667	91.66667	91.6666667	91.667	100
PenEv	100	100	83.333	83.33333	100	100	100
Overall	93.75	93.75	90.278	93.05556	93.0555556	94.444	100

Table 9. Comparison between the AIC test for the three generated series by each model.

	SulAT	SulHu	SulPr	SulEv	ChwAT	ChwHu	ChwPr	ChwEv	PenAT	PenHu	PenPr	PenEv
-SVSS	60.04	183	54.89	2.104	58.31	165.55	65.53	14.39	63.32	143.64	95.86	6.103
-SVMS	42.13	185	57.73	14.42	70.01	186.98	99.93	4.1	57.76	152.49	91.31	13.22
-MVSS	66.97	158	58.37	7.095	71.31	169.69	51.35	-1.246	60.95	157.9	130.7	-8.323
Matals, 1967	47.22	162	52.12	11.61	59.34	155.12	50.15	16.89	59.67	148.91	82.56	-10.56
Al-Suhili and Mustafa, 2013	45.02	158	39.68	-1.38	55.91	153.2	47.48	-13.86	53.88	143.23	62.2	-11.74
Al-Suhili and Khanbilvardi, 2014	36.43	144	36.58	-5.35	48.84	144.92	48.62	-15.76	46.57	126.39	61.89	-20.55
The Developed Model	26.34	136	**38.14**	-7.34	42.67	137.56	35.67	-19.87	39.67	111.14	55.67	-21.69
-SSSV	54.38	163	50.84	10.68	79.51	187.49	55.09	-19.04	61.29	153.73	91.79	19.75
-MSSV	73.38	168	72.78	13.97	62.9	173.26	63.21	6.373	67.8	173.56	101.3	15.52
-MVSS	48.31	190	62.51	6.358	81.06	169.01	66.25	-3.124	61.9	142.18	95.18	29.9
Matals, 1967	42.67	157.8	47.45	4.56	59.67	153.67	49.15	11.69	54.15	139.45	78.34	26.56
Al-Suhili and Mustafa, 2013	40.6	153	33.71	-3.7	53.7	148.72	46.15	-12.47	50.31	137.7	59.68	-19.29
Al-Suhili and Khanbilvardi, 2014	35.09	150	36.09	-3.21	51.71	146.4	46.3	-9.43	45.59	127.45	63.46	-14.18
The Developed Model	33.21	143.16	29.87	**-1.1**	45.67	122.56	36.89	-14.78	41.34	121.78	58.99	-22.45
SSSV	46.43	145	63.35	17.81	64.45	171.17	110.7	22.29	56.22	164.29	107.7	-5.484
MSSV	48.88	165	67.72	11.97	69.84	177.03	86.33	29.87	70.4	149.45	63.05	20.53
MVSS	48.96	167	45.03	25.9	81.77	160.22	87.54	-1.396	69.7	153.59	98.92	28.11
Matals, 1967	45.91	143	44.54	19.87	58.67	157.78	76.57	-10.12	56.12	143.56	81.23	22.13
Al-Suhili and Mustafa, 2013	43.53	150	42.85	-6.46	57.58	147.49	55.41	-16.01	55.76	132.87	67.45	-14.84
Al-Suhili and Khanbilvardi, 2014	41.61	144	35.67	-2.82	57.4	142.15	45.95	-11.54	51.3	117.14	62.19	-15.31
The Developed Model	33.54	121.5	32.67	**-4.32**	48.78	139.98	36.78	-18.92	46.78	113.56	58.75	-17.23

Scheduling of Irrigation and Leaching Requirements

Amer Hassan Al-haddad
Assistant Professor
College of Engineering, University of Baghdad
E-mail: Ameralhaddad 1950@yahoo.com

Alaa Ibraheem Badi Al-Safi
College of Engineering, University of Baghdad
E-mail: alaa86wr@yahoo.com

ABSTRACT

Iraq depends mainly on Tigris and Euphrates Rivers to provide high percentage of agricultural water use for thousands years. At last years, Iraq is suffering from shortage in water resources due to global climate changes and unfair water politics of the neighboring countries, which affected the future of agriculture plans for irrigation, added to that the lack of developed systems of water management in the irrigation projects and improper allocation of irrigation water, which reduces water use efficiency and lead to losing irrigation water and decreasing in agricultural yield. This study aims at studying the usability of irrigation and leaching scheduling within the irrigating projects and putting a complete annual or seasonal irrigation program as a solution for the scarcity of irrigation water, the increase of irrigation efficiency, lessening the salinity in the projects and preparing an integral irrigation calendar through field measurements of soil physical properties and chemical for project selected and compared to the results of the irrigation scheduling and leaching with what is proposed by the designers. The process is accomplished by using a computer program which was designed by Water Resources Department at the University of Baghdad, with some modification to generalize it and made it applicable to various climatic zone and different soil types. Study area represented by large project located at the Tigris River, and this project was (Al-Amara) irrigation project. Sufficient samples of project's soil were collected so as to identify soil physical and chemical properties and the salinity of soil and water as well as identifying the agrarian cycles virtually applied to this project. Finally, a comparison was conducted between the calculated water quantities and the suggested ones by the designers. The research results showed that using this kind of scheduling (previously prepared irrigation and leaching scheduling) with its properties which made it applicable requires an intense care when using the plant distribution pattern, the agrarian cycle, its agrarian areas and agricultural intensity within all climatic regions. Also, it was found that this program was an instrumental tool for providing water if the plant distribution pattern was well-selected.

Keywords: irrigation scheduling, leaching scheduling, percentage of maximum root depth, salinity, water resources dept. program, water budget, Amara irrigation project.

متطلبات جدولة الري والغسيل

د. عامر حسن حداد
كلية الهندسة / جامعة بغداد

علاء ابراهيم بادي
كلية الهندسة /جامعة بغداد

الخلاصة

يعتمد العراق على نهري دجلة والفرات في توفير نسبة كبيره من الاحتياجات المائية للإغراض الزراعية منذ آلاف السنين . إلا انه في السنوات الأخيرة أصبح يعاني من شحه في موارده المائية بسبب التغيرات المناخية العالمية والسياسات المائية الجائرة لدول الجوار مما اثر على الخطط الزراعية المستقبلية . أضافه إلى ذلك ضعف طرق إدارة المياه في المشاريع الاروائيه وتوزيع مياه الري بصورة غير فعاله مما قلل من كفاءة استخدام المياه والذي أدى إلى هدر في مياه الري ونقص في الإنتاج . تهدف هذه الدراسة إلى دراسة إمكانية استخدام جدولة الري والغسيل ضمن المشاريع الاروائيه ووضع برنامج إروائي سنوي أو موسمي متكامل كحل

لشحه مياه الري وزيادة كفاءة الري وتقليل الملوحة في المشاريع وإعداد تقويم إروائي متكامل وذلك من خلال قياسات حقلية لخواص التربة الفيزيائية والكيمائية للمشاريع المختارة ومقارنه نتائج جدولة الري والغسيل مع ما هو مقترح من المصممين. تتم هذه العملية باستخدام برنامج حاسوبي تم انشاؤة وإعداده وتتطويرة في قسم هندسة الموارد المائية في جامعه بغداد مع بعض التعديلات للارتقاء به نحو العمومية وجعله قابل للتطبيق في المناطق المناخية المختلفة ولأنواع مختلفة من الترب. تم اختيار مشروع ري العمارة كمنطقة للدراسة وتم جمع العينات الوافية للمشروع لمعرفة خواصه الفيزيائية والكيميائية ونسبة الملوحة في التربة ومياه الري أضافه إلى ذلك تم معرفة الدورة الزراعية المطبقة فعليا في المشاريع. وأخيرا تم إجراء مقارنة بين كميات المياه المحسوبة وكميات المياه المقترحة من قبل المصممين ومن خلال نتائج البحث أظهرت إن استخدام هكذا نوع من الجدولة (جدولة الري والغسيل المعدة مسبقا) بخصائصه تجعله قابل للتطبيق, والذي يتطلب عناية شديدة عند استخدام نمط توزيع النباتات والدورة الزراعية والكثافة الزراعية, كما وجد إن هذا البرنامج أداة مفيدة لتوفير المياه إذا ما أحسن اختيار النباتات ونمط توزيعها.

الكلمات الرئيسية : ألجدوله الاروائيه , جدوله الغسيل , النسبة المئوية لأطول جذر , الملوحة , البرنامج الخاص بقسم الموارد المائية , الموازنة المائية , مشروع ري العمارة.

1. INTRODUCTION

1.1 Irrigation Scheduling

Irrigation scheduling simply determines when to irrigate and how much irrigation water to apply, or it is a strategy that minimizes the supplied water with minimal impacts on yields and crop quality. An effective irrigation schedule helps to maximize profit while minimizing environmental problems, water, and energy use.

The following factors that contribute in developing a workable and efficient irrigation schedule:

- Soil properties;
- Soil-water relationships;
- Type of crop and its sensitivity to drought stress;
- Stage of crop development;
- Availability of water supply; and
- Climatic factors such as rainfall and temperature.

A range of irrigation scheduling methods have been developed to assist farmers and irrigators to apply water more efficiently taking into account crop evaporation and rainfall. Irrigation scheduling includes the following methods:

First - Traditional method which is unfortunately the method adopted by many farmers. This method is based on individuals' decision and depends on previous observations without taking into account the need of plant to water. There is a belief among many farmers that the addition of large amounts of irrigation water increases the agricultural productivity. This method consumes a large amount of water without a scientific justification, and it may cause:

1. Lack of soil aeration and accumulation of CO_2 that inhibits the ability of roots to absorb water and nutrients.
2. Leaching nutrients from the soil and removing it from the root zone.
3. Depletion of water without justification, causing a crisis in water resources.
4. Lack of productivity.

Therefore, this method must be disposed of.

Second - Modern methods which are methods based on scientific base to take into account several factors affecting water consumption, and these methods depend on climatic factors, soil factors, plant type, or depend on all these factors.

Making the very best decisions about when and where to irrigate is not easy when the irrigation water available over a season is production limiting. Each decision requires a consideration of the entire remaining irrigation season. A farmer needs to make difficult decisions about when and which crops will be subjected to water stress. Uncertain rainfall further complicates decisions. Optimal on-farm irrigation scheduling methods can provide advice in these situations. Existing optimal on-farm irrigation schedulers generally use dynamic programming for optimization. A number of authors since the late 1960s have proposed using simplistic plant models combined with dynamic programming optimization to schedule irrigation for a single crop. Made significant contributions to these single crop schedulers.

,Hamad ,1996. developed a practical and easy procedure for preparing seasonal or annual irrigation programs for an irrigation project. The developed procedure is based on some practical criteria among them are the:

- Supplied discharge would be constant in all irrigations;
- Time of application would be also constant throughout the season;
- Starting day of all irrigations in the season or the year would be the same day in the week in order to make the farmers and irrigators accustomed to the days of irrigation; and
- Irrigation intervals are selected in such a way to avoid crop stress due to insufficient soil moisture.

,Al-Hadaad, 1997, developed a model to pre-schedule irrigations in large irrigation projects based upon average weighted of root depth, physical soil properties and crop water requirements. This model also includes estimating expected annual crop production of the project for a given cropping pattern.

,Riffat, 1999, developed an optimization process to maximize total crop production from a given cropping pattern in an irrigation project by using pre-scheduled irrigations and pre-specified constraints on the volumes of applied water and cropping intensity.

,Al-Hadaad ,2001, evaluated the effect of using weighted average root depths and a certain level of depletion in building an irrigation scheduling program for large projects containing different crops on water stress of wheat crop during the growing season.

,Broner ,2005, pointed out that the irrigation scheduling offers several advantages such as:

1. It enables the farmer to schedule water rotation among the various fields to minimize crop water stress and maximize yields,
2. It reduces the farmer’s cost of water and labor through less irrigation, thereby making maximum use of soil moisture storage,
3. It lowers fertilizer costs by holding surface runoff and deep percolation (leaching) to a minimum,
4. It increases net returns by increasing crop yields and crop quality,
5. It minimizes water-logging problems and reducing the drainage requirements,
6. It assists in controlling root zone salinity problems through controlled leaching, and
7. It results in additional returns by using the saved water to irrigate non-cash crops that otherwise would not be irrigated during water-short periods.

,Bakr, 2011, pointed to effectively schedule irrigation applications, four key pieces of information need to be known:

- soil texture;
- water holding capacity of the soil;
- Initial soil moisture content; and
- crop water use at the specific development stage.

The use of computer programs to help scheduling irrigation was introduced in the 1970’s. However, only recently with the introduction of fast, personal computers have they begun to gain wider acceptance, **Martin, 2009**. Irrigation scheduling is based on three methods and tools; they are plant stress measurement, predictive models, and soil moisture measurement ,**Antosch, 2007**. Soil water measurement based on either "soil water measurement", where the soil water status is measured directly or determine the need of irrigation, or on "soil water balance calculations" where the soil water statue is estimated by calculation using a water balance approach in which the change in soil water over a period is given by the difference between the inputs and the losses.

The scheduling procedure adopted in this research is that developed by ,**Hamad ,1996.** and **, Al-Haddad, 1997.** It is a practical and applicable procedure that can be adopted in large irrigation projects since it is simple to use and easy to understand by project manager and farmers. It was based on the following constrains:

1. Applied discharge at the project head gate is constant throughout the whole year, such application would facilitate the operation of controlling and distribution structures of irrigation network.
2. Irrigation time is held constant during the year or at least during the growing season, in order to habituate the worker and farmer on irrigation time in the project.
3. Irrigation time must be chosen in a way that facilitates water distribution and project operation and should be full-days and avoiding parts of the day.
4. Irrigation interval must be selected in a way that crops will not be stressed due to decreasing soil moisture content and will not cause over-irrigation.
5. The day of starting irrigation during the year is same day of the week and the day of starting of irrigation scheduling. Such a practice would habituate the farmer to irrigation date, and the date of water distribution between farmers.

These constrains can be useful for a single large project. Since this program is intended to a number of projects located the Tigris River basin which is different in soil properties, climate, and types of planted crops; such variation should be taken in account when building a scheduling program. Some modifications on these constrains are required to make it more comprehensive, so the third and fifth constrains are modified as follows:

- For heavy soils, the day of starting irrigation during the year is the same day of the week as the day of starting the irrigation schedule or irrigation year. For light soils, there are two possible irrigation days in the week, first day has the same interiority of heavy soils irrigation day and the second is in the middle of week of the day of starting irrigation year.
- In winter season, time of irrigation will be chosen in a way that does not affect crop growth, while in summer season there is a continuous irrigation except in rainy zones.

1.2 Leaching Scheduling

Leaching scheduling means how much water should be applied to leach soil salinity and when. Leaching is often done to reclaim saline soil or to conserve a favorable salt content of the soil of irrigated lands as all irrigation water contains salts.

The Leaching Requirement concept was developed by the U.S. Salinity Laboratory **,Richards, 1954.** It has been defined as "the fraction of the irrigation water that must be leached out of the bottom of the root zone in order to prevent average soil salinity from rising above some specifiable limit"; therefore, it is the minimum amount of water that must pass through the root zone to keep salts within an acceptable range.

The leaching requirement depends on the salt concentration of the irrigation water, the amount of water extracted from the soil by the crop (evapotranspiration) and the salt tolerance of the crop, which determines the maximum allowable concentration of the soil solution in the root zone , ,**Rhoades, 1974. and ,U.S. Salinity Laboratory Staff, 1954.**

The accumulated salt in the root zone is generally leached by applying water in excess of field capacity (LR). Field capacity can be defined as a maximum amount of moisture that can be held against gravity in the soil pores of the root zone Results from several laboratory experiments by **Miller et al.,1965;** some field trials by**, Nielsen et al.,1966. and Oster et al.,1972**, had shown that the quantity of salts are removed per unit quantity of water leached can be increased appreciably by leaching at soil moisture contents of less than saturation, i.e. under unsaturated conditions. In the field, unsaturated conditions during leaching were obtained by adopting intermittent pounding or by intermittent sprinkling at rates less than the infiltration rate of the soil. The degree of salt removal during leaching can be markedly influenced by the method used.

,Hussein ,2012, pointed that leaching is the key factor in controlling soluble salts brought in by the irrigation water and can be divided into two parts:

1. Fundamental (Initial) Leaching

To reclaim saline soils, leaching strategies especially continuous pounding and intermittent pounding were developed by Laboratory scientists and are universally used ,**Reeve et al., 1955**.

Hoffman, 1980, used the data obtained from the field in USA and some countries and represented in the equation below:

$$\frac{EC_{fc} - EC_e}{EC_{iw} - EC_e} = \left(\frac{0.07}{\left(\frac{D_{iw}}{D_s} \right)} \right) + 0.02 \qquad (1)$$

Where:

EC_e : Electrical conductivity of soil , ds/m,

EC_{fc}: Electrical conductivity of soil extract at field capacity, ds/m,

EC_{iw}: Electrical conductivity of irrigation water, ds/m,

D_{iw}: Depth of irrigation water, mm, and

D_s: Soil depth, mm.

Leaching curves both with respect to desalinization and of a highly saline-sodic soil, were determined experimentally using large size ring (infiltration meters). These curves were useful in knowing the amount of water of a given composition needed to reduce the harmful levels of salinity and sodicity to the lower desirable values. Different theoretical models were also tested by comparing the calculated and experimental desalinization leaching curves. It was found that there is a reasonably good agreement between theoretical and experimental results up to nearly 10% of the initial salinity.

2. Maintenance (Secondary) Leaching or Leaching Requirement

The actual LR can only be determined by monitoring salinity control which is then related to field water management. Under some conditions however, differences in soils, drainage and water application methods make leaching less than I00% efficient. Cracks, root holes, wormholes and other large pores can transport water quickly through the root zone when these channels are in contact with the irrigation water at or near the surface **,Rhoades, and Merrill, 1976,** and **,Rhoades, 1990.** suggested the following equation:

$$LR = \frac{EC_{iw}}{(5 * EC_e - EC_{iw})} \qquad (2)$$

Where:

LR: Leaching Requirement, expressed as percentage.

,Hussein ,2012, pointed that the success of irrigated agriculture, in the long run, depends on maintaining the balance of salt in the root zone of crops, where whenever the salt dissolves in irrigation water added to the soil, it increases its focus as a result of evaporation-transpiration. Thus, the salt concentration becomes higher than the estimated carrying plants to it, and to maintain the crop damage must remove these excess salts by leaching zone using irrigation water, and at the expense of high irrigation water to be added by the specific scheduling program, we should take into account the salt budget for this case. The additional irrigation water used to wash the soil will also wash the nutrients in the soil.

In practice, the U.S. Salinity Laboratory recommends to use the average electrical conductivity of the saturation soil solution extract EC_e;(if the electrical conductivity of drainage water not readily available), and the EC_{iw} to determine LR, and also recommends that the salt entering into the root zone from irrigation or capillary rise from ground water remains in the root zone.

If drainage is adequate, the depth of water required for leaching depends on the salt sensitivity of the crop and the salinity of the applied water. When salinity is high, the depth of leaching water needed may be too great, making it necessary to change to a more salt tolerant crop, providing that the market economics will allow this. In dealing with a major salinity problem related to water quality, a cropping change is considered a drastic step and will only be taken when less severe options have failed to maintain economic production. Leaching, on the other hand, is a basic step in production even for water of the best quality and must be practiced when necessary to avoid salt accumulation that could ultimately affect production. Leaching salt downward into the deeper layer with excess water is the most common method to lower soil salt content in the root zone **,Qadir et al., 2003.**

2. MATHEMATICAL MODEL

2.1 Irrigation Scheduling

Conceptual formulation

Irrigation scheduling means how much water should be applied and when to irrigate. To make the right decision, there are some steps that should be followed. First of all, indicate cropping pattern and information about each crop should be known, such as growing season, growing and harvesting date, root depth. Soil physical properties, climate, availability of water resources, and field water losses also should be known.

With the aid of the information above, monthly and annual water requirements can be calculated and irrigation scheduling can be adopted. Three main schedules are known, these are: constant depth; constant interval; and practical irrigation schedule. As it is known, scheduling of irrigation affects the quantity of irrigation water which is received by plants. Since each crop has its own root zone and consumptive use rate, **Al-Mesh'hedany ,2002.** investigated the effect of an irrigation scheduling scheme on each crop grown in the project by executing a water budgeting procedure for each crop on a daily basis in order to determine the actual amounts of water received from the adopted irrigation scheduling scheme for each crop during its growing season. In this research, this procedure will be adopted to investigate planted crop statue due to irrigation scheduling procedure.

The procedure described in the previous section was mathematically formulated to obtain a workable procedure .Below, a brief description of the mathematical formulation of irrigation scheduling procedure items that must be provided, **Al-Haddad, 1997.**

Crop water requirements: The first step in irrigation scheduling is to determine crop water requirements. Actual monthly crop water requirements can be estimated from reference evapotranspiration and crop coefficient as follows:

$$ET_{cij} = K_{cij} * ET_{Oi} \tag{3}$$

where:

ET_{cij} : Actual monthly evapotranspiration rate of the j^{th} crop during the i^{th} month (mm/month),

K_{cij} : Monthly crop coefficient of the j^{th} crop during the i^{th} month (dimensionless),

ET_{Oi} : Monthly reference crop evapotranspiration rate (potential evapotranspiration rate) during the i^{th} month (mm/month),

i : Month index, and

j : Crop index.

Since a cropping pattern contains many crops, the weighted average of crop evapotranspiration rate ought to be used to estimate irrigation water requirements. The monthly weighted average of actual crop evapotranspiration for certain crop pattern can be calculated from:

$$\mathrm{WET_{ci}} = \frac{\sum_{j=1}^{n}(\mathrm{ET_{cij}} * \mathrm{NA_j})}{\sum_{j=1}^{n}\mathrm{NA_j}} \quad (4)$$

where:

$\mathrm{WET_{ci}}$: Monthly weighted average of actual crop evapotranspiration for certain cropping pattern during the i^{th} month (mm/month),

n : Number of planted crops in adopted crop pattern, and

$\mathrm{NA_j}$: Net area planted with the j^{th} crop, it is equal to $NA * PA_j$ (don.),

PA_j : Percentage of area planted with the j^{th} crop, and

NA : Net irrigated project area (don.).

Net monthly volume of irrigation water requirements can be calculated from subtracting average monthly effective rainfall (if there is) from monthly crop consumptive use rate and multiplying by the area as follows:

$$\mathrm{NI_{i\,req.}} = \sum_{j=1}^{n} \mathrm{C} * \mathrm{NA_j} * (\mathrm{WET_{ci}} - \mathrm{ER_i}) \quad (5)$$

where:

$\mathrm{NI_{i\,req.}}$: Net volume of water required during the i^{th} month (m^3),

$\mathrm{ER_i}$: Monthly effective rainfall during the i^{th} month (mm/month), and

C : Conversion factor units (dimensionless).

So, the net continuous irrigation discharge required during the i^{th} month would be:

$$NQ_{i\,req.} = C_1 \left(\frac{NI_{req,}}{ND_i}\right) \quad (6)$$

where:

NQ i req.: Net continuous discharge required during the i^{th} month (m^3/sec),and

$\mathrm{ND_i}$: Number of days in i^{th} month.

C_1 : conversion factor.

The gross continuous irrigation discharge required during the i^{th} month can be calculated by:

$$\mathrm{GQ\ i\ req.} = \frac{\mathrm{NQ_{i\,req}}}{\mathrm{IE_i}} \quad (7)$$

where:

GQ i req : Gross continuous discharge required during the i^{th} month (m^3/sec), and

IE : Expected irrigation efficiency in the project expressed as a percentage.

The water duty which represents the irrigation capacity of unit irrigation water to irrigate unit of area, and can be calculated from:

$$\mathrm{WD_i} = \frac{\mathrm{NQ_{i\,req}}}{\mathrm{NA_i}} \quad (8)$$

where:

WD_i : Water duty during the i^{th} month ($^{l/sec}/_{ha}$), and

NA_i : Net irrigated project area during the i^{th} month (don.)

One of the main and important parameters that affects irrigation scheduling is soil water content. First step to estimate soil water content is to know the root zone depth. Adopting maximum root depth means occurrence of water losses on areas planted with crops having shallow root zones, while adopting minimum root depth means water shortage and/or water stress on areas planted with crops having deep root depth zone. Thus, in this research a percentage of maximum root depth shall represent root zone depth for a certain cropping pattern**, Bakr ,2011**, and it can be calculated from:

$$URD_i = \max(RD_{ij}) * \% RD \tag{9}$$

where:
URD_i : Used root depth during the i^{th} month (mm),
RD_{ij} : Root depth of the j^{th} crop during the i^{th} month (mm), and
$\% RD$: Percentage of the root depth.

The total available water is calculated as:

$$TAW_i = (FC - PWP)\ URD_i \tag{10}$$

where:
TAW_i : Total available water (mm),
FC : Soil water content at field capacity expressed as a percentage by volume, and
PWP : Soil water content at permanent wilting point expressed as a percentage by volume.
The readily available water is expressed as a percentage of the total available water, or:

$$RAW_i = TAW_i * AD \tag{11}$$

where:
RAW_i : Readily available water in the root zone during the i^{th} month (mm), and
AD : Allowable depletion expressed as a percentage.

The allowable depletion differs from one crop to another and it is a function of evaporation power of the atmosphere. ,**Allen et al., 1998,** gave an allowable depletion for ETc =5 mm/day. Therefore, an adjustment is required for different evapotranspiration rates and they suggested an adjustment formula. In this research, the fraction of allowable depletion and adjustment formula for each crop presented by ,**Allen et al, 1998.**,will be adopted. The adjustment formula is:

$$AD_j = \text{app.(ii)} + 0.04 * (5 - ETc) \tag{12}$$

where:
AD_j : Allowable depletion of the j^{th} crop expressed as a percentage, and
app.(ii): Soil water depletion fraction for no stress for crops.
As allowable depletion is different from one crop to another as was mentioned above, the weighted average allowable depletion for an irrigation project will be adopted, and is calculated as follows:

$$AD = \frac{\sum_{j=1}^{n} AD_j * PA_j}{\sum_{j=1}^{n} PA_j} \tag{13}$$

Initial soil water deficit in the first day of irrigation scheduling is measured or assumed. Therefore, the soil water deficit at the second day of schedule can be calculated as:

$$SWDB_{ki} = SWDA_{(k-1)i} + WET_{cki} - ER_{ki} \quad (14)$$

where:

$SWDB_{ki}$: Soil water deficit on the k^{th} day before irrigation during the i^{th} month (mm),

$SWDA_{(k-1)i}$: Soil water deficit after irrigation on the $(k-1)^{st}$ day during the i^{th} month (mm),

ER_{ki} : Effective rainfall (mm),

and

k : Day index.

When a new month begins, root zone depth increases due to a plant growth if the soil water at the end of the previous month is greater than the soil water at the beginning of the new month, then the increase in root depth requires additional quantity of water to raise its water content. This additional quantity of water is calculated as follows:

$$SWDL_i = \frac{SWDAL_i}{URD_i} \quad (15)$$

where:

$SWDL_i$: Soil water deficit after irrigation (if there is any) at the last day in the i^{th} month measured as a percentage, and

$SWDAL_i$: Soil water deficit after irrigation (if there is any) at the last day in the i^{th} month expressed as a depth of water (mm).

The additional soil water required to raise the soil water content due to the additional root depth calculated as follows:

$$ASWD_{(i+1)} = (FC - ISWC + SWDL_i)ARD_{(i+1)} \quad (16)$$

where:

$ASWD_{(i+1)}$: Additional soil water deficit in the $(i+1)^{th}$ month (mm),

ISWC : Initial soil water content (mm), and

$ARD_{(i+1)}$: Additional used root depth and is equal as $URD_{(i+1)} - URD_i$ (mm).

This additional water is added to the soil water deficit on the first day of the $(i+1)^{th}$ month and it is equal to zero when root depth at i^{th} month is equal or greater than root depth at $(i+1)^{th}$ month or when the soil water content at the last day of the month is less than the initial soil water.

The daily soil water deficit after irrigation during the i^{th} month can be calculated from:

$$SWDA_{ki} = SWDB_{ki} - Irr.D_{ki} \quad (17)$$

where:

$Irr.D_{ki}$: Applied net irrigation depth infiltrated in the soil on the k^{th} day during the i^{th} month (mm).

Irrigation water must be applied whenever soil water content reaches a pre-specified value expressed as a percentage of RAW_i or difference between ($SWDB_i$ and RAW_i) . To avoid crop water stress, irrigations should be applied before or on the day when the used readily available water is depleted (i.e., $SWDA_{ki} \leq RAW_i$).

The applied net irrigation depth can be calculated from:

$$Irr.D_{ki} = \frac{IRR_{time\ i} * Q_{max} * IE}{NA_i} \quad (18)$$

where:

$IRR_{time\ i}$: Irrigation time (days), and

Q_{max} : Gross maximum or design project discharge (m^3/sec).

2.2 Leaching Scheduling

The conceptual facts were mathematically formulated in order to obtain a workable procedure. Below, is a brief description of the mathematical formulation of leaching scheduling procedure items as presented .The basis for understanding the impact of irrigation and drainage management on the salt balance is the water balance of the root zone. The water balance of the root zone can be described in the following equation **,FAO, 1985.**

$$Irr.D = R^* + ET_c \tag{19}$$

where:

R* : Depth of leaching water, mm.

Salt balance equation the root zone

With each irrigation, salts are added to the root zone because certainly there is a salt in water . A fraction of the salts is leached below the root zone by the net deep percolation water. After a certain period, salt accumulation in the soil will approach an equilibrium or steady-state concentration based on the salinity of the applied water and leaching water **,FAO, 1985.**

The following assumptions are made to put the salt balance equation:

- The exchange processes and chemical reactions which take place in the soil are not taken into consideration, and
- The amount of salts supplied by rainfall, fertilizers and exported by crops is negligible. The zone of shallow groundwater is created with the same average salinity concentration as the percolation water.

Under these assumptions, the salinity of the soil water is equivalent to the salinity of the water percolating below the root zone. The water balance of the root zone can be described in the following equation**:**

$$Irr\,.D \, * \, C_{iw} = R^* * C_R{}^* \tag{20}$$

Where:

C_{iw}: The average salt concentration of irrigation water, ppm, and

$C_R{}^*$: The average salt concentration of depth leaching water, ppm.

Leaching efficiency coefficient

Leaching efficiency coefficient is an essential parameter to be considered in the leaching processes. It indicates the degree of mixing between the applied water and the original soil solution, where it could be defined in one of two ways:

- With respect to the water percolating from the bottom of the root zone. It can be defined as the percentage of water percolating from the original soil water, the remainder of which flows through a bypass consisting of a crack or a root hole. This concept of leaching efficiency for vertical water movement was originally during the experimentation works carried out in the Dujailah Project in Iraq by ,**Boumans, 1963,** and
- With respect to the irrigation water, the leaching efficiency is defined as the percentage of irrigation water mixing with soil water.

The introduction of a leaching efficiency coefficient means that the full amount of water percolated through the soil profile is replaced by the efficient or effective amount of water during the leaching process.

In a related work by ,**Van Der Molen, 1979,** two different expressions were formed, each describing a different model of physical leaching process. These two expressions take the following forms:

$$f = \frac{C_{Dp}}{C_e} \qquad (21)$$

$$f = \frac{C_{Dp} - C_{iw}}{C_{fc} - C_{iw}} \qquad (22)$$

Where:

C_{DP}: The average salt concentration of the water percolation below the root zone,
C_e: The average salt concentration of the reservoir solution (after leaching),
C_{fc}: The average salt concentration of the soil solution at field capacity, and
f : Leaching efficiency coefficient.(fraction of unity).

<u>The salt equilibrium equation:</u>

To calculate the leaching requirement amount, the salt equilibrium equation presented by ,**Richards, 1954.** is used in this study; this equation was obtained from:

- Salt balance equation, Eq. (20), and
- Leaching efficiency coefficient equation, Eq. (21).

The salt equilibrium equation therefore is:

$$R^* = (ET_c - ER)\left(\frac{EC_{iw}}{f\left(EC_{fc} - EC_{iw}\right)}\right) \qquad (23)$$

EC_{fc} calculated by the following relationship:

$$EC_{fc} = \mathrm{EC_0}\left(\frac{\theta_{vs}}{\theta_{fc}}\right) \qquad (24)$$

where:

EC_o: The initial electrical conductivity of soil solution at field capacity, ds/m,
θ_{fc}: Soil moisture content of soil at field capacity, fraction of unity, and
θ_{vs} : Soil moisture content of soil at saturation, fraction of unity.

$\frac{\theta_{vs}}{\theta_{fc}} = 2$: For moderate texture soil as showed by, **Al-Furat Center For Studies and Designs of Irrigation Project, 1992.**

To start the leaching scheduling, using the maximum planted crop root depth to guarantee that all necessary depths of others root zone will be leached during whole year. The amount of salts could be added during the first irrigation in any month equal to the amount of salts would be added in the second irrigation for the same month because the depth of irrigation dose is constant considered to be, but the depth of leaching water differ from month to another due to root`s growth and. The amount of salt would be added by any irrigation is:

$$Z_{ki} = (EC_{iw})_{ki} * NA_j * RD_j * C_o \qquad (25)$$

Where:

Z_{ki}: The amount of salts to be added on the k^{th} day after irrigation, during the i^{th} month, gram,
NA_j: Net area planted with j^{th} crop, don.,
RD_j: Root depth at any time of the j^{th} crop, mm, and
C_o: The conversion factor milli equivalent per liter (meq/l) or part per million (ppm), and the unit of electrical conductivity is dicesemen's per meter.

Through, 640 ppm=1 dS/m, **Ayers and Westcot, 1985.**

There are three probabilities of supplying irrigation water due to the status of soil moisture content, and these are;

- First probability is the net depth of irrigation water was equal to the soil water deficit before irrigation (full irrigation). Accordingly the soil water content after irrigation will reach the field capacity of soil, then:

$$Irr.D_{ki} = SWDB_{ki}$$

- Second probability is the net depth of irrigation water was less than the soil water deficit before irrigation (partial irrigation).Accordingly there is an additional quantity of water should be added to raise the water soil content to field capacity level. In this case and, if the salinity reaches a harmful level effect on crops, the leaching water must be added to remove the salt from the soil (the additional quantity of water is calculated as depth of extra leaching water) is:

$$(act.R^{*}_{t})_{ki} = ASWD_{ki} + R^{*}_{ki} \quad (26)$$

$$SWDB_{ki} - Irr.D_{ki} = ASWD_{ki} \quad (27)$$

Where:

$(act.\ R^{*}_{t})_{ki}$: Actual depth of irrigation water on the k^{th} irrigation during the i^{th} month, mm.

- Third probability is that, the net amount of irrigation water is greater than the soil water deficit before irrigation. According to the contiguity between the net irrigation water and the soil water deficit the water losses may be divide into two parts:
  1. The first is the surface runoff and this amount of water losses cannot be controlled and goes as surface run off, and
  2. The second is the one third from the field water losses which can be controlled **,Hussein ,2012.** and will be used as a depth of leaching water, the name of this part considered as deep percolation, in this case deep percolation must be checked if it is greater than depth of leaching water therefore, there is no need to add water for purposes of leaching . If deep percolation is less than depth of leaching water therefore, adding leaching dose is needed.

If $Irr.D_{ki} > SWDB_{ki}$, then the are two possibility these are:

1. $Irr.D_{ki} - SWDB_{ki} > R^{*}_{ki}$ then $(act.R^{*}_{t})_{ki} = 0$, and
2. $Irr.D\ ki - SWDB_{ki} < R^{*}_{ki}$ then

$$(act.\ R^{*}_{t})_{ki} = R^{*}_{ki} - [Irr.D\ ki - SWDB_{ki}] \quad (28)$$

3. SAMPLE OF CALCULATION

To simplify discussion, Amara irrigation project in Maysan Governorate was taken as an example. Amara irrigation project is located within the southern zone. This zone has a different soil textured refers to the ancient irrigation zone. At present, this zone has a saline soil to a variable degree of salinity. The design average percentage of additional leaching water requirements for southern Iraq were taken as 19-19.5% from net irrigation requirement, **General Scheme of Water Resource and Land Development of Iraq, 1982**.

Irrigation scheduling

In winter season and during the first month of irrigation scheduling calendar (October), irrigation depth was applied twice a week if it is required, with a chosen time of irrigation, taken into account that this time was not exceed the irrigation interval. In summer season, continuous irrigation is adopted since there is no rainfall during the summer season period and crop water requirements become large during this season. To minimize water losses and avoid plant water stress in summer season, irrigation depth was applied twice a week with an irrigation interval equals irrigation time 3.5 . In this zone, the effective rainfall is not sufficient to supply crops water requirements. In other words, irrigation water is required even in winter season to supply crop water requirements.

Table1. and **Fig.1** show the difference in applied water distribution between applying irrigation scheduling procedure (designed) case taken in account the water leaching requirement and designer

suggestion (general scheme) case. Applied irrigation volumes in scheduled case are less than those allocated to the project, and there is 18% of water lost as drainage water. It is known that the southern zone requires 19-19.5% of water to leach salts, so the 18% of applied water which is lost as a drainage water, is used to leach salts, therefore it can be said that there are no water losses. **Table 1** also shows that 1687.13 million m^3 of water were saved. This is a good result if the plants are not suffering stress.

After checking plant statue by using a water budgeting program it was found that. All winter crops are suffering from stress and soil moisture content is below wilting point at the beginning of growing season. The maximum plant root depth under soil moisture content below the wilting point is approximately 5 (cm) long. It was supposed that this case is an acceptable, since in spite of the plant initially requires high frequent and little quantities of water, "shallow root depth can absorbs required water when it logged to full the soil water reservoir". Since planted crops root depths are between 600–2000 (mm). These root depth "which represents 10% of minimum plant root depth" was considered as little root depth, and under this depth, the plants will not be lost even the soil moisture content is under the wilting point level because the soil water reservoir filled with water at the beginning of scheduling . Winter plants statue is illustrated in the **Fig. 2.**

Fig. 2 shows a good plant status since soil water content curve approximately conforms to field capacity curve. At the beginning of growing season, the soil water content curve overreaches wilting point curve, this is done with root depth not exceeds 60 mm, so it is acceptable as mentioned previously.

Summer crops have two behaviors: the first one is soil water content exceeds wilting point at the beginning of the growing season with root depth not exceeding 60 (mm),the second one is soil water content exceeds wilting point at the beginning of the growing season with root depth exceed 60 (mm), which means losing the crops. **Figs.3** and **4** show these two behaviors, respectively.

Fig. 3 shows summer crop with good status since the soil water content curve is between field capacity curve and readily available water curve except at the beginning of growing season. At the beginning of growing season, the soil water content curve overreaches wilting point curve, this is done with root depth not exceeds 60 mm. In the practice the pre-irrigation is necessary to refill the soil with necessary moisture for seeds growth , so can assumed that there is not water stress at the beginning of crop growth because of sequence irrigation with small irrigation interval (3.5 days)

Fig. 4 shows stressed summer crop with the soil water content exceeds wilting point with root depth not exceeding 60 mm. Perennial crops have no overreaching of wilting point and showing good plant status as shown in the **Fig. 5**.

Leaching Scheduling:

The amount of leaching requirement have been applied when the concentration of soil extract is greater than or equal to critical crop tolerance to salinity (with condition that less than 50% of yield reduction). If the net depth of irrigation water is less than the soil water deficit before irrigation (partial irrigation), accordingly additional quantity of water should be added to raise the water soil content to field capacity. In this cases and, if the salinity reaches a harmful level effect on crops, the leaching water must be added to remove the salt from soil.

In all irrigation cycles during autumn and winter seasons the net depth of irrigation water is greater than the soil water deficit before irrigation (full irrigation) accordingly the contingents between net irrigation depth, soil water deficit will be taken as water losses. In some irrigation applications during winter, spring seasons and these needs to additional quantity of water should be added to raise the water soil content to field capacity.

The difference in applied water distribution between applying leaching scheduling procedure (designed) case and designer suggestion (general scheme) case are shown in **Table 2**. In the first case the applied irrigation volumes in scheduled case are less than those allocated to the project, and there is 13.1 %of water lost as drainage water. In these cases assuming that the water losses cannot be controlled therefore 13.1% are losses and go to the drain and the real need, is 985.24mm depth of leaching water. **Table 2**. also showed that 1658.96 million m^3 of water were saved. This is a good result, if the plants are not suffering stress. In the second case the applied irrigation volumes in a scheduled case are less than those allocated to the project, and there is 13.1% of water lost as drainage water. In these cases, assuming that the water losses can be controlled and part of water losses (deep percolation) plays a role of leaching water depth, and therefore the loss of drainage water became 11.7%, and 188.96 mm of leaching water is needed to leach salt. **Table 2**, also shows that 2134.75 million m^3 of water was saved. This is a good result if the plants are not suffering stress.

Introducing the leaching scheduling procedure a cropping pattern efficient should be used in order to improve the water use efficiency, but without harmful stress to crops. Cropping pattern should be chosen carefully, Amara Irrigation Project with assumed cropping pattern four winter season crops, five summer season crops, and six perennial crops were planted with total cropping intensity equals 114%. The crops are different in degree of response to salinity; some crops can produce acceptable yields at much greater soil salinity than others and this is because some have better able to make the needed osmotic adjustments enabling them to extract more water from a saline soil**, Hussein , 2012.**

The wide range of salt tolerance crops allows for a greater use of moderately saline water, some of there were previously thought to be unusable. Therefore greatly expands the acceptable range of water salinity which is not effect on crop growth, and the yields, so it can considered to be a suitable water for irrigation. With many trials, the right percentages of plant area which improve water saving without losing crops could not be found, in this project it is assumed that there is no portion of plant area for sensitive crops was planted.

For saving crops a 50% yield potential was considered as an index for salinity hazard; another meaning: the depth of leaching water should be add before the soil salinity became less than or equal to the threshold value of 50 % yield potential. It was assumed that the soil salinity level for sensitive crops was 6 ds/m, for moderately sensitive crops was 7.5 ds\m, for moderately tolerant crops was 10 ds\m, and tolerant crop was 12 ds/m **,Hussein ,2012.**

The water source of Amara Irrigation Project is Tigris River in Maysan Government, the mean annual of salt concentration is 1186 ppm.

4. CONCLUSION

1. The comparison between applied discharges using irrigation and leaching scheduling procedure, and the discharge that was suggested by designers are possible; with the constraint that the harmful level of the salt concentration index does not effected on crop growth.
2. Irrigation and leaching scheduling procedure is useful if cropping patterns are chosen carefully. Some of studied of irrigation projects required selecting more suitable cropping pattern; others required only changing the percentage of planted area with each crop.
3. Using percentage of monthly maximum planted crop root depth of scheduling irrigation giving flexibility to have a balance between applied irrigation, saved water, drainage losses, total available water, readily available water, and plant status by control the applied irrigation frequency.
4. Using maximum root depth to estimate the depth of leaching water, and to guaranty that all other root zones will be leached from salt.
5. Percentage of depletion from readily available water does not affect applied depth per irrigation, but it affects applied irrigation frequency during winter season, and for first month of irrigation and leaching scheduling.
6. The salinity of irrigation water affects the depth of leaching water especially; when the salinity of irrigation water high. The monthly applied of leaching water, using scheduling procedure, and for

two cases: case I uncontrolled water losses, and case II controlled water losses are greater than monthly applied of leaching water as suggested by designers(general scheme).

7. There is a difference between the monthly distribution of irrigation water for the assumed two cases of leaching and the suggestion of the designers (general scheme) when used the scheduling of irrigation and leaching water.

REFERENCES

- Allen R.; L. Pereira; D. Raes; M. Smith ,1998, *Crop Evapotranspiration: Guidelines for Computing Crop Water Requirements, Irrig. and Drain.* Paper No. 56, Food and Agricultural Organization of United Nations (FAO), Rome, Italy.

- Al-Furat Center for Studies Design of Irrigation Project, 1992, *The Soil of West Gharraf Project* .

- Al-Haddad, A. H. ,1997, *Irrigation Scheduling in Large Irrigation Project,* PhD. Dissertation submitted to the College of Engineering, University of Baghdad.

- Al-Haddad, A. H. 2001, *Effect of Prescheduled Irrigation on Wheat Growth,* First National Conference in Civil Engineering, College of Engineering, University of Al-Anbar.

- Al-Mesh'hedany, U. N. K. ,2002, *"The Role of Irrigation Scheduling in Crop Production,* M. Sc. Thesis submitted to the College of Engineering, University of Baghdad.

- Antosch, Larry M. ,2007, *Irrigation Water Management for Ohio.* Procedure Guide for the Development and Implementation of a Systematic Water Management Program.

- Ayers,R.S. and Westcot,D.W., *1985, Water Quality for Agriculture. Irrigation and Drainage Paper*, 29,Rev.I. FAO, Rome, 174 p.
- Bakr, T. Sh. ,2011, *Irrigation Scheduling Effect on Water Requirements,* M. Sc. Dissertation Submitted to the College of Engineering, University of Baghdad.

- Boumans, J. H. ,1963, *Some Principles Governing the Drainage and Irrigation of Saline Soil , Reclamation of Salt Effected Soils in Iraq, Pub.* II. ILRI , Wageningen, the Netherlands.

- Broner,I.,2005, *Irrigation Scheduling.* Colorado State University. http://www.ext.colostate.edu/PUBS/crops/04708.html.

- *General Scheme of Water Resources and Land Development of Iraq,1982*, Ministry of Water Irrigation, Iraq.

- Food and Agriculture Organization (FAO),1985, *Water Quality for Agriculture. Irrigation and Drainage,* Paper, 29. Rev. 1. FAO, Rome. 174 p.

- Hoffman, G. J. ,1980, *Guideline for Reclamation of Salt Effected Soil,* Technical Conference, Juar. Mexico., pp: 49-64.

- Hussein, Kh. A. ,2012, *Scheduling of Leaching Requirements to Prevent the Secondary Salinization in the Root Zone,* M. Sc. Dissertation Submitted to the College of Engineering, University of Baghdad.

- Martin, Edward C. ,2009, *Methods of Measuring for Irrigation Scheduling-WHEN,* The University of Arizona Cooperative Extension.

- Nielsen, D. R., J. W. Biggar, and J. N. Luthin, 1966, *Desalinization of Soils under Controlled Unsaturated Conditions,* Int. Commission on Irrigation and Drainage, 6th Congress, New Delhi, India.

- Oster, J. D., Willardson, L. S. and Hoffman, G. J. ,1972, *Sprinkling and Ponding Techniques for Reclaiming Saline Soils,* Transactions ASCE, 15: 1115-1117.

- Reeve, R. C. ,1957, *The relation of Salinity to Irrigation and Drainage Requirements,* 3rd Congress of International Commission on Irrigation and Drainage Transaction, 5(10): 175-187.

- Richard, L. A. (Ed.) et. Al., 1954, *Diagnosis and Improvement of Saline and Alkaline Soils ,Ag.* Handbook No. 60 U.S.D.A. US Salinity Lab. Staff.

- Riffat, R. U. N. ,1999, *Variation of Water Use Efficiency with the Cropping Pattern,* M. Sc. Thesis submitted to the College of Engineering, University of Baghdad.

- Rhoades, J. D. and Merrill, S. D. ,1976, *Assessing the Suitability of Water for Irrigation: Theoretical and Empirical Approaches. In: Prognosis of Salinity and Alkalinity,* Soils Bulletin 31, FAO, Rome, pp. 69–109.

- Rhoades, J.D.,1990, *Determining Soil Salinity from Measuring of Electrical Conductivity ,Commun.* Soil Sci. Plant Anal. 21 :1887-1926.

- Van Der Molen, W. H. ,1979, *Salt Balance and Leaching Requirement, Drainage Principles and Applications,* Vol. II, Wageningen, the Netherlands.

- صفاء نوري حمد. 1996."برمجة الإرواء في مشاريع الري". مجلة هندسة الرافدين, جامعة الموصل, الموصل.
- عامر حسن الحداد. 2000 ."المقارنة بين أسلوبين لغسل التربة الملحية مختلفة النسجة". مجلة الموارد المائية المجلد 19,العدد الثاني, جامعة بغداد.

ABBREVITIONS

% RD =percentage of maximum root depth,%.
%RAW=percentage of depletion from readily available water,%.
act $R*_t$=actual depth of leaching water, mm.
AD =percentage of Allowable depletion,%.
ARD =additional used root depth, mm.
ASWD=additional soil water deficit, mm.
C =conversion factor for units, dimensionless.
C_{DP} = the average salt concentration of the percolated water below the root zone, dimensionless
C_e = the average salt concentration of the soil saturation extract, dimensionless.
C_{fc} =the average salt concentration of the soil solution at field capacity, dimensionless.
C_{iw} =the average salt concentration of irrigation water, dimensionless.
C_o =the conversion factor, dimensionless.
$C_R{}^*$ =the average salt concentration of leaching water, dimensionless.
D_{iw} =depth of irrigation water, mm.
D_s =soil depth, mm.
ER = monthly effective rainfall, mm/month.

EC_e = electrical conductivity as measured in the soil saturation extract, crop tolerant, dS/m.
EC_{fc} =electrical conductivity of soil extract at field capacity, dS/m.
EC_{iw} =electrical conductivity of irrigation water, dS/m.
EC_o =electrical conductivity of soil before leaching (initial value), dS/m.
Etc = actual monthly crop evapotranspiration, mm/month.
Eto = monthly reference crop evapotranspiration**,** mm/month**.**
ds/m = measuring unit of electrical conductivity expressed as dicesemens per meter.
F = leaching efficiency coefficient, fraction of unity.
FC = field capacity,%.
GIS = geographic Information System, dimensionless.
I =index for time in month, month.
Irr.D = infiltrated net irrigation water depth, mm.
IE = expected irrigation efficiency,%.
IRR_{time}=irrigation time, day.
ISWC=initial soil water content, mm.
J =index for crop grown in the project, dimensionless.
k = index for time in days, day.
K_c = crop coefficient, %.
LR = leaching Requirement, %.
N = number of crops grown in the project, dimensionless.
NA = net irrigated project area, don.
NA I = net area in the project planted during thei^{th} month, don.
NAj = net area planted with the j^{th}crop, don.
ND =number of days in month, day.
$NI_{req.}$=net volume of water required,m^3.
NQ req=net continuous discharge required, m^3/sec.
OP = osmotic potential, bars.
PA = percentage of area planted with each crop, %.
PWP = permanent Wilting point,%,
Q max= maximum discharge m^3/sec.
RAW= readily available water in the root zone, mm.
RD j= root depth at any time of the j th crop, mm.
R* = depth of leaching water, mm.
R*t = total depth of leaching water, mm.
SWC= soil water content in the root zone, mm.
SWC (allow)= allowable soil water content, mm.
SWD = soil water deficit, mm.
SWDA= soil water deficit after irrigation, mm.
SWDAL= soil water deficit after irrigation at the last day in the month, mm.
SWDB= soil water deficit before irrigation, mm.
SWDL= percentage of Soil water deficit after irrigation at the last day in the month, %,
TAW = total available water, mm.
URD = used root depth, mm.
WD = water duty, L/sec/ha.
$WETc_i$= monthly weighted average of crop evapotranspiration for certain cropping pattern during the i^{th} month (mm/month).
Z = the amount of salt added after each irrigation. gram.
θ_{fc} = soil moisture content at field capacity, fraction of unity.
θ_{vs} = soil moisture content at saturation, fraction of unity

Table 1. Monthly and annual net and gross amounts of water for Amara irrigation project.

Month	From irrigation scheduling (Designed)		From general scheme
	Net volume of irrigation $10^6\ m^3$	Gross volume of irrigation $10^6\ m^3$	Net volume of irrigation $10^6\ m^3$
Jan.	23.33	28.11	30.93
Feb.	58.33	70.28	53.26
Mar.	81.67	98.40	88.18
Apr.	119.96	126.60	261.40
May	125.81	126.51	381.03
Jun.	111.57	112.45	531.48
July	123.85	126.51	528.56
Aug.	123.29	126.25	478.37
Sept.	122.86	126.51	223.01
Oct.	84.34	89.23	98.49
Nov.	35.00	42.17	52.55
Dec.	46.67	56.23	16.55
Sum	1056.68	1129.25	2743.81
Percentage of drainage water		18	
Saved volume of water $10^6\ m^3$		1687.13	
Percentage of leaching requirements		19.5	
Percentage of water losses		....	

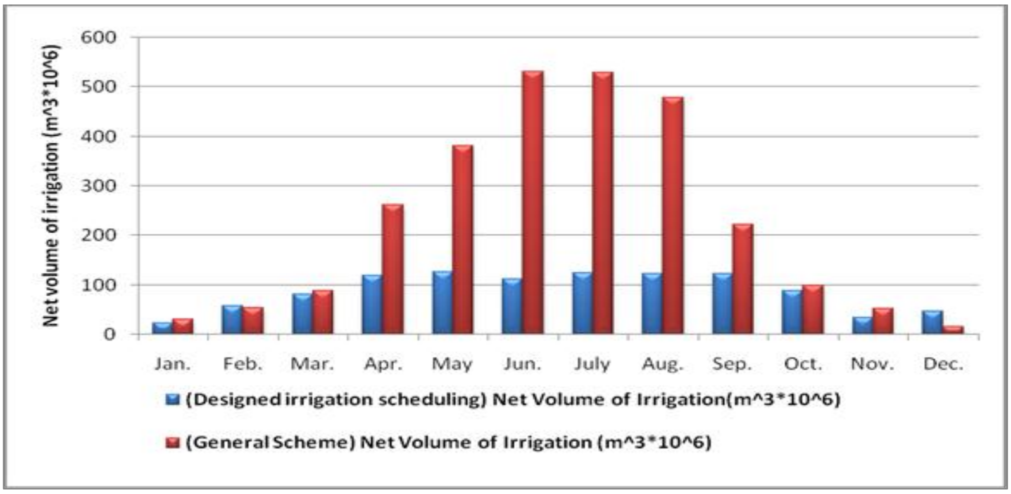

Figure 1. Variation of monthly applied irrigation volumes distribution by using irrigation scheduling and by designer suggestion.

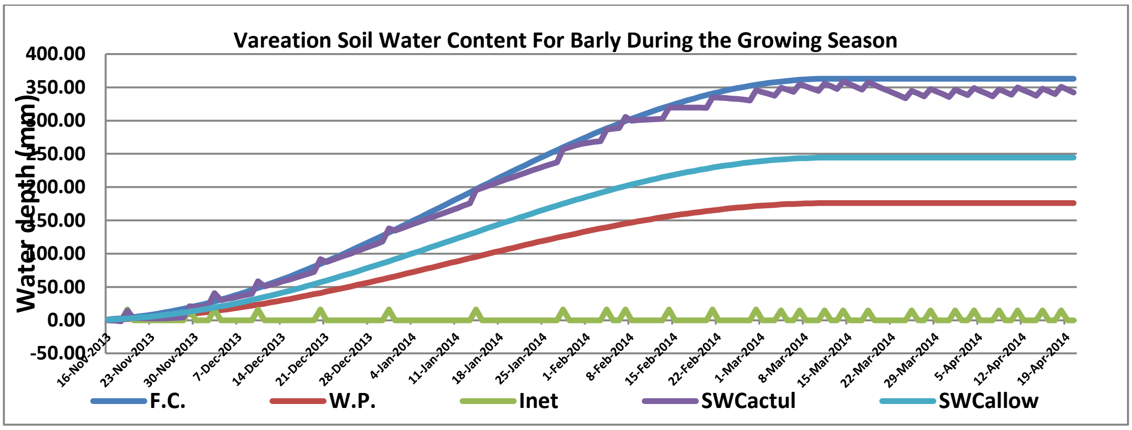

Figure 2. Variation of soil water content for Barley during the growing season for Amara irrigation project.

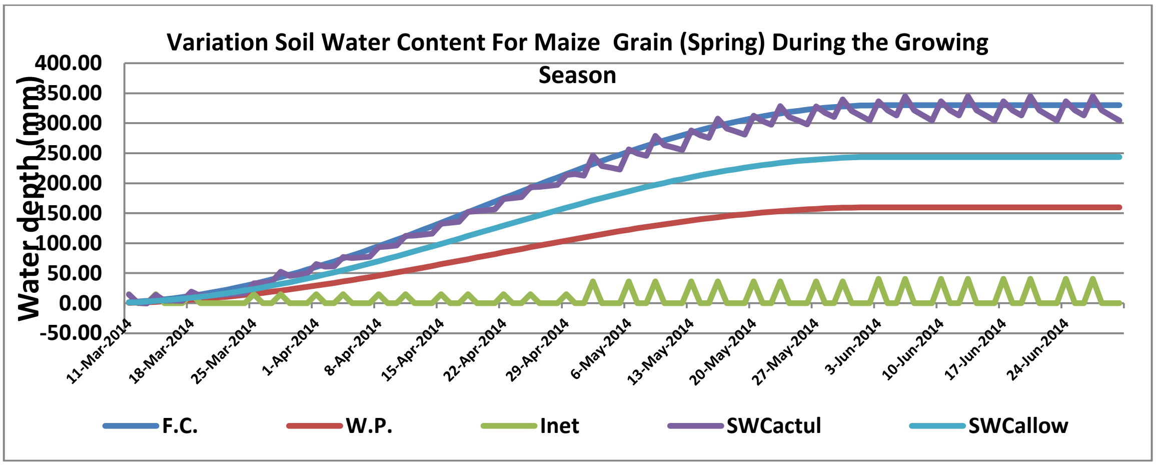

Figure 3. Variation of soil water content for maize grain (spring) during the growing season for Amara irrigation project.

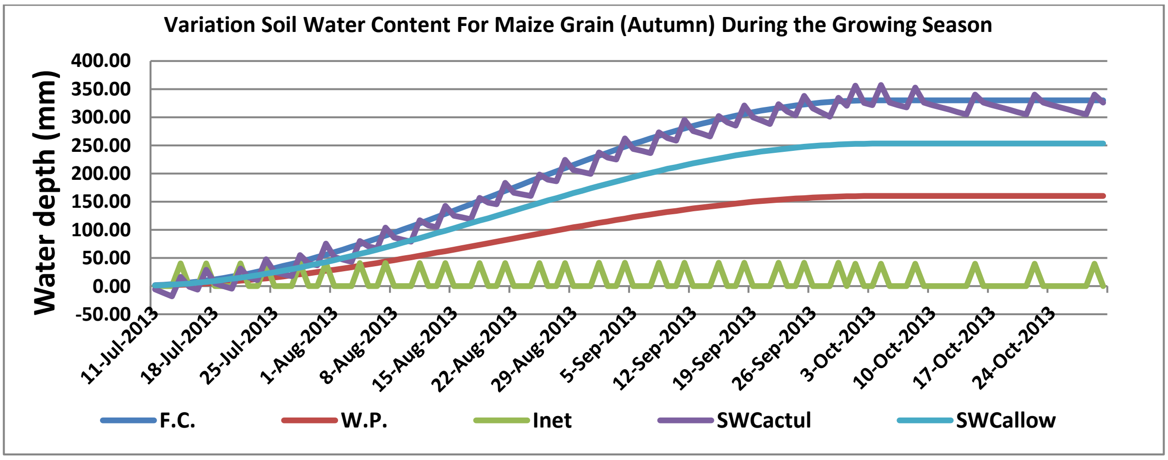

Figure4. Variation of soil water content for maize grain (autumn) during the growing season for Amara irrigation project.

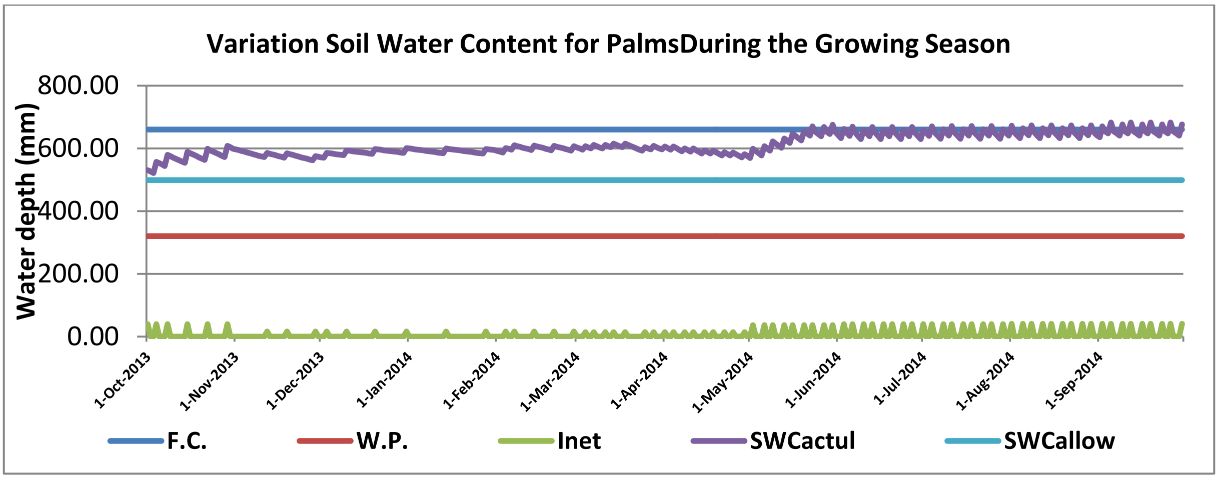

Figure 5. Variation of soil water content for palms during the growing season for Amara irrigation project.

Table 2. Monthly and annual irrigation water amounts for Amara Irrigation Project, for period 2013-2014.

Months	From leaching scheduling		Estimated by general scheme (LR =19.5%)
	Designed I net volume of irrigation water, 10^6 m^3	Designed II net volume of irrigation water, 10^6 m^3	Net volume of irrigation water, 10^6 m^3
Jan.	28.78	24.72	36.96
Feb .	111.73	64.40	63.65
Mar .	226.63	97.79	105.37
Apr.	309.85	138.09	312.37
May	149.58	129.10	455.33
Jun .	124.06	117.88	635.12
Jul .	139.03	133.74	631.63
Aug .	137.38	129.86	571.65
Sept .	144.41	131.42	266.49
Oct.	124.76	92.25	117.69
Nov .	71.46	37.89	62.79
Dec.	52.42	47.17	19.98
Sum.	1620.09	1144.31	3279.03
Percentage of drainage water %	13.1	11.7	
Saved volume of water 10^6 m^3	1658.96	2134.75	
Aver. Percentage of leaching requirements, %	40.04	7.68	19.5
Actual water losses, mm	452.06	310.67	……

Effect of Initial Water Content on the Properties of Compacted Expansive Unsaturated Soil

Mohammed Yousif Fattah
Prof. in Building and Construction Dept.,
University of Technology,
Email: myf_1986@ yahoo.com

Aysar Hassan Al-Lami
Student at Department of Civil Engineering College of Engineering, University of Baghdad
Email: aysar_lami@yahoo.com

Mahmood D. Ahmed
Asst. Prof.,Civil Engineering Department
University of Baghdad
Mahmood_baghdad@yahoo.com

ABSTRACT

Unsaturated soil can raise many geotechnical problems upon wetting and drying resulting in swelling upon wetting and collapsing (shrinkage) in drying and changing in the soil shear strength. The classical principles of saturated soil are often not suitable in explaining these phenomena. In this study, expansive soil (bentonite and sand) were tested in different water contents and dry unit weight chosen from the compaction curve to examine the effect of water content change on soil properties (swelling pressure, expansion index, shear strength (soil cohesion) and soil suction by the filter paper method). The physical properties of these soils were studied by conducting series of tests in laboratory. Fitting methods were applied to obtain the whole curve of the SWRC measured by the filter paper method with the aid of the (Soil Vision) program. The study reveals that the initial soil conditions (water content and dry unit weight) affect the soil cohesion, soil suction and soil swelling, where all these parameters marginally decrease with the increase in soil water content especially on the wet side of optimum.

Key words: expansive soil, swelling, filter paper, SWRC, swelling pressure.

تاثير المحتوى المائي الابتدائي على خصائص تربه عراقية انتفاخية محدوله غير مشبعة

د. محمد يوسف فتاح
استاذ في قسم هندسة البناء و الانشاءات
الجامعة التكنلوجية

ايسر حسن اللامي
طالبة في قسم الهندسة المدنية
جامعة بغداد

د. محمود ذياب احمد
استاذ مساعد في قسم الهندسة المدنية
جامعة بغداد

الخلاصة

التربه غير المشبعة يمكن ان تثير العديد من المشاكل تحت تاثير الترطيب و التجفيف مسببة الانتفاخ تحت تاثير الترطيب و الانكماش تحت تاثير التجفيف وتغيير في مقاومة القص للتربه. المبادئ الاساية للترب المشبعة هي عادة غير مناسبة في تفسير مثل هذه الظواهر. في هذه الدراسة, التربة الانتفاخية من (البنتونايت و الرمل) تمت دراستها في محتوى مائي و كثافة اوليه مختلفة من منحني الرص المختبري لدراسة تاثير تغير المحتوى المائي على خصائص التربة (الضغط الانتفاخي, معدل الانتفاخ,مقاومة القص (تماسكية التربة) و اجهاد المص للتربة بطريقة ورق الترشيح). الخصائص الفيزيائية للتربة تمت دراستها بالاستعانة بالعديد من الفحوص المختبريه. تم استخدام المعادلات التكميلية لايجاد المنحني الكامل للعلاقة بين المحتوى المائي و اجهاد المص في التربه بالاستعانة ببرنامج (Soil Vision). بينت الدراسة بان ظروف التربة الابتدائية (المحتوى المائي و الكثافة الاوليه) تؤثر على

تماسكية التربة و انتفاخيتها و اجهاد المص فيها حيث ان هذه الخصائص الثلاثة تقل بشكل كبير بزيادة المحتوى المائي الابتدائي خاصة على الجهة الرطبة من منحني الرص المختبري.

الكلمات الرئيسيه : تربة انتفاخية, الانتفاخ, ورق ترشيح, الضغط الانتفاخي

1. INTRODUCTION

The soil forming at shallow depths in the arid and semi-aired regions and the compacted soil used in highways, earth dams, embankments and airport runways are in unsaturated conditions. Whenever water interacted to such soils, volume changes could happen. Such a reaction between the soil and the water may cause collapse or swelling to soils depending on soil conditions. Usually these volume changes are small in magnitude. However, for particular types of soils (expansive soils), these volume changes are of considerable order. Such soils either suck in or lose a large amount of water during hydration or dehydration process. For shallow foundations, soil swelling and soil shrinkage may cause considerable problems, because the wetting may cause a reduction in the soil shear strength and an increase in the soil hydraulic conductivity and shrinkage may cause cracks in different parts of the structure, **Abed, 2008**.

Many financial losses are reported all over the world due to the lack of the correct understanding of the behavior of expansive soil. To close the knowledge gap in this field, serious research on this topic started in the middle of 1960s. Several conferences have been held since then and produced the so called " the unsaturated soil mechanics" as an independent science with extended rules as compared to classical soil mechanics. Today studying the expansive soil cannot be separated from the unsaturated soil mechanics, **Smith, 2003**.In Iraq, expansive soils spread in large area in the north, middle and south of Iraq.

2. UNSATURATED SOILS

Unsaturated soils may be defined as the soil which has four phases: soil, water, air and air-water interface or the "contractile skin". The contractile skin is considered as a fourth phase since it has definite bounding and different properties from the contiguous materials". The presence of small air in soil renders the soil to be unsaturated, **Fredlund, and Rahardjo, 1993**. The soil below the water table is fully saturated and the pore water pressure has a positive value. The ground water table is considered as the line at which the pore water pressure will be equal to zero (relative to atmospheric). Above the water table the soil will be in an unsaturated state where the pore water pressure has a negative value.

2.1 Soil Suction

Porous materials like soil have the ability to absorb and retain water. This property has an engineering definition which is "suction". Suction may be defined as the free energy of soil water. Suction in soil consists of two components matric (matrix) suction and osmotic suction, **Fredlund, and Rahardjo, 1993**. In unsaturated soil mechanics, the matric suction is notably defined as the difference between the pore air and pore water pressure (u_a-u_w). The summation of these components gives the total suction. Matric suction generates from capillarity, texture, and surface adsorption forces, while the osmotic suction comes from the effect of the dissolved salts in the soil water. According to, ,**Fredlund, 1969,** the osmotic suction is always neglected. This relation can be formed in an equation as follows:

$$h_t = h_m + h_\pi \qquad (1)$$

where h_t = total suction (kPa),
h_m = matric suction (kPa),
h_π = osmotic suction (kPa).
The magnitude of soil suction ranges from a lower limit equals to zero when the pore water pressure equals to zero and theoretically no dissolved salts in soil water and an upper limit which equals to 1,000,000 kPa. This case occurs when there is zero water content (dry soil).

2.2 The Soil Water Characteristic Curve (SWCC)
The soil water characteristic curve may be defined as the graphical representation of the mathematical relation between the volumetric water content (the ratio of volume of water to the total volume of soil), gravimetric water (the ratio of the mass of water to the mass of solids) or the degree of saturation (S) and the matric suction, **Fredlund, et al., 2001**. In case of increasing the suction (drying) for initially saturated, slurry or compacted, soils the resulted curve is called the (SWCC), while in case of initial unsaturated state soils, the curve will identify as the soil water retention curve (SWRC) which has the same definition, ,**Al-Badran, 2011**. The SWCC may be measured by different methods: a) experimental methods (i. e. the Fredlund and Xing and the van Genuchten equations used in this paper), b) estimated from the pore size distribution (PSD), c) experimental methods (i. e. the filter paper method used in this paper).

2.3 The Filter Paper Method
The initial water content of the compacted soil appears to have direct relationship to the soil matric suction, while the osmotic suction does not seem to be sensitive towards the changes in the soil water content. It is one of the indirect methods for measuring matric and osmotic suction, the filter paper will absorb the moisture from the soil until reaching the equilibrium state (by either liquid or vapor moisture exchange) where the water content will be equal in the filter paper and the soil, **Bulut, et al., 2001**.

The liquid exchange will happen when the filter paper is in contact with the soil and in this case the matric suction will be measured, while the vapor exchange will happen when the filter paper is not in contact with the soil from which the total suction will be measured. This method however will need a calibration for suction versus water content relation in filter paper. The main advantages of this method are the low cost as compared to the other methods and the capability to measure wide range of suction (full range of suction in case of contact filter paper). The accuracy of the filter paper technique depends on the accuracy of the suction versus water content calibration curve. The filter paper used should be the ash free filter paper like the most commonly used ones Whatman No.42 and Schleicher and Schuell No.589 WH.

2.4 Expansive Unsaturated Soil
Expansive soil is that kind of problematic soil which shows a significant amount of volume changes upon wetting and drying. The amount of swell generally increases with the increase in soil's plasticity index, **Ameta, et al., 2008**.

Expansive soil problems to foundations are heaving, cracking and break up to light structures like pavements. The effect of heave is to reduce the soil shear strength and thus reducing the stability of the structure and causing total and differential settlement, **Sridharan, et al., 1987**. It is true to consider the expansive soil as soft soil under wet condition. Swelling soil can virtually control the behavior of any soil type if the amount of clay is more than 5% by weight, **Rogers, et al., 1993**. The clay minerals containing montmorillonite show significant swelling upon wetting as compared to the clay soil containing other clay minerals like kaolinite or illite which shows significant decrease in volume upon drying but limited increase in volume caused by wetting, **Chen, 1975**.

2.5 Mechanism of Swell

Mitchell, 1993. showed that soil swelling happens due to several factors:

1-Capillary Imbibition: The surface tension caused by air in the unsaturated soil and the soil suction caused water adsorption to the soil system.

2-Osmotic Imbibition: The double layer acts as semi permeable membrane with difference in the ion's concentration inside and outside of it causing the flow of water and increase in the soil volume.

3- Hydration of Exchangeable Cations: as described previously the cations attracted to the negatively charged soil surface causing an increase in the volume of the double layer. Then these cations will be hydrated causing an increase in the ion's volume and as a result an increase in the soil volume.

4-Van Der Waals forces: these forces are secondary in-directional forces and less strong than the hydrogen bonding and they connect the montmorillonite sheets, when adsorption of water happens a repulsion between these forces will happen leading to an increase in the volume of soil.

The objective of the present work is to model the behavior of the expansive soil in the framework of unsaturated soil mechanics. This work was used to predict the volume changes associated with the changes in soil suction.

3. EXPERIMENTAL WORKS AND MATERIAL USED

In this study, the aim was to study the effect of initial water content on the properties of compacted expansive soil. Different mixtures of bentonite (brought from Al-Falouja city west of Baghdad) with sand (from Ali Al-Gharbi city south of Baghdad) were tested till getting the mixture of 80% of bentonite to 20% of sand (B-S) by dry weight depending on the required plasticity indices. The physical and chemical properties of these soils are presented in **Table 1.** and **Table 2**. respectively. **Fig. 1** shows the grain size analysis of the soils by the wet sieving method according to ASTM D 1140-00 for bentonite and the (B-S) soil and the dry sieving according to ASTM D 422-02 was used to the sand soil. **Fig. 2** shows the compaction curve of the soils.

Four points were chosen from the compaction curve, **Fig. 2** (two from the dry side, the optimum moisture content and one from the wet side). **Table 3,** shows the water content and the dry unit weight used to prepare the samples. The oven dried soil was left to cool down at room temperature and then mixed with the required water to get the targeted water content. The samples were left to cure in two plastic bags for one day as followed by ,**Agus, et al., 2010,** and then prepared by the moist tamping system recommended by ,**Chao, 2007.**

3.1 Measurements of Soil Suction

The test was done according to ,**ASTM D, 5298-03**. The soil samples were remolded in two odometer rings 75 mm in diameter and 19 mm in height, three filter papers (Whatman 42) were sandwiched between these two soil samples and two filter paper were separated from the soil sample by a PVC ring of 2.5 cm in thickness as followed by ,**Fattah, et al., 2013. a and b.** This group of soil samples and filter papers were placed in glass cylinder where the samples filled about two third of the cylinder space as recommended by ,**Bulut, et al., 2001.** to reduce the equilibrium time. The samples were left to get the equilibrium condition for about ten days ,**Sridharan et al., 1987**. Then the wet filter papers were weighed to the nearest 0.0001gm quickly as possible, the filter papers were placed in a jarred tins and inserted in the oven of 105 ^{0}C for six hours and weighed again as recommended by ,**Chao, 2007.**

3.2 Unconfined Compression Test

The unconfined compression test was done according to the ,**ASTM D, 2166-00**. The soil samples were remolded in the unconfined compression tube 3.8 cm in diameter and 15 cm in length, the extracted samples were cut to produce a soil sample of only 7.6 cm length which will be tested in the triaxial machine at a rate of 1.5 mm/minute. This test is basically used to quickly find the unconfined compression strength (q_u) of the soil by which the shear strength of the soils can be computed as:

$$c = q_u/2 \qquad (2)$$

where c is the soil cohesion.

3.3 The Swelling Test

The test was done according to ,**ASTM D, 4829-03**. In these tests, the oven dried soil passing 2mm sieve was mixed with the required amount of water and were remolded at the oedometer ring (75 mm in diameter and 19 mm in height) but the sample was prepared by a height equal to 14 mm to insure that the specimen will be laterally confined ,**Al-Omari, et al., 2010**. A load of about 7 kPa was applied as seating pressure, left for ten minutes then an initial reading was recorded. The soil sample was submerged with distilled water for 24 hours then the final reading was recorded. To measure the swelling pressure, weights will be added in increments to the soil sample to get the dial gage reading zero again.

4. RESULTS OF TESTS

4.1 Results of Unconfined Compression Test

Fig. 3 shows the relation between the unconfined compressive strength and the initial water content of the B-S soil. The figure shows that the unconfined compressive strength (q_u) decreased with the increase in the soil water content from 479 kPa to 320 kPa when the water content increased from 23% to 30.5%. Suction contributes to increase the soil strength which is reflected as the shear strength contribution due to suction (i.e., $Ø^b$), the cohesion in unsaturated soil is combined of two components; the effective cohesion and the cohesion due to suction, Eq. (3), **Fredlund, and Rahardjo, 1993.**

$$c = \acute{c} + (u_a - u_w) \tan \varnothing^b \qquad (3)$$

However, the ($\varnothing^b$) decreases with the increase in soil suction but in the case of undrained loading condition, the increase in the soil shear strength due to applying pressure is greater than the decrease in shear strength due to decreasing the matric suction, where the specimens tested with lower water contents have lower shear strength in drained loading conditions, these specimens show higher strength in the undrained condition, **Vanapalli, et al., 1999**. The initial matric suction of specimen compacted at dry of optimum and optimum water content is higher compared to specimen compacted wet of optimum. Due to this reason, specimen at dry side of optimum and at optimum show more resistance to deformation than specimen wet of optimum, where the soil strength and stiffness increases with the increase in soil suction as stated by ,**Nishimura, and Vanapalli, 2004**.

4.2 Results of Swelling Tests

Fig. 4 shows the relation between the swelling pressure and the initial water content, while **Fig. 5** shows the relation between the expansion index and the initial water content of soil suction. The figures show that the swelling pressure and the expansion index decrease with the increase in the soil initial water content and that could be attributed to the soil structure which is more dispersed at higher water contents and the natural desire of the soil to imbibe water to satisfy the double layer. This desire decreases with increasing water content, **Sudjianto, et al., 2009**. The results show that compacting the expansive soil on the wet side of optimum is capable of removing major component of swelling pressure from 275 to 162.5 kPa when the moisture changes by 7.5 %. According to ,**Ameta, et al., 2008**. the swelling pressure increases with the increase in the dry unit weight and decreases with the increase in the initial molding water content, however the effect of the initial molding water content is more effective than the dry unit weight in reducing or increasing the swelling pressure especially on the dry side of optimum.

,Zumrawi, 2013, showed that there is an inverse linear relationship of the swelling percent and the swelling pressure with the initial water content with constant dry unit weight, while a linear relationship may be obtained between the swelling percent and swelling pressure with the initial dry unit weight if the initial water content is constant. The same conclusion was obtained in this work but the relation is not linear since both the initial water content and the initial dry unit weight were not constant.

4.3 Results of the Filter Paper Test

Fig. 6 shows the relation between the initial soil water content with the total and matric suction, while **Fig. 7** shows the relation between the filter paper water content and the total and matric suction. The figures show a linear relationship between the suction (total and matric) with filter paper water content for both soils showing a linear increase in suction with the decrease in the filter paper water content. The results also show that the suction (total and matric) decreases with the increase in the soil water content but this relation does not have a linear trend. The rate of increasing the water content is not equal to the rate of decreasing the soil suction. The inverse relationship between the water content or the soil degree of saturation with suction could be explained by the fundamental meniscus theory as follows, when the water content increases, the radius (Rs) of the meniscus will also increase. When (Rs) increases, the pressure difference between the pore air pressures and the pore water pressure (matric suction) will decrease as illustrated in Eq. (4), ,**Ravichandran, and Krishnapillai, 2011**.

$$u_a - u_w = 2T_s/R_s \tag{4}$$

where: T_s is the surface tension.

Fig. 8 shows the SWRC as measured by the Fredlund and Xing equation with the aid of Soil Vision program after inserting the required soil properties (specific gravity, dry unit weight, grin size analysis and at least three points of water content with corresponding suction measured by the filter paper method). **Fig. 9** shows the SWRC estimated by van Genuchten equation.

4.4 Relations between the Soil Suction and the Unconfined Compressive Strength

Fig. 10 shows the relation between the soil suction with the unconfined compressive strength of the soil where a nonlinear increase in the unconfined compressive strength with the both suction components due to the effect of suction to increase the soil resistance to deformation and increasing the soil strength.

By increasing the soil suction the soil wetness decreased and the contact between the soil particles decreased causing reducing in the soil cohesion.

5. CONCLUSIONS

Based on the experimental results of the experimental work, the following conclusions may be obtained:

1- The soil unconfined compressive strength increased with the increase in soil suction and with decrease the soil water content, where the soil cohesion decreased from 248.5 to 134 kPa when the initial water content increased by 7.5% due to the effect of matric suction which leads to increase the soil cohesion component of soil shear strength.
2- The swelling potential of the soil increased with increase of soil suction and with the decrease in the soil initial water content and this increase is greater for samples prepared at the dry of optimum water contents. The swelling pressure decreased from 287.5 to 162.5 kPa and the expansion index decreased from 276 to 160.8 when the moisture changes by 7.5%. The natural desire of the soil to imbibe water to satisfy the double layer decreases with increasing water content.
3- Both total and matric suction decreased with the increase in the initial soil water content and a linear relationship was obtained between the two suction components and the filter paper water content.

REFERENCES

- Abed, A., 2008. *Numerical Modeling of Expansive Soil Behavior,* Ph.D. Thesis, University of Stuttgart.
- Agus, S. S., Schanz, T., Fredlund, D. G., 2010. *Measurements of Suction versus Water Content for Bentonite – Sand Mixtures,* Geotechnical testing Journal Vol. 126, No.2, pp. 179-190.
- Al-Badran, Y. M. H., 2011. *Volumetric Yielding Behavior of Unsaturated Fine-Grained Soils,* Ph.D. Thesis, Faculty of Civil and Environmental Engineering, University of Bochum, Germany.
- Al-Omari, R. R., Ibrahim, S. F. and Al-Bayati, I. K., 2010. *Effect of Potassium Chloride on Cyclic Behavior of Expansive Clays,* International Journal of Geotechnical Engineering, Vol. 4, No.2, pp. 231-239.
- Ameta, N. K., Purohit, D. G. M. and Wayal, A.S., 2008. *Characteristics, Problems and Remedies of Expansive Soils of Rajasthan, India,* Electronic Journal of Geotechnical Engineering, EJGE, Vol.13.
- ASTM D 1140-00, 2000. Standard Test Methods *for Amount of Material in Soils Finer Than the No. 200 sieve, Reprinted from the Annual Book of ASTM Standards.* Copyright ASTM, Vol.4, No.8.
- ASTM D 2166-00 , 2000. *Standard Test Method for Unconfined Compressive Strength of Cohesive Soil,* Reprinted from the Annual Book of ASTM Standards. Copyright ASTM, Vol.4, No.8.
- ASTM D 2487-00, 2000. *Standard Practice for Classification of Soils for Engineering Purposes* (Unified Soil Classification System*), Reprinted from the Annual Book of ASTM Standards. Copyright ASTM, Vol.4, No.8.*
- ASTM D 422-02, 2012. *Standard Test Method for Particle-Size Analysis of Soils,* Reprinted from the Annual Book of ASTM Standards. Copyright ASTM, Vol.4, No.8.

- ASTM D 4254-00, 2000. *Standard Test Methods for Minimum Index Density and Unit Weight of Soils and Calculation of Relative Density,* Reprinted from the Annual Book of ASTM Standards. Copyright ASTM, Vol.4, No.8.
- ASTM D 4318-00, 2000, *Standard Test Methods for Liquid Limit, Plastic Limit and Plasticity Index of Soils,* Reprinted from the Annual Book of ASTM Standards. Copyright ASTM, Vol.4, No.8.
- ASTM D 4829-03, *2003, Standard Test Method for Expansion Index of Soils,* Reprinted from the Annual Book of ASTM Standards. Copyright ASTM, Vol.4, No.8.
- ASTM D 5298-03, 2003. *Standard Test Method for Measurements of Soil Potential (Suction) by Filter Paper,* Reprinted from the Annual Book of ASTM Standards. Copyright ASTM, Vol.4, No.8.
- ASTM D 698-12, 2012. *Standard Test Methods for Laboratory Compaction Characteristics of Soil Using Standard Effort (600KN-m/m^3),* reprinted from the Annual Book of ASTM Standards. Copyright ASTM, Vol.4, No.8.
- ASTM D 854-00, *2000. Standard Test Methods for Specific Gravity of Soil Solids by Water Pycnometer*, Reprinted from the Annual Book of ASTM Standards. Copyright ASTM, Vol.4, No.8.
- Budhu, M., 2011, *Soil Mechanics and Foundations*, University of Arizona, USA.
- Bulut, R., Lytton, L. and Wray, W. K., 2001, *Soil Suction Measurements by Filter Paper*, Geotechnical Special Publication, No. 115., Proceedings of Geo-Institute Shallow Foundation and Soil Properties Committee Sessions at the ASC,E 2001,Civil Engineering Conference, Texas, pp. 243-261.
- Chao, K. H., 2007, *Design Principles for Foundations on Expansive Soil,* Ph.D. thesis, Colorado State University.
- Chen, F.H., 1975, *Foundations on Expansive Soils*, Elsevier, Amsterdam.
- Fattah, M. Y., Ahmed, M. D. and Mohammed, H.A., 2013a, *Behavior of Partially Saturated Cohesive Soil under Strip Footing,* Journal of Engineering, Vol. 19, No.3, pp. 298-311.

- Fattah, M. Y., Yahya, A. Y., Al-Hadidi, M. Th. and Ahmed, B. A., 2013b, *Effect of Salts Content on Total and Matric Suction of Unsaturated Soils,* European Scientific Journal ESJ, Vol.9, No.9.
- Fredlund, D.G., 1969, *Consolidometer Test Procedural Factors Affecting Swell Properties, 2nd International Conference on Expansive Clay Soils,* Texas, U.S.A., pp. 435-456.
- Fredlund, D. G., and Rahardjo, H., 1993, *Soil Mechanic for Unsaturated Soils,* John Wiley & Sons Inc. New York, USA.
- Fredlund, D. G., Rahardjo, H., Leong, E. C., and Ng, C. W. W., 2001, *Suggestions and Recommendations for the Interpretation of Soil–Water Characteristic Curves*, Proc. 14th Southeast Asian Geotechnical Conference, Hong Kong, pp. 503 – 508.
- Mitchell, J. K., 1993, *Fundamentals of Soil Behavior*, 3rd edition, John Wiley and Sons, New York, USA.
- Nishimura T. and Vanapalli S. K., 2004, *Shear Strength Behavior of an Unsaturated Soil in Low and High Suction Range under Constant Volume Conditions, 57th Canadian Geotechnical Conference, Quebec, section 6E, pp.17-24.*
- Ravichandran, N. and Krishnapillai, S. H., 2011, *A Flexible Model for Moisture-Suction Relationship for Unsaturated Soils and its Application,* International Journal of Geosciences IJG, Vol.2, No.3, pp. 204-213.
- Rogers, J. D., Olshansky, R. and Rogers R. B., 1993, *Damage to Foundations from Expansive Soils*, Claims People, Vol. 3, No.4, pp.1-4.
- Smith, P. G. C., 2003.,*Numerical Analysis of Infiltration into Partially Saturated Soil Slopes,* Ph.D. Thesis, Department of Civil and Environmental Engineering, University of London.
- Sridharan, A., Rao, A.S. and Sivapullaiah, P.V., 1987, *Swelling Pressure of Clays, Geotechnical Testing Journal, American Society for Testing and Materials,* Vol. 9, No.1, pp. 24-33.
- Sudjianto, A. T. Suryolelono, K.B., Rifa, A. and Mochtars, I. B., 2009,*Behavior of Expansive Clay of Ngawi Region (East Javal) Under Water Content Variation,* Civil Engineering Dimension, Vol.11, No. 2, pp. 100-105.

- Vanapalli, S. K., Fredlund, D. G. and Pufahl, D. E., 1999. *The Relationship between the Soil Water Characteristic Curve and the As-Compacted Water Content Versus Soil Suction for a Clay Till*, Proceedings of the 11th Pan American Conference on Soil Mechanics and Geotechnical Engineering, pp.991-998.
- Zumrawi, M. E., 2013, *Swelling Potential of Compacted Expansive Soils*, International Journal of Engineering Research and Technology (ISERT), Vol. 2, No. 3, pp. 1-6.

Table 1. The physical properties of soils prepared.

Physical Properties	B-S	Specification
Specific gravity (Gs)	2.83	ASTM D 854
Liquid Limit (L.L)	104	ASTM D 4318
Plastic Limit (P.L)	41	ASTM D 4318
Plasticity Index (P.I)	63	ASTM D 4318
% clay	55	ASTM D 1140, D 422-02
% silt	23	
% sand	22	
Activity (A) %	1.15	Budhu, 2011
Optimum Moisture Content % (O.M.C)	28	ASTM D 698-12
Maximum Dry Unit Weight $(\gamma_{dry})_{max}$ (kN/m^3)	14.976	ASTM D 698-12
Minimum Dry Unit Weight (kN/m^3)	---	ASTM D 4254
C_c, C_u for Sand	---	ASTM D 4254
e (void ratio)	0.89	----
Soil Symbols according to USCS	CH	ASTM D 2487

Table 2. Chemical properties of soils used.

Chemical Properties	Bentonite	Sand
SO_3	2.27	0.05
Organic	0.59	Nil
Gypsum	4.7	0.1075
TSS	6.1	0.15
SiO_2	51.92	55.55
CaO	1.96	11.25
Na_2O	0.13	1.73
MgO	0.27	3.9
Cl	0.17	0.06
pH	9.14	8.65

Table 3. Water content and dry unit weight of soil sample.

Soil Type	Water Content	γ_{dry} (kN/m^3)
B-S mixture	23%	14.66
B-S mixture	25.5%	14.90
B-S mixture	28%	14.976
B-S mixture	30.5%	14.90

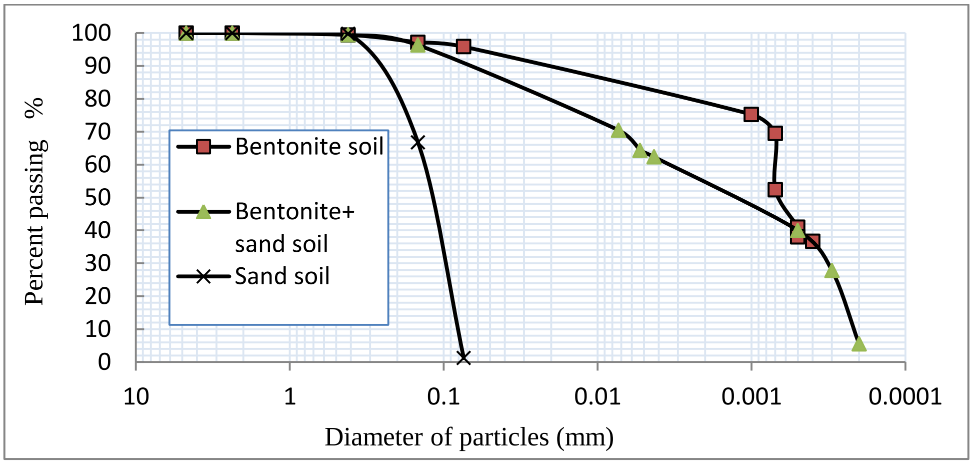

Figure 1. The grain size analysis of soil used.

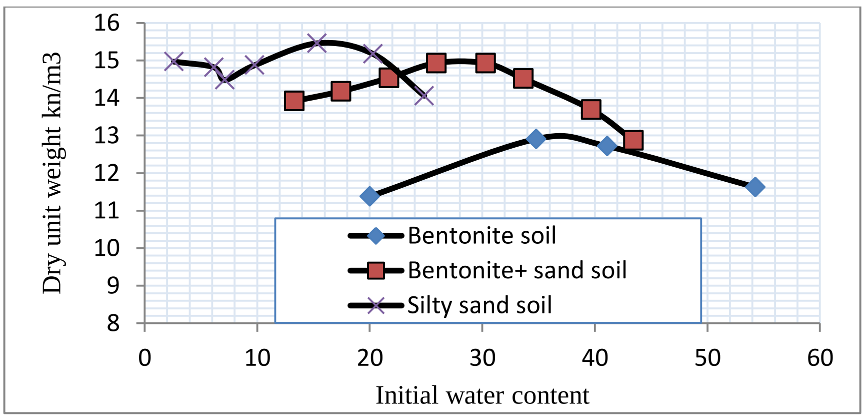

Figure 2. compaction curve of soil used.

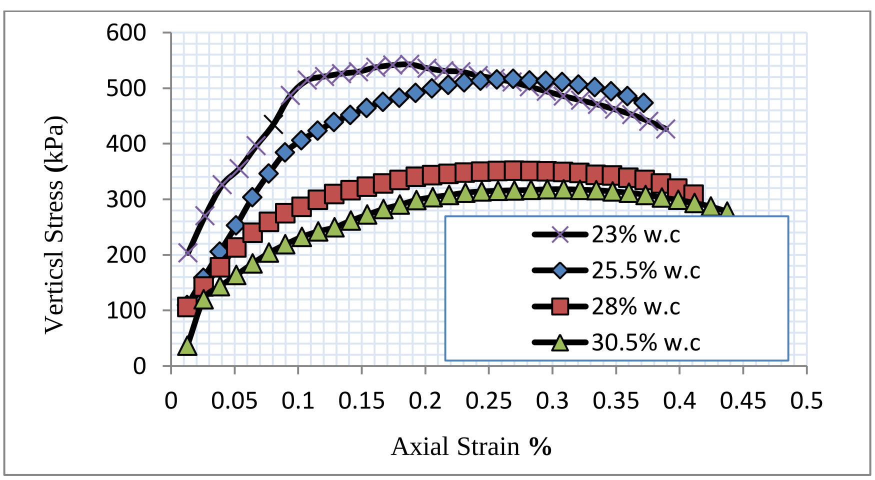

Figure 3. Unconfined compression test results of B-S mixture.

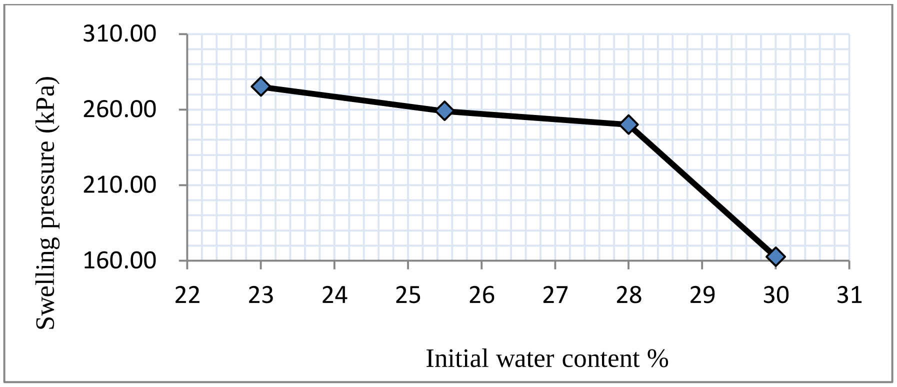

Figure 4. Initial water content versus swelling pressure of B-S mixture.

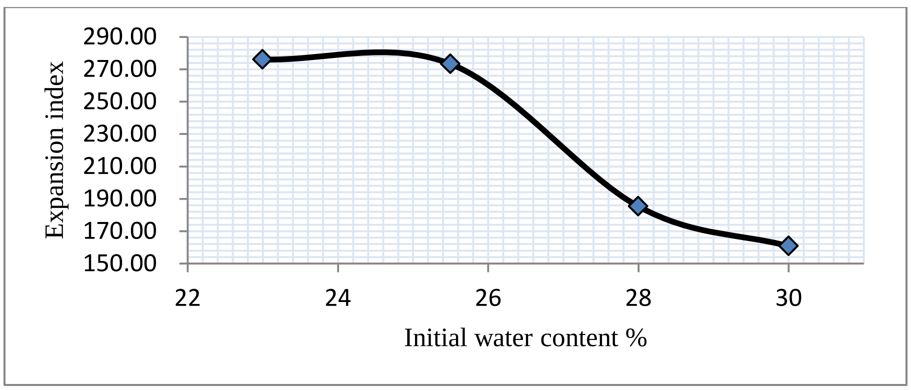

Figure 5. Initial water content versus expansion index.

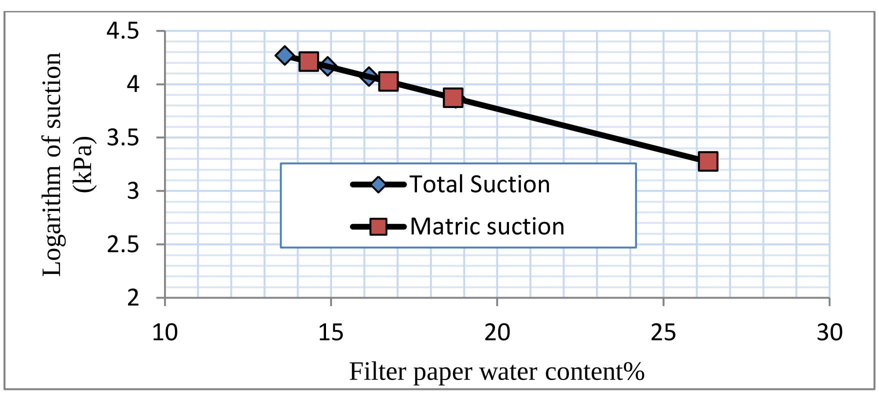

Figure 6. The relation of suction (total and matric) with the filter paper water content.

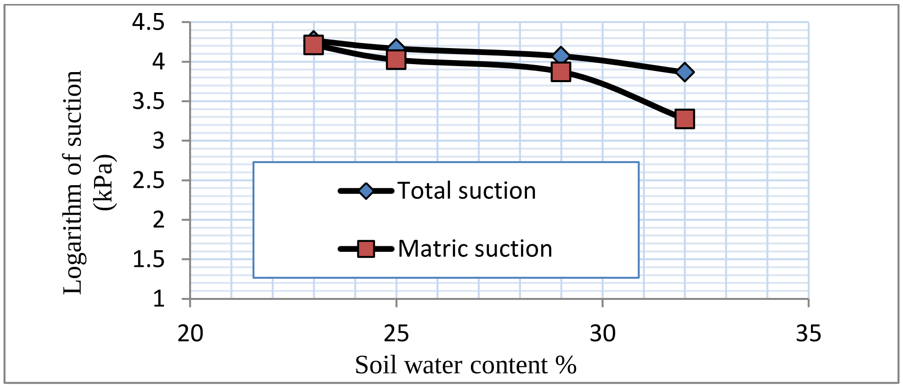

Figure 7. The relation of suction (total and matric) with the soil water content.

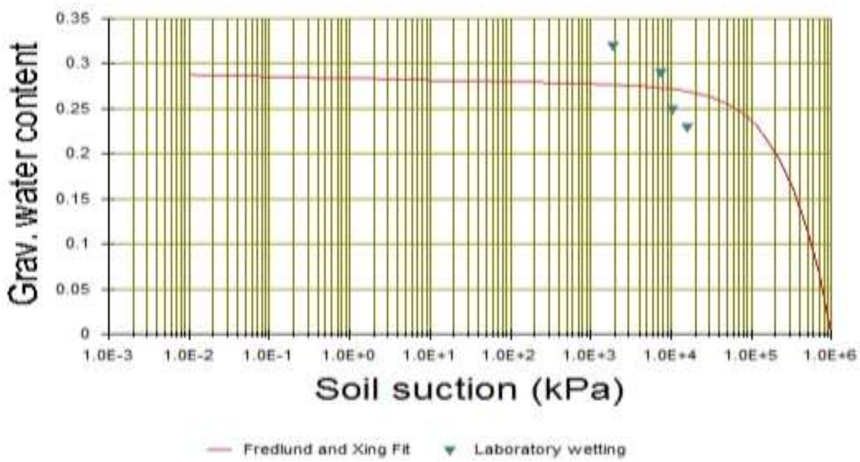

Figure 8. The SWRC estimated by Fredlund and Xing equation.

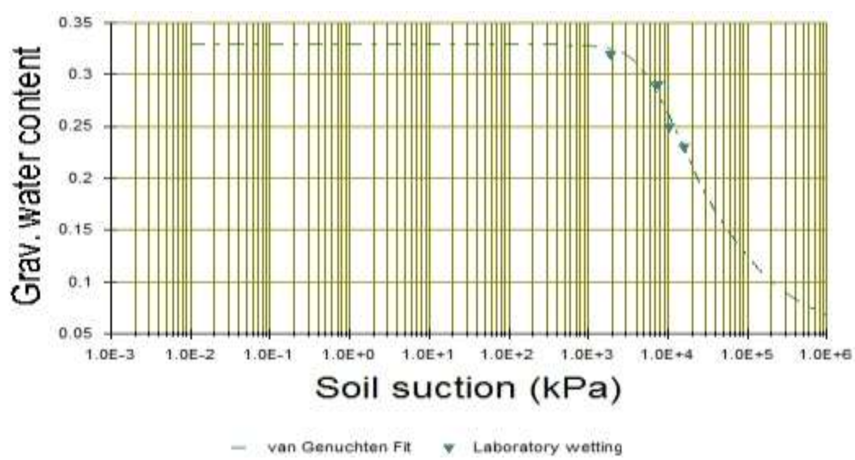

Figure 9. The SWRC estimated by Van-Genuchten equation.

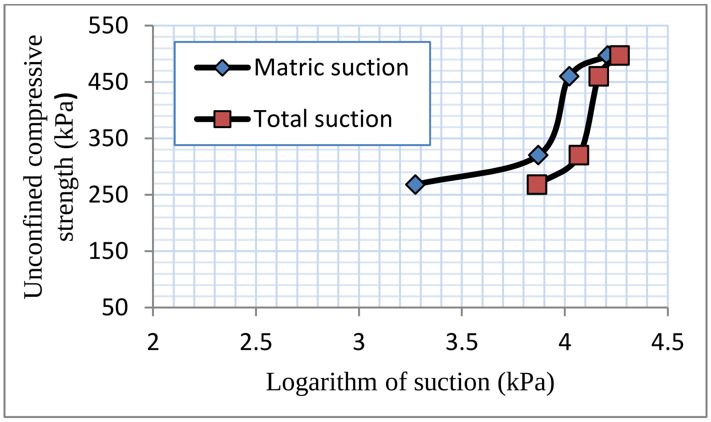

Figure 10. The relation between soil suction (matric and total) and the unconfined compressive strength.

Bearing Capacity of Bored Pile Model Constructed in Gypseous Soil

Asst. Prof. Bushra Suhale Al-Busoda
Department of Civil Engineering
College of Engineering
University of Baghdad
Email: albusoda@yahoo.com

Asst. Lect. Asmaa Hasan Al-Rubaye
Department of Civil Engineering
College of Engineering
University of Baghdad
Email: asmaa5azan@gmail.com

ABSTRACT

Gypseous soils are distributed in many regions in the world including Iraq, which cover more than (31%) of the surface area of the country. Existence of these soils, always with high gypsum content, caused difficult problems to the buildings and strategic projects due to dissolution and leaching of the gypsum caused by the action of water flow through soil mass. For the study, the gypseous soil was brought from Bahr Al-Najaf, Al-Najaf Governorate which is located in the middle of Iraq. The model pile was embedded in gypseous soil with 42% gypsum content. Compression axial model pile load tests have been carried out for model pile embedded in gypseous soil at initial degree of saturation of (7%) before and after soil saturation. Several criteria have been used to calculate the bearing capacity of the model bored pile through the results of the pile load tests. It was found that Shen's method gave almost an acceptable result for all model pile load tests. Large draw down in bearing capacity was observed when model pile has been loaded after it was subjected to soaking for (24) hours because of loss of cementing action of gypsum by wetting.

Key words: gypseous soil, bored pile, bearing capacity, soaking, …..etc.

قوة التحمل لنموذج ركيزة الحفر شيدت في تربة الجبسية

أ.م.د. بشرى سهيل البوسدة
قسم هندسة المدنية
جامعة بغداد

م.م. أسماء حسن الربيعي
قسم الهندسة المدنية
جامعة بغداد

الخلاصة

تتوزع التربة الجبسية في العديد من المناطق في العالم بما في ذلك العراق ، والتي تغطي اكثر من 31% من مساحة البلاد. ان وجود هذه التربة بمحتوى جبس عالي ، يتسبب بمشاكل مختلفة للمباني و المشاريع الاستراتيجية نتيجة انحلال الجبس الناجم عن تسرب المياه من خلال كتلة التربة . التربة الجبسية التي تم اعتمادها في هذا البحث أحضرت من منطقة بحر النجف في محافظة النجف. نفذة ركيزة الحفر في تربة جبسية بمحتوى جبس يقارب ال 42 ٪ وقد أجريت اختبارات حمل الأنضغاط المحوري للركيزة المدفونة في تربة جبسية بدرجة من التشبع الأولي(7 ٪) قبل وبعد تشبع التربة. في هذه الدراسة تم استخدام عدة معايير مختلفة لتقييم قدرة تحمل ركيزة الحفر من خلال استخدام نتائج التي حصلت من فحص الركيزة. وقد وجد أن طريقة شن كادت أن تعطي نتيجة مقبولة لجميع اختبارات الحمل لنموذج الركيزة المستخدمة في هذا البحث. هبوط كبير تم ملاحظته في قابلية تحمل الركائز عند تحميلها بعد تعرضها الى الغمر بالماء لمدة 24 ساعة وذلك نتيجة لذوبان مادة الجبس الذي يعمل مادة رابطة بين حبيبات التربة.

الكلمات الرئيسية : تربة جبسية, ركيزة حفر, قابلية تحمل, غمر,.....

1. INTRODUCTION

Gypseous soils are classified as one of the problematic soils due to their complex and unpredictable behavior. They exist in many parts of the world, concentrated mainly in arid and semi-arid regions, ,**Al- Saoudi, et al., 2013**. In Iraq, it has been reported that many major projects suffered from several problems related to construction on or by gypseous soils such as cracks, tilting, collapse and leaching the soil, **Mahdi, 2004**. For examples, the damage cases and collapse occurred in the soil under the foundations of the houses in AL-Thawrra Hai, 1969, in Mosul City, **Al-Busoda**, **1999**.

It is a well-known fact that gypseous soils exhibit high bearing capacity and very low compressibility when they are dry. The collapsibility of gypseous soils results from the direct contact of water.

In civil engineering, it can be defined that a soil is a "gypseous soil" when it has gypsum content enough to change the properties of this soil, **Seleam, 2006**.

Deep foundations usually consist of piles, which are structural units installed by driving or by in-situ construction method. Foundation on collapsible soil suffers from sudden settlement, which may contribute to serious damage due to inundation.

The basis of the "soil mechanics approach" to calculating the carrying capacity of piles is that the total resistance of the pile to compression loads is the sum of two components, namely skin friction and end resistance. A pile in which the skin frictional component predominates is known as a *Friction Pile*; while a pile bearing on rock or some other hard incompressible material is known as an *End-bearing Pile*. With end-bearing piles, care must be exercised to ensure that the hard, dense layer is adequate to support the load, **Tomlinson, 2004**.

Ghazali, et al., 1990, presented a case history about the design of pile foundations in calcareous and coral formations and pile load tests in Jeddah area on the eastern coast of the Red Sea. This case study presents two design approaches: precast concrete driven piles, and bored and grouted piles. According to the pile load tests of these two proposed pile types, bored and grouted cast in place concrete piles were found to be the most suitable type for coral formation and carbonate sediments of the east coast of the Red Sea. The researchers concluded that the driven pile causes the soil grains to crush rather than displace factually. It also causes a breakage in the structure and cementation of the coral rock, which results in low skin friction. The observed allowable settlements for driven precast concrete piles were high and exceeded the values stated in the specification even before reaching the working load.

Nabil, 2001, studied the behavior of bored pile groups in cemented sands by a field testing program at a site in South Surra, Kuwait. The program consisted of axial load tests on single bored piles in tension and compression. Two groups of piles, each consisting of five piles were tested. The soil deposit at the site consists of medium dense, weakly cemented sands with strength parameters of cohesion of 20 kPa and internal friction angle of 35degree. Test results on single piles indicated that the axial load distribution along the piles in compression was nearly linear. Also the single piles in compression resisted 70% of the applied load at failure in side friction and 30% in base resistance.

,Abd Elsamee, 2012, had conducted three in-situ pile load tests on bored piles of 900 mm diameter and 50 m length. Soil profile indicates that the soil type from elevation 0.00 to -10.00 m is calcareous silty- sand with broken shells, from elevation -49.00 to -52.00 m is calcareous silty- sand, and from elevation -52.00 to -60.00 m is hard silty-clay with intervening calcareous silty-sand. The ultimate capacities of the piles are determined from the load test results using different criteria. These criteria were Tangent Graphical method, Hansen method, Chin's method, Ahmed and Pise (1997), and Decourt's extrapolation method. The results of different criteria show that the percentage of friction load carried by the shaft is approximately 85% to 90% and the percentage of load carried by the end bearing is 15% to 10%. Hansen (1963) method gives higher values of ultimate capacity carried by the pile than the other methods.

2. SOIL PROPERTIES

2.1 Physical Properties

These tests include specific gravity, atterberg limits, grain size distribution, relative density, and permeability tests. The details of these tests are illustrated in **Table 1**. and **Fig. 1** which show the grain size distribution curves.

2.2 Engineering Tests

Engineering tests were conducted on gypsums soil. The initial degree of saturation for soil sample was 7%. The engineering tests comprise collapse test, one-dimensional compression test, and direct shear test. The results of these tests are given in **Table 2**. and **Figs. 2**, **3**, and **4**, respectively.

3. DETAILS OF MODEL PILE

Aluminum solid pile was used as pile prototype. The pile surface was rough, in order to insure the interaction between soil and pile due to the friction on pile-soil interface, and the angle of interface friction for this testing pile was obtained from a series of shear box tests.

Pile shape is shown in **Plate 1** and its properties are illustrated in **Table 3**.

4. MODEL LOADING SETUPS

The model setups are listed below:

- Test box with (450*600*600) mm in size
- Loading jack
- Axial loading system
  1) S-type load cell (500 kg) capacity
  2) Wagezelle type load cell (1000 kg) capacity, (tip load cell)
  3) Two Load Cells Indicators
  4) Two dial gauges (0.01 mm)
  5) Two magnetic holders

- Two steel plates, at the center of one side of each plate there is a hollow semi-circle with radius of (21mm)

5. SOIL BED PREPARATION FOR FLOATING PILE, (F-PILE)

Gypseous soil was prepared at initial degree of saturation equal to 7%. The model box has been divided in to 9 layers. Weight of soil was calculated depending on volume of each layer and dry in-place unit weight of soil (12.5 kN/m^3). Soil was mixed thoroughly with the required amount of water by hands till completing the whole quantity. After preparing the specimen, it was put in the model box using static loads. After making some trials, it was found that 32 Kg was enough to ensure that soil sample would fill the expected volume of one layer. For distributing static loads uniformly on the surface of the soil, two steel plates were used, as shown in **Plate 2**. The dimensions of each plate were (582*296*2) mm and at the center of one side a hollow semi-circle with radius (21) mm slightly larger than the radius of the pile was made. The plates for one layer were put in X-direction and for the next layer in Y-direction to prevent making weak joint.

6. INSTALLATION OF MODEL PILES

For model pile which has been embedded in homogeneous gypseous soil, it was decided to determine the values (percentages) of mobilized skin friction and base resistance under compression pile load test. Therefore the floating model pile was used. To install the model floating pile, steel plate of (1mm) thickness and one hole (21mm) in diameter was placed at center of plate. The plate with a hole was welded to a cylindrical steel tube of (3cm) length which works as a casing for pile to keep the model pile vertically in the box and prevent horizontal movement, see **Plate 3**.

7. TEST PROCEDURE FOR MODEL LOADING TEST

In loading stages, to decide the amount of loads that will be exerted on the model piles, theoretical static equation is used. The working load of pile is calculated by dividing the predicted ultimate pile capacity by a factor of safety equal to (2.5). The procedure recommended by the American Standard ,**ASTM D,1143.** was followed during the model pile load test. Model pile was loaded to 250% of the working load with increments; each one was equal to 25% of working load.

The loading process was performed using manual hydraulic jack provided with load cell (S-type) to record the axial load exerted on the model pile and tip load cell for recording pile tip resistance, see **Plate 4**.

The following model tests were conducted for rough prototype pile:

1) Axial pile load test was carried out when the initial degree of saturation was 7%. **Fig. 5** shows pile load-settlement curve.
1. Pile model test was soaked for 24 hours before pile loading test, axial (compression) load was exerted on model pile after 24 hours from inundation, when the initial condition was (S= 7%), the shape of pile load-settlement curve is presented in **Fig. 6**.

The pile settlement was measured by dial gauge of (0.01) mm, while soil settlement was measured at a distance of (50 mm) from the side of pile by dial gauge (0.01) mm. For connecting the dial gauges on the model box, two magnetic holders were used. **Plate 5** shows the arrangements of dial gauges for soil and pile settlement readings.

8. CALCULATING THE RESISTANCE OF PILE TO COMPRESSIVE LOAD

Design of a pile foundation for axial load starts with an analysis of how the load is transferred to the soil, often thought limited to determining only the pile capacity, sometimes separating the capacity on components of shaft and toe resistances. The load-transfer analysis is often called static analysis or capacity analysis, **Fellenius, 2006.**

The ultimate bearing capacity for ($\boldsymbol{c}$) and ($\boldsymbol{\phi}$) soil can be determined by the static formula as follows:

$$Qu = Qb + Qs \quad (1)$$

$$Qu = A_P\left[cN_C + \sigma_{vb}\, N_q\right] + \sum A_S\, (c\alpha + K_S\sigma_v\, tan\, \delta) \quad (2)$$

Value of ($\boldsymbol{K}$) depends on several factors, for bored pile is equal to coefficient of lateral earth pressure at rest condition (K_o) and calculated from equation 3.

$$K_o = 1 - \sin\phi \quad (3)$$

The (α) value lies in the range of 0.3 to 0.6 for bored pile, **Malone, 1996**. The (α) value elected in above equations was (0.45).

9. PREDICTION OF THE ULTIMATE PILE CAPACITY

It is difficult to define the failure load of pile when it has not been loaded to failure. There are a number of criteria used to determine the bearing capacity of piles from pile load test, the criteria used included:

1. *Tangent Graphical Method*: defines the failure as the load at the intersection of the initial straight portion of the curve and final straight portion of the curve.
2. *Terzaghi Method*: when the pile settlement is equal to 10% of pile diameter.
3. *Log load-Log settlement*: This method is used for long pile length with large-diameter by plotting a logarithmic relationship between the value of the (settlement / Diameter) and the load. The maximum load is determined by depending on the diameter of the pile, where the *ASTM*322 identifies the maximum value when (settlement / diameter) is 0.05, **Fattah,** and **Al-Shakarchi, 2009**.
4. *Chin-Kondner Extrapolation*: according to Chin's method the tests carried out with piles in field and in laboratory show that, load-settlement relation is hyperbolic. A plot is made between settlement divided by corresponding load and the settlement. After some initial

variation, the plotted values fall on a straight line. The inverse slope of this line gives the ultimate load, **Fattah** and **,Al-Shakarchi, 2009**.

$$\delta_1/_P = m\delta_1 + c_2 \tag{4}$$

5. *Brinch Hansen Method (1963)*: the square root of each settlement value from pile load test data divided by corresponding load value is plotted against the settlement. **Fattah** and **Al-Shakarchi, 2009 and Dewaikar, 2012**.

Ultimate load is given as:

$$Qu = 1/_{2\sqrt{c_1 * c_2}} \tag{5}$$

6. *Decourt's Extrapolation (1999)*: divided each load with its corresponding settlement and plot the resulting value against the applied load. A linear regression over the apparent line (often be the last points) determine the line. Decourt identified the ultimate load as intersection of this line with load axis, **Fattah,** and **Al-Shakarchi, 2009 and Dewaikar, 2012**.
7. *De Beer Method*: by plotting the load-settlement data in a double-logarithmic form. The intersection point of two straight lines on a log-log plot gives the magnitude of ultimate load, **Fattah and ,Al-Shakarchi, 2009**.
8. *Shen's Method (1980)*: load-settlement curve is drawn with settlement vs log load coordinates and a curve with linear tail is obtained. Starting point of linear tail is defined as the ultimate load, **Dewaikar, 2012**.

10. ULTIMATE BEARING CAPACITY TERMS FOR FLOATING PILE

Through the study, which was conducted on a floating pile embedded in gypseous soil, and also conclusions of former researchers as ,**Fattah et al., 2009** and **Abd Elsamee, 2012**. Shen's method was used for selecting the values of ultimate bearing capacity. It was seen that this method gave almost acceptable results for model pile load tests. **Table 5.** clarifies the skin friction and base resistance obtained from results of model bored pile load tests, which have been tested at initial degree of saturation at soaked and un-soaked states. It also shows the percent of reduction (**RD** %) in $\boldsymbol{Qu}$ due to soaking, where:

$$RD = \frac{Qu_{un-soaked} - Qu_{soaked}}{Qu_{un-soaked}} \times 100 \tag{6}$$

11. RESULTS FOR PHYSICAL TESTS

The particle size distribution tests conducted using dry and wet sieve analyses method. The data on soil reflects a significant difference between the dry and wet sieving by water, with respect to soil with gypsum content equal to (42%) the dry sieving showed only (6.4%) fines while the wet sieving resulted in (44%) fines. The ability of gypsum for dissolution leads to an erroneous determination of particle size distribution by wet sieving (using water). As shown in **Fig. 1** there is no difference observed between the curve of dry sieving and the curve of wet sieving of samples soaked in kerosene.

Hydrometer test was carried out by using water saturated with gypsum for avoiding dissolution of gypseous soil in water saturated with gypsum. The percentage of passing sieve No. 200 from wet sieving by kerosene is (9.3%), which is between (5-12) percent. The gypseous soil is classified as (SP-SM) according to the Unified Soil Classification System.

The specific gravity decreases for the soil with high gypsum content. The low specific gravity of gypseous soil is attributed to low specific gravity of gypsum, which is equal to (2.32).

Atterberg limits play an important role in classification of cohesive soils, which affect the magnitude of many properties such as compressibility and strength. Liquid limit results were obtained by cone pentrometer method. The results of tests are shown in **Table 1**.

From the results of field and minimum and maximum unit weights of gypseous soil, the relative density of gypseous soil is (35%), thus soil has a loose state.

The coefficient of permeability (k) was determined by the constant head method from three differents times. The coefficient of permeability was determined over a short period after the confirmation that the amount of water flow was constant. The results obtained of permeability test are shown in **Table 1**. According to the results obtained, the soil may be classified as "low permeability soil", as stated by ,**Lambe,** and **Whiteman, 1969**.

12. RESULTS FOR ENGINEERING TESTS

The severity of collapse problem has been classified according to the classification suggested by ,**Jennings** and **Knight, 1975**. It is found to be problem. The addition of water leads to break bonds between soil particles and results in settlement of soil sample.

For the one-dimensional compression test, the unloading portion of the curve showed a little rebound after the release of the load since the deformation was primarily due to rearrangement of the grains and softening of gypsum.

For the direct shear test, in soaked state the reduction in value of cohesion is due to loss of cementing action of gypsum by wetting. Similar results were found by ,**Al-Dulaimi, 2004** and ,**Hussein, 2012**. while the angle of internal friction is less influenced by the soaking process.

13. RESULTS FOR PILE LOAD TEST

In soaked state, before pile load test, the soil was subjected to soaking from top surface. From the results of the dial gauge readings of pile and soil settlements it is found that the soil settlement is more than the pile settlement. **Fig. 7** shows the variation of pile settlement and soil settlement within 24 hours of soaking. When pile was loaded at soaked state, large draw down in bearing capacity was observed and trend of behavior is similar to that of local shear failure. This behaviour may be attributed to the breaking of bonds due to soaking. The soil exhibited a loss in strength parameters because of loss of cementing action of gypsum by wetting.

The values of the ultimate bearing capacity which are obtained from pile load-settlement curves according to different criteria, and the theoretical calculations are summarized in **Table 4**. From the results obtained, it was found that some criteria like Chin-Konder extrapolation, Brinch Hansen 1963, and Decourt give high estimation of the bearing capacity for model pile load tests. It is thought that these methods are not suitable for bored pile of large diameter, the same result was observed by ,**Fattah** and **Al-Shakarchi, 2009,** for bored pile constructed in Baghdad city, and **,Abd Elsamee, 2012**, for pile load tests on bored piles constructed in soil contained calcareous silty- sand**.** Log load-Log settlement, Terzaghi, and Tangent Graphical Method were given lower value than the other criteria for evaluation of the bearing capacity of floating piles in soaked condition.

14. CONCLUSIONS

Based on the experimental results of the experimental work, the following conclusions may be obtained:

1) From the different criteria that were used for evaluation of the ultimate bearing capacity, Log load-Log settlement, , and Tangent Graphical Method were given lower value than the other criteria, while Chin-Konder extrapolation method, Brinch Hansen (1963), and Decourt extrapolation gave high estimation of the bearing capacity in model pile load tests. Shen's method gave almost the acceptable results for model pile load tests.
2) Large draw down in bearing capacity was observed when floating pile was loaded after it was subjected to soaking for (24 hours). The percent of reduction (**RD**, %) in Q_u due to soaking was 45%.
3) When the model box was soaked with water, the gypseous soil was affected and collapsed; the final settlement of gypseous soil (11.02, mm) was more than the final settlement of pile (9.18, mm).

REFERENCES

- Al-Aqaby, M.D., 2004. *Effect of Kerosen on Propertiese of a Gypseous Soil,* M.Sc. Thesis, Civil Engineering Department, University of Baghdad.

- Al-Busoda, B.S.Z., 1999, *Studies on the Behavior of Gypseous Soil and its Treatment during Loading,* M.Sc. Thesis, Civil Engineering Department, University of Baghdad.

- Al-Dulaimi, N.S., 2004, *Characteristics of Gypseous Soils Treated with Calicum Chloride Solution,* M.Sc. Thesis, Civil Engineering Department, University of Baghdad.

- Al-Saoudi, N.K.S., Al-Khafaji, A.N., Al-Mosawi, M.J., 2013, *Challenging Problems of Gypseous Soils in Iraq*, Proceedings of the 18^{th} International Conference on Soil Mechanics and Geotechnical Engineering, Paris.

- ASTM D1143-81, 1994, *Standard Test Method for Piles under Static Axial Compressive Load.*
- ASTM D1556-07, 2007, *Standard Test Method for Density and Unit Weight of Soil in Place by the Sand-Cone Method.*

- ASTM D2216-98, 1999, *Standard Test Method for Laboratory Determination of Water (Moisture) Content of Soil and Rock by Mass.*

- ASTM D2434-68, 2000, *Standard Test Method for Permeability of Granular Soils (Constant Head).*

- ASTM D2435-00, 1996, *Standard Test Method for One-Dimensional Consolidation Properties of Soils.*

- ASTM D2487-00, 2000, *Standard Practice for Classification of Soils for Engineering Purposes (Unified Soil Classification System).*

- ASTM D3080, 1989, *Standard Test Method for Direct Shear Test of Soils under Consolidated Drained Conditions.*

- ASTM D422-02, 2000, *Test Method for Particle-Size Analysis of Soils.*

- ASTM D422-63, 1998, *Standard Test Method for Particle-Size Analysis of Soils.*

- ASTM D4254-00, 2000, *Standard Test Methods for Minimum Index Density and Unit Weight of Soils and Calculation of Relative Density.*

- ASTM D5333–92, 1993, *Standard Test Method for Measurement of Collapse Potential of Soils.*

- ASTM D854-00, 2000, *Specific Gravity of Soil Solids by Water Pycnometer.*

- British Standard Institution, 1975, *Methods of Testing Soil for Civil Engineering Purposes*, B. S. 1377.
- Dewaikar, D.M., 2012, *Analysis of Pile Load Tests Data*, Asian Journal.

- Abd Elsamee, W.N., 2012, *Evaluation of the Ultimate Capacity of Friction Piles,* Engineering Sciences, Vol.4, No.11, PP.778-789.

- Fattah, M.Y., Al-Shakarchi, Y.J., 2009, *A Comparision Between Diferent Criteria in Evaluating the Bearing Capacity of a Bored Pile in Baghdad City,* The 6th Engineering Conference,Civil Engineering, University of Baghdad, Vol.1.

- Fellenius, B.H., 2006, *Basics of Foundation Design,* Electronic Edition.

- Ghazali, F.M., Baghdadi, Z.A., and Mansur, O.A., 1990, *A Comparative Study of Pile Foundations in Coral Formations and Calcareous Sediments*, Engineering Sciences, Vol.2, No.1, PP.3-17.

- Hussein, R.S., 2012, *Bearing Capacity of Shallow Footing on Compacted Dune Sand Over Reinforced Gypseous Soil*, M.Sc. Thesis, Civil Engineering Department, University of Baghdad.

- Jennings, J. E., and Knight, K., 1975, *A Guide to Construction on or with Materials Exhibiting Additional Settlement Due to 'Collapse' of Grain Structure, Proceedings,* Sixth Regional Conference for Africa on Soil Mechanics and foundation Engineering Johannesburg, South Africa, PP.99-105.

- Lambe, T.w., and Whiteman, R. V., 1969, *Soils Mechanics, John Wiley and Sons Inc.,* New York.

- Mahdi, B.O., 2004, *Some Engineering Aspects of Gypseous Soils,* Ph.D. Thesis, Civil Engineering Department, University of Baghdad.

- Malone, A.W., 1996, *Foundation Design and Construction, Geotechnical Engineering Office, Civil Engineering and Development Department,* the Government of the Hong Kong, Geo Publication No.1, Via the Internet.

- Nabil, F.I., 2001, *Axial Load Tests on Bored Piles and Groups in Cemented Sands,* Journal of Geotechnical and Geoenvironmental Engineering, Vol. 127, No. 9, PP. 766-773.

- Seleam, S.N., 2006, *Evaluation of Collapsibility of Gypseous Soils in Iraq*, Journal of Engineering, Vol. 13, No. 3, PP. 712-726.

- Tomlinson, M.J., 2004*, Pile Design and Construction Practice,* Fourth Edition.

- Varghese, P.C., 2009, *Foundation Engineering,* Sixth Edition.

NOMENCLATURE

A_P = cross-sectional area of pile, m^2
A_S = surface area of pile shaft, m
c = soil cohesion, kPa
C_1 = slope of the best fitting straight line, dimensionless
C_2 = y-intercept of straight line for best fittnig
Cc = compression index, dimensionless
CP = collapse potential, %
Cr = rebound index, dimensionless
Dr = relative density of soil, %
Gs = specific gravity, dimensionless
K = coefficient of permeability, cm/sec
K_o = coefficient of earth pressure at rest condition, dimensionless
K_S = coefficient of earth pressure, dimensionless
L = length of pile penetrating settling soil, m
L/D pile = length-to-diameter ratio, dimensionless
L.L = liquid limit, %
m = slope of straight line, dimensionless
N_C , N_q = bearing capacity factors, dimensionless
P = load, kN

P.I = plasticity index, %
P.L = plastic limit, %
Qb = end-bearing resistance, Kg
Qs = skin friction resistance, Kg
Qu = ultimate bearing capacity, Kg
RD = percent reduction in ultimate bearing capacity, %
S = degree of saturation, %
α = adhesion factor, dimensionless
γ_d = in-place dry unit weight, kN/m^3
γ_{dmax} = maximum value of dry unit weight, kN/m^3
γ_{dmin} = minimum value of dry unit weight, kN/m^3
δ = interface friction angle, deg.
δ_1 = pile settlement, mm
σ_v = effective overburden pressure, kPa
σ_{vb} = effective overburden pressure for base soil, kPa
ϕ = internal friction angle, deg.

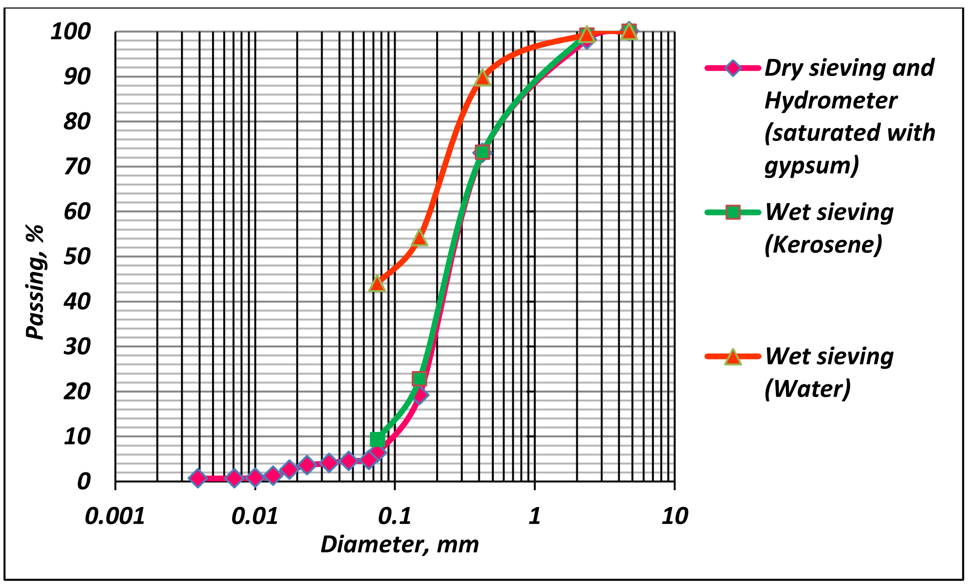

Figure 1. Grain size distribution curves of gypseous soil.

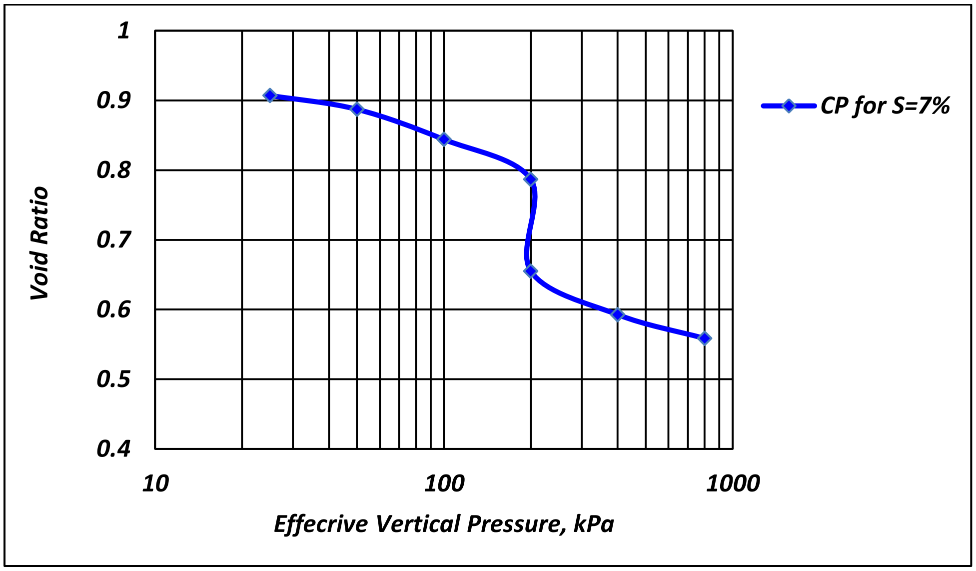

Figure 2. Result of single collapse test for gypseous soil.

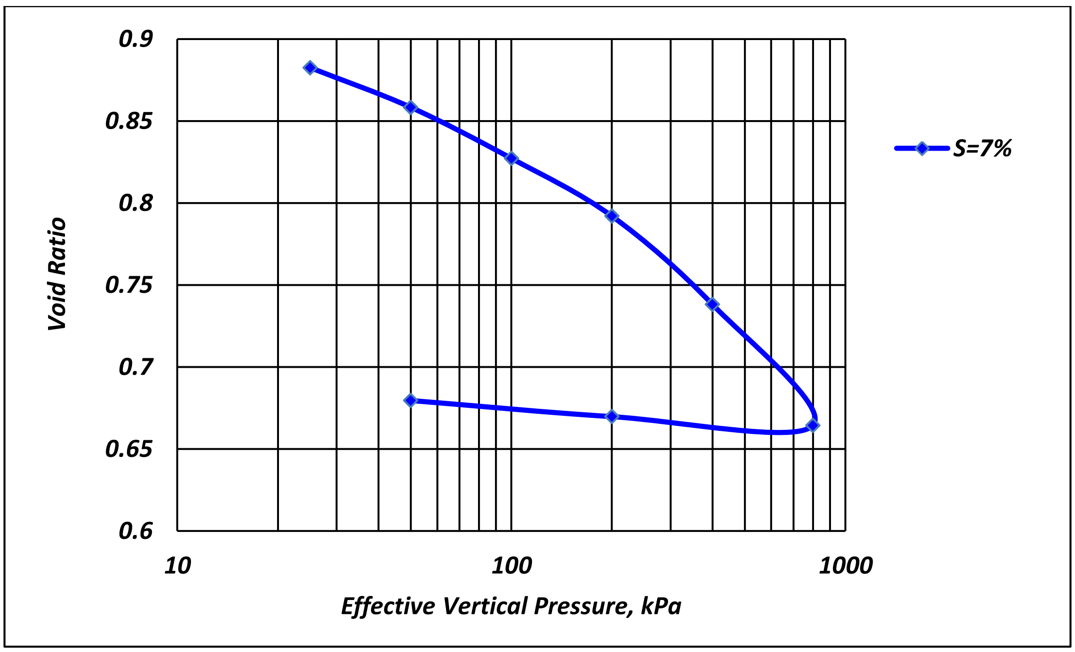

Figure 3. One-dimensional compression curves for gypseous soil.

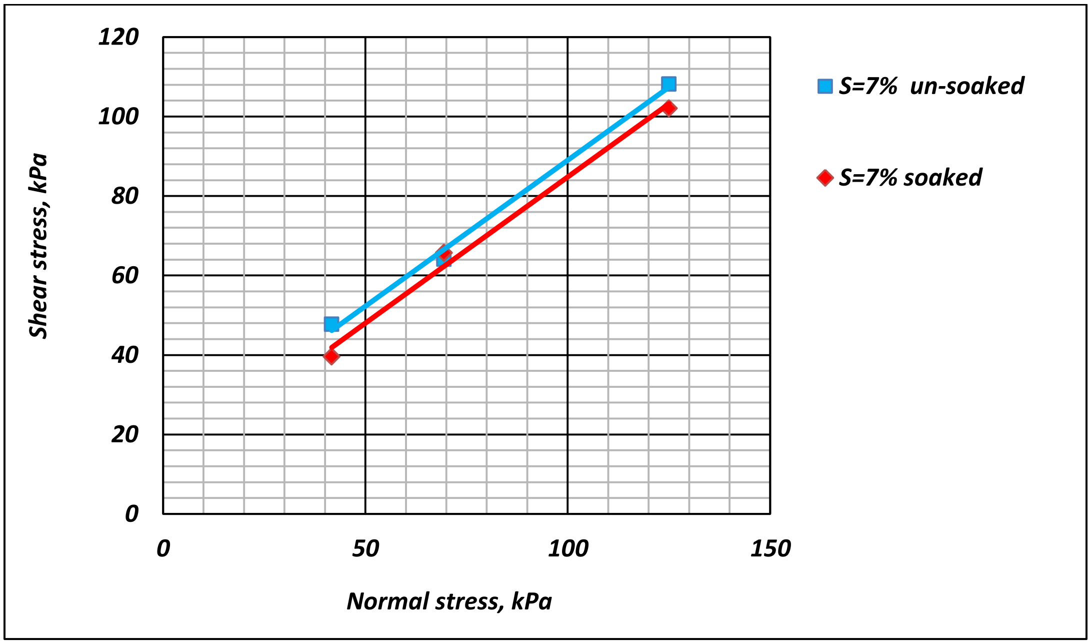

Figure 4. Shear stress –normal stress relationship for gypseous soil at 7% degree of saturation for soaked and un-soaked states.

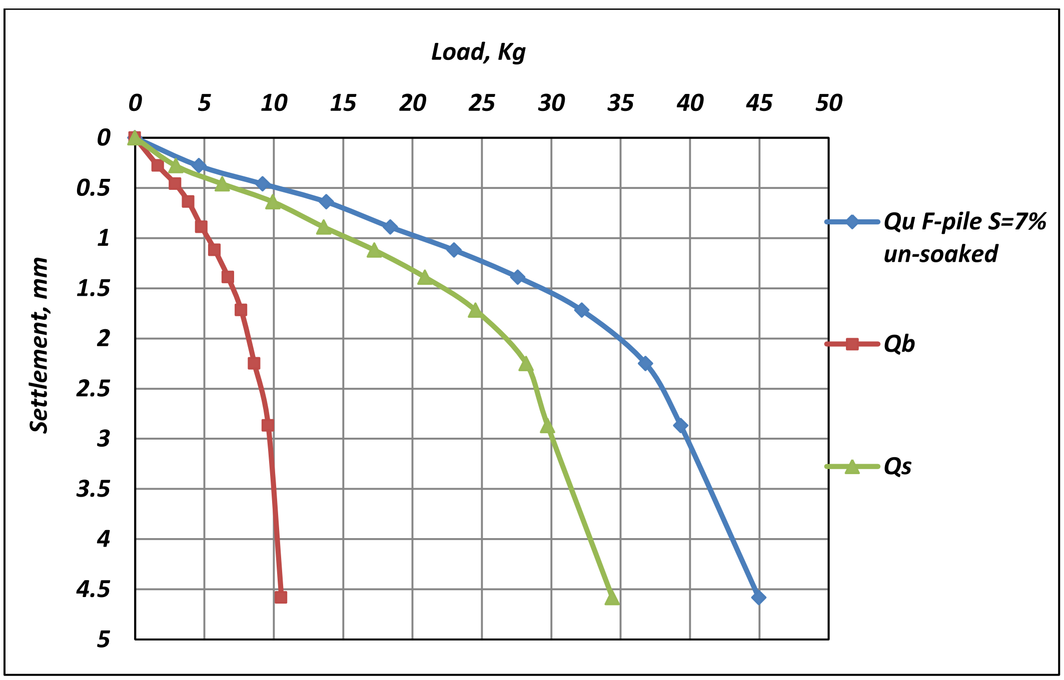

Figure 5. Load-settlement curves for floating pile with 7% degree of saturation in un-soaked state.

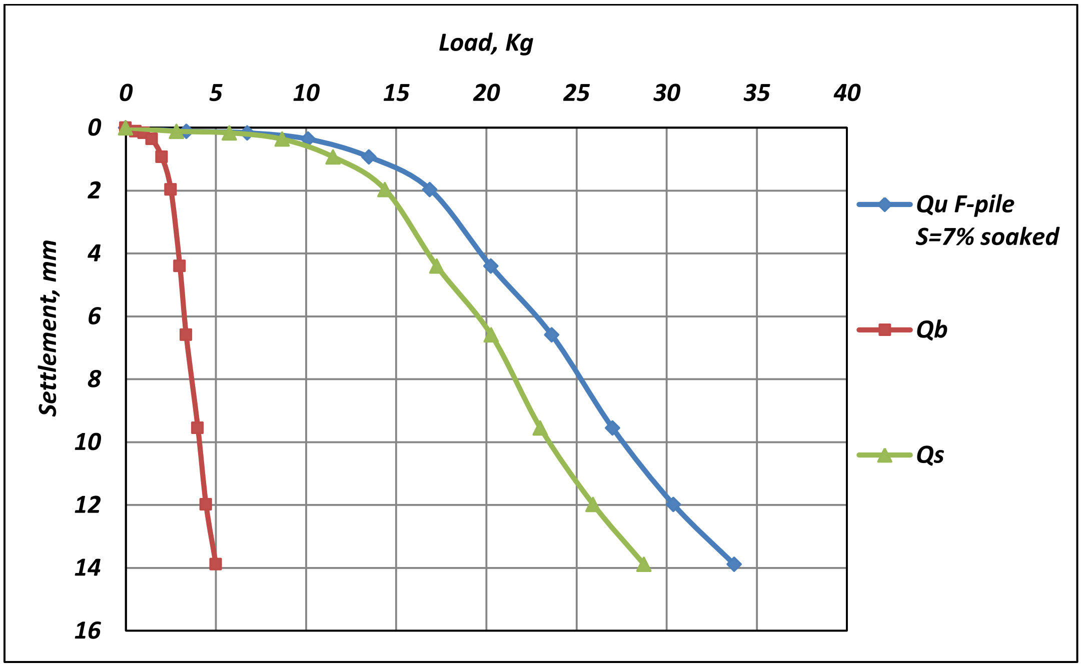

Figure 6. Load-settlement curves for floating pile with 7% degree of saturation in soaked state.

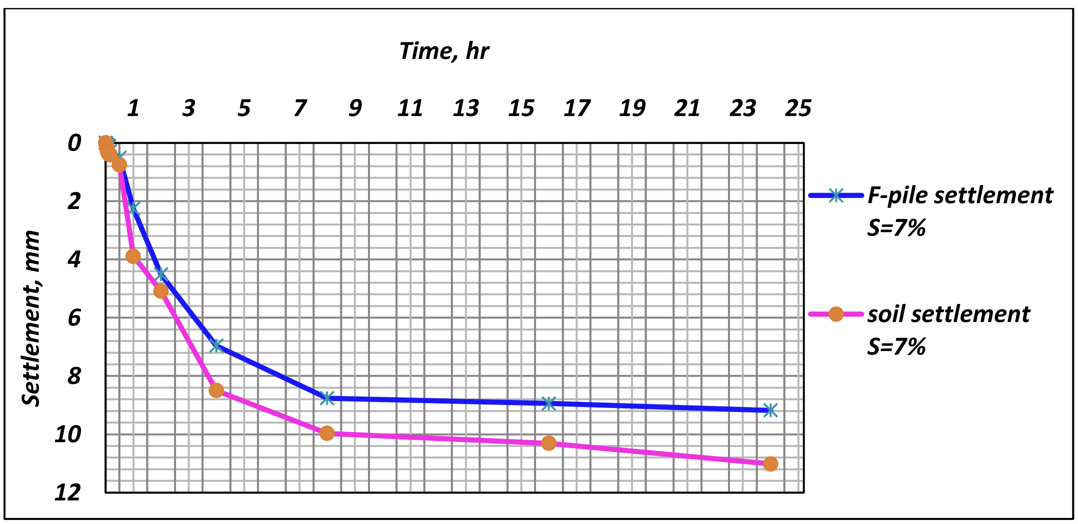

Figure 7. Variation of pile and soil settlements during soaking before loading the floating pile.

Plate 1. Shape of pile model test.

Plate 2. Static Loads for placing gypseous soil.

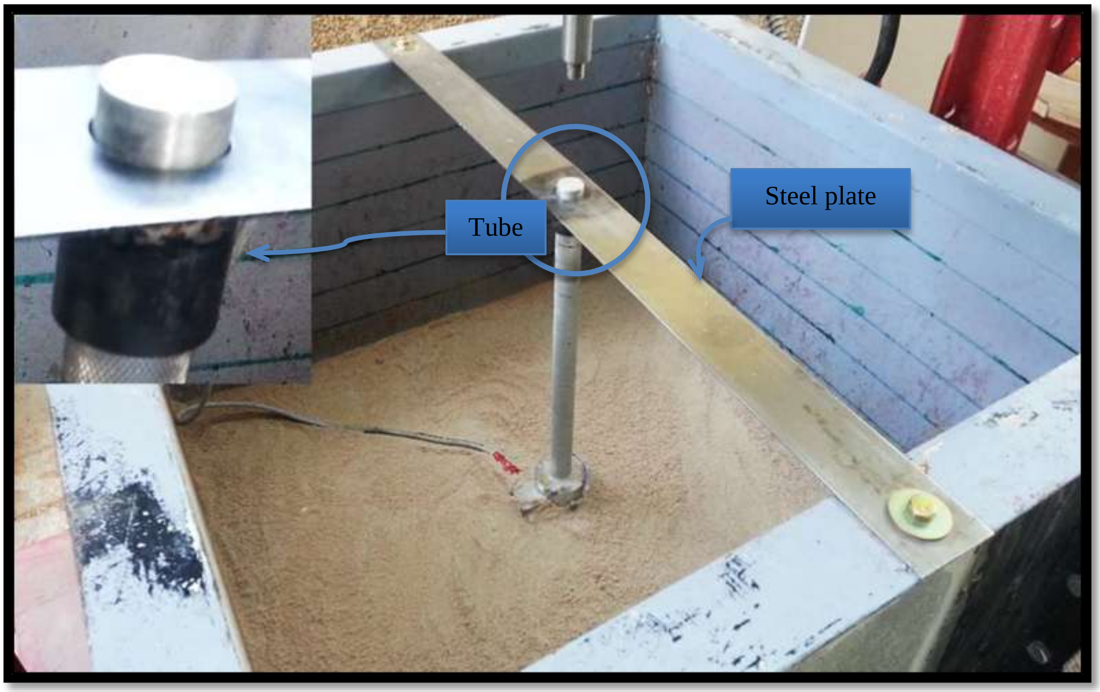

Plate 3. Steel plate fixed the model pile vertically in the box and prevented horizontal movement.

Plate 4. Load cells and their indicators.

Plate 5. Arrangements of dial gauges for soil and pile settlements readings.

Table 1. Results of physical tests for gypseous soil.

Properties		Value
Specific gravity, (*Gs*)		2.48
Atterberg's limits	Liquid limit (*L.L*)%	33
	Plastic limit (*P.L*)%	N.P
	Plasticity index (*P.I*)%	---
Minimum dry density, (γ_{min}) kN/m³		11.50
Maximum dry density, (γ_{max}) kN/m³		14.88
Dry field density, (γ_d) kN/m³		12.50
Relative density, (*Dr*) %		35
Permeability, (*K*) cm/sec		$2.11*10^{-4}$

Table 2. Results of engineering tests.

Properties		**value**
Collapse potential, CP%		7
Cc		0.166
Cr		0.0125
un-soaked	C, kPa	15.5
	ϕ, deg.	36
soaked	C, kPa	11
	ϕ, deg.	36

Table 3. Properties of pile model.

Properties	**Value**
Weight of pile	280 gm
Density of pile	2.78 gm/cm^3
Length of pile (L)	30 cm
Diameter of pile (D)	2 cm
L/D ratio	15

Table 4. Summary of ultimate capacity (kg) for bored floating piles constructed in gypseous soil at soaked and un-soaked states.

Predicted pile load capaciy (Kg)	CP =7% S = 7%	
	Unsoaked	**Soaked**
Theoretical (static method)	45.5	31.6
Tangent graphical method	33	15
Terzaghi method	36	17
Log load-log settlement	20	15
Chin-kondner extrapolation	60.97	38.3
Brinch hansen method (1963)	54.6	33.2
Decourt's extrapolation	58	26
De beer method	36.8	20.25
Shen's Method (1980)	36.8	20.25

Table 5. Skin friction and base resistance values for floating bored piles.

Un-soaked State					Soaked State					RD%
Qu, Kg	*Qb, Kg*	*Qs, Kg*	*Qs, %*	*Qb, %*	*Qu, Kg*	*Qb, Kg*	*Qs, Kg*	*Qs, %*	*Qb, %*	
36.8	8.6	28.2	77	23	20.25	3	17.25	85	15	45

Treatment of Furfural Wastewater by (AOPs) Photo-Fenton Method

Dr. Yasmen A. Mustafa
College of Engineering-University of Baghdad
Email:yasmen.mustafa@gmail.com

Raid Raho Omran
College of Engineering-University of Baghdad
Email:raid_omran@yahoo.com

ABSTRACT

The objective of this study is to investigate the application of advanced oxidation processes (AOPs) in the treatment of wastewater contaminated with furfural. The AOPs investigated is the homogeneous photo-Fenton ($UV/H_2O_2/Fe^{+2}$) process. The experiments were conducted by using cylindrical stainless steel batch photo-reactor. The influence of different variables: initial concentration of H_2O_2 (300-1300mg/L), Fe^{+2}(20-70mg/L), pH(2-7) and initial concentration of furfural (50-300 mg/L) and their relationship with the mineralization efficiency were studied.

Complete mineralization for the system $UV/H_2O_2/Fe^{+2}$ was achieved at: initial H_2O_2 = 1300mg/L, Fe^{+2} = 30mg/L, pH=3, temperature =30^{o}C and irradiation time of 60 min, for 300mg/L furfural concentration. The results have shown that the oxidation reagent H_2O_2 plays a very important role in the furfural mineralization.

Key words: Advanced oxidation process, UV, Furfural, Photo-Fenton process, H_2O_2.

معالجة المياه الملوثة بالفورفورال باستخدام عمليات الاكسدة المتقدمة(طريقة الفوتوفنتون)

ياسمين عبد العزيز مصطفى
استاذ مساعد دكتور
كلية الهندسة – جامعة بغداد

رائد رهو عمران
باحث
كلية الهندسة – جامعة بغداد

الخلاصة

الهدف من هذا البحث دراسة معالجة المياه الملوثة بمادة الفورفورال باستخدام احد طرق الاكسدة المتقدمة (AOPs). حيث تم استخدام نظام الاكسدة المتجانسة ($UV/H_2O_2/Fe^{+2}$, photo-Fenton process). التجارب تم اجرائها باستخدام مفاعل اسطواني مصنوع من الفولاذ المقاوم للصدأ يعمل بنظام الوجبات. تاثيرالمتغيرات المختلفة مثل: التركيز الابتدائي لل H_2O_2 (300- 1300mg/L) و Fe^{+2}(20-70mg/L) و pH (2-7) والتركيز الابتدائي للفورفورال(50-300 mg/L) تم دراستها ودراسة علاقتها مع كفاءة التحلل للفورفورال. بينت التجارب ان التحلل الكامل للفورفورال بتركيزmg/L 300 تم باستخدام H_2O_2=1300mg/L و Fe^{+2} =30mg/L وبظروف حامضية pH=3 ودرجة حرارة 30^{o}C وبوقت 60 دقيقة . النتائج بينت ان تركيز العامل المؤكسد H_2O_2 له دور مهم في عملية الاكسدة.

1. INTRODUCTION

Many industries such as petroleum refining, petrochemical, pharmaceutical, pulp, paper and food industries involve processes that use or produce furfural, **Sahu, et al., 2008**. The discharge of untreated furfural wastewater can cause severe environment pollution. Therefore, there has been a growing interest for the removal of furfural from wastewater not only to counter its health effects but also to recover the furfural and recycle it back to the process. Most of the furfural on the world market is produced in China, **Win, 2005**. China is the dominant player in the world furfural market with 80% of global capacity and 72% of world consumption **Fig. 1**, **IHS, 2011**.

Furfural is irritating to eyes, skin and respiratory system. Inhalation may cause headache, nausea and central nervous system depression. It also may be absorbed through intact skin. It shows some limited carcinogenic effects, furfural has been classified as a category 3 carcinogen, **USEPA 2012.** Furfural actuate exposure can also damage livers and kidneys. The Permissible Exposure Limit (PEL) and the threshold limit value (TLV) for furfural was reported 5.0μg/ml and 2.0μg/ml, respectively, **ACGIH, 1994; OSHA, 1994**.

The presence of furfural, increase the toxicity of wastewater and makes biological treatment very difficult. Removal of this substance will require modifications or alternatives of the existing systems, **Yaghmaei et al., 2005**. This compound if discharge in open rivers, it can destroy the micro flora and has negative effect on human health.

Aerobic and anaerobic biological treatment have been used by many researchers for the degradation of furfural, **Wang, et al., 1994**. Also Adsorption technique is quite popular in the treatment of wastewater contaminated with furfural due to its simplicity as well as the availability of a wide range of adsorbents. Activated carbons are widely used as adsorbents for the treatment of furfural polluted water, **Sulaymon and Ahmed, 2006**.

Advanced oxidation processes (AOPs) are related to a nonconventional technologies that characterized by the generation of hydroxyl radicals, which are highly reactive and non-selective substances used to degrade toxic organic compounds present in a medium such as wastewater and soil. Some characteristics features of hydroxyl radical are shown in **Fig. 2**, **Oppenländer, 2007**. The hydroxyl radical has a high oxidation potential (E^0 = 2.8 V), as shown in **Table 1**, and is able to react with practically all classes of organic compounds, resulting in complete mineralization of these compounds, that is, the formation of carbon dioxide, water and inorganic salts, or their conversion into less aggressive products, **Bolton et al., 2001**.

Over a century ago, Fenton **,Fenton, 1894,** demonstrated that a mixture of H_2O_2 and Fe^{+2} in acidic medium had very powerful oxidizing properties. The classical mechanism is a simple redox reaction in which Fe^{+2} is oxidized to Fe^{+3} and H_2O_2 is reduced to hydroxide ion and the hydroxyl radical, Eq.(1) :

$$Fe^{2+}_{aq} + H_2O_2 \rightarrow Fe^{3+}_{aq} + HO^{\bullet} + OH^{-} \quad (1)$$

In the conventional Fenton reaction, carried out in the absence of light, the ferric ion produced in Eq.(1) can be reduced back to ferrous ion by a second molecule of hydrogen peroxide forming the hydroperoxyl radical, according to Eq.(2). This reaction, referred to by **Neyens and Baeyens, 2003** as Fenton-like, occurs more slowly than reaction (1)

$$Fe^{3+}_{aq} + H_2O_2 + H_2O \rightarrow Fe^{2+}_{aq} + H_3O^{+} + HO_2^{\bullet -} \quad (2)$$

About two decades ago, it was found that the irradiation of Fenton reaction systems with UV light strongly accelerated the rate of degradation of a variety of pollutants, **Pignatello et al., 2006 and Malato et al., 2003**. This behavior upon irradiation is due principally to the photochemical reduction of Fe^{+3} back to Fe^{+2}, for which the net reaction can be written as, Eq.(3):

$$Fe^{3+}_{aq} + H_2O + hv \rightarrow Fe^{2+}_{aq} + HO^{\bullet} + H^{+} \quad (3)$$

The objective of this work is to study the effectiveness of the AOPs in the mineralization of furfural using batch experiments. The AOP selected to carry out this study is the photo-Fenton ($UV/H_2O_2/Fe^{2+}$) process.

2. MATERIALS AND METHODS

2.1 Furfural and Chemicals Used

Furfural commercial grade (Suzhou Alpha International Company, China) was obtained from AL-Dora refinery to simulate the wastewater used in the present experiments. Also **Table 2** shows all the chemicals that used. All the samples were prepared by dissolving requisite quantity in distilled water. The pH of the solution was adjusted by using H_2SO_4 solution.

2.2 Equipment

Batch experiments were carried out in the present work using laboratory scale system, **Fig. 3**, which consist of feed container, peristaltic pump and reactor. The cylindrical reactor is made of stainless steel, 2.4 Litter volume. Irradiation was achieved by using low-pressure mercury vapor lamp, 4-pin single end, 40W, UV-C 254 nm (Philips Company) which was sheathed in glass sleeve for protection and fixed inside along the reactor. The feed container was mounted on a magnetic stirrer with heater (MSH-300N, BOECO. Germany) to maintains the desired temperature and provide a well mixing. Valves 1, 2 and 3 were utilized to control the flow direction through the system. Peristaltic pump (BT300-2J), of medium flow rate 0.07-1140 mL/min from Longer Company, China was used to maintain the desired flow. The pH of solution was monitored using pH meter from (WTW Co., German. INOLAB 720).

2.3 Experimental Procedure

Batch experiments were conducted in the present work to find the best conditions for AOP treatment. The procedure was performed maintaining valve No.1 and No.2 opened and valve No.3 closed, **Fig.3**. For each experiment, simulated furfural wastewater with desired concentration was added to the feed container. A well mixing was maintained using a magnetic stirrer, and the pH value of the solution was adjusted before adding the reagents by adding a dilute H_2SO_4 in the feed container. The desired quantity of Fe^{+2} was added to the feed container and mixed very well. The peristaltic pump was switched on and the solution was allowed to flow from the feed container through the peristaltic pump to the UV reactor, the solution was re-circulated for 5 minutes. The desired quantity of H_2O_2 300-1300 mg/L was added to the feed container, and immediately the UV lamp was turned on. The solution was circulated at a flow rate of 600 mL/min. Regular samples 10ml volume was taken from the feed container after 0, 20, 40 and 60 min for analyses.

2.4 Analysis

Chemical Oxygen Demand of samples was analyzed by COD Photometer system. Appropriate amount of sample (2ml) was introduced into commercially available digestion solution (MR-Rang: 0-1500mg/L) containing potassium dichromate, sulfuric acid and mercuric sulfate. The mixture was then incubated for 120 min at 150^{o}C in a COD reactor (model RD-125, Lovibond Company, Germany). After oxidation was complete, the COD concentration was measured colorimetrically at 605 nm using a DR/2010 spectrophotometer (model MD100, Lovibond, Germany).

3. RESULTS AND DISCUSSION

3.1 The Effect of Initial H_2O_2 Concentration

The effect of initial concentration of H_2O_2 (300, 500, 700, 900, 1100 and 1300 mg/L) on photo-Fenton process was tested to optimize the amount of H_2O_2 required to treat the furfural. Fixed initial amount of Fe^{+2} (40 mg/L) was maintained through the experiments. Initial pH equal to 3 was used and the temperature was maintained at 30^{o}C through all the experiments. Initial furfural concentration 300 mg/L was used in the experiments. **Fig. 4** shows the relation between the removal efficiency and the irradiation time for different initial concentration of H_2O_2. From this figure it can be noticed that the degradation of furfural increased as the concentration of H_2O_2 increased from 300 to 1300mg/L reaching a maximum removal efficiency of 100% at 1300 mg/L after 40 minutes of irradiation time. The mineralization of furfural increased with the increasing of initial concentrations of hydrogen peroxide was related to the fact that the solution was additionally produced hydroxyl radicals for mineralization process as mentioned by many researchers, **Tang, et al., 2011**.

3.2 The Effect of Initial Fe^{+2} Concentration

The amount of Fe^{+2} used in the experiment is one of the critical parameters, which influences the efficiency of photo-Fenton processes and it plays an important role in the minimization of the amount of H_2O_2 dosage. The effect of initial Fe^{+2} concentrations on photo-Fenton process was tested by carrying out experiments with different concentrations of Fe^{+2} (20, 30 and 40 mg/L). The best H_2O_2 concentration (1300 mg/L) from the previous section was used in these experiments. The pH=3, the furfural concentration=300mg/L and the temperature was maintained at 30^{o}C through the experiments. From **Fig. 5** it can be observed that the mineralization rate of furfural increased when Fe^{+2} amount was increased from 20 to 30 mg/L, and the removal efficiency increased from 58.17 % to 100% respectively after about 40 min of irradiation time. At 40mg/L Fe^{+2} the removal efficiency was observed to be 71.33% . This finding is in agreement with the previous observation, **Zhang and Yang, 2011**. The negative effect can be explained as: the addition of ferrous ions increases wastewater turbidity during the photo-treatment, which hinders the absorption of the UV light, required for the photo- Fenton process, excess ferrous ions can react with hydroxyl radical decreasing the attack of hydroxyl radical on organic substrates, also excess ferrous ions can react with OH radical producing compound which inhibit reaction rate, **Dincer et al., 2008**.

3.3 Effect of Initial pH

The photo-Fenton reaction is strongly affected by the pH-dependence. The pH value has a decisive effect on the oxidation potential of hydroxyl radical. Therefore, additional set of experiments were performed to determine the most effective initial pH for the furfural decomposition. Different initial solutions at pH 2, 3 and 7 for H_2O_2 initial concentration of 1300 mg/L were examined, keeping the other parameters and dosage constant (Fe^{+2}=30 mg/L, temperature =30°C, irradiation time =60min and furfural concentration =300 mg/L). **Fig. 6** shows that the mineralization of furfural was significantly influenced by the pH value. The removal efficiency increased when pH increases from pH=2 (63.10%) to pH=3 (100%). Then a decreased in the efficiency was noticed at pH=7 (62.5%) after 60min of irradiation time. The best pH, as observed, was 3 which is in agreement with previous studies using photo-Fenton process, **Tony et al., 2012**.

3.4 Effect of the Initial Furfural Concentration

Pollutant concentration is an important parameter in wastewater treatment, for that a set of experiments with different concentrations of furfural 50, 150 and 300 mg/L were performed. The initial concentration of H_2O_2=1100 mg/L, Fe^{+2}=30 mg/L, pH=3, Temp. =30^oC and irradiation time=40 min. The results were plotted in **Fig. 7**. As noticed from this figures, the removal efficiency increases as the initial concentration of furfural decreases. A complete mineralization of furfural was reached after 20 min of irradiation time for 50 mg/L furfural concentration, while for 150 mg/L a complete mineralization was achieved after 60 min of irradiation time. For 300 mg/L furfural concentration, 94.22 % removal efficiency was reached only after 60 min of irradiation time. This can be explained as: when the concentration of H_2O_2 was fixed throughout these set of experiments, the OH radical that generate in to the photo-Fenton treatment will be more available to attach the furfural molecules in solution of low concentration. This finding is in agreement with the previous observation of, **Tang et al., 2011**.

4. CONCLUSIONS

The main conclusions that can be drawn from the experimental work of this study are as follows:

1- The results indicated that a complete mineralization for $UV/H_2O_2/Fe^{+2}$ system, for furfural concentration of 300 mg/L, was obtained at H_2O_2 = 1300 mg/L, Fe^{+2} = 30 mg/L, pH = 3, Temp. = 30^oC, irradiation time = 60 min.

2- H_2O_2 plays a very important role in the furfural mineralization, high consumption (1300mg/L) of H_2O_2 was required in photo-Fenton system to attain complete mineralization.

3- The best pH value for homogeneous system was found to be equal to 3.

REFERENCES

- ACGIH, 1994, *Documentation of the Threshold Limit Values and Biological Exposure Indices*, 6th ed., American Conference of Governmental Industrial Hygienist, Cincinnati.
- Bolton, J. R., Bircher, K. G., Tumas, W., and Tolman, C. A., 2001, *Figures-of-Merit for the Technical Development and Application of Advanced Oxidation Processes*, Pure Appl. Chem., Vol. 73, No. 4, PP. 627–637.
- Dincer, A. R., Karakaya, N., Gunes, E., and Gunes, Y., 2008, *Removal of COD from Oil Recovery Industry Wastewater by the Advanced Oxidation Processes (AOPs) Based on H_2O_2*, Global NEST Journal, Vol. 10, No. 1, PP. 31-33.
- Fenton,H. J.H., 1894, *Oxidation of Tartaric Acid in Presence of Iron*, Journal of the Chmical Society, transaction, Vol.65,PP.899-910.
- IHS, 2011, *Furfural Report*, IHS Chemical, Chemical Economics Handbook.
- Malato, S., Blanco, J., Vidal, A., Alarcón, D., Maldonado, M.I., Cáceres, J., and Gernjak, W., 2003, *Applied Studies in Solar Photocatalytic Detoxification: An Overview*, Sol. Energy, Vol. 75, PP. 329-336.
- Neyens, E., and Baeyens, J., 2003, *A Review of Classic Fentons Peroxidation as an Advanced Oxidation Technique*, Journal of Hazardous Material B, Vol.98, PP.33-50.
- Oppenländer, T., 2007, *Photochemical Purification of Water and Air: Advanced Oxidation Processes (AOPs): Principles, Reaction Mechanisms, Reactor Concepts*. John Wiley and Sons.
- OSHA, 1994, *Computerized Information System*, Occupational Safety and Health Administration. U.S. Department of Labor.
- Pignatello, J. J, Oliveros, E., and Mackay, A., 2006, *Advanced Oxidation Processes for Organic Contaminant Destruction Based on the Fenton Reaction and Related Chemistry*. Critical Reviews in Environmental Science and Technology, Vol. 36, No. 1, PP. 1-84.
- Sahu, A. K., Mall, I. D., and Srivastava, V. C., 2008, *Studies on the Adsorption of Furfural from Aqueous Solution onto Low-Cost Bagasse Fly Ash*, Chemical Engineering Communications, Vol. 195, PP. 316-335.

- Sulaymon, A. H., and Ahmed, K. W., 2006, *Competitive Adsorption of Furfural and Phenolic Compound onto Activated Carbon in Fixed Bed Column*, Journal of Engineering,Vol.13, PP.1721-1736.
- Tang, X., Guo, Z., Xue, H., Guo, X. and Kang, C, 2011, *Degradation of Furfural by UV/O_3/H_2O_2 Technology*, The 5th International Conference on Bioinformatics and Biomedical Engineering (IEEE). Wuhan, China.
- Tony, M. A., Purcell, P. J., and Zhao, Y. Q., 2012, *Oil Refinery Wastewater Treatment using Physicochemical, Fenton and Photo-Fenton Oxidation Processes*, Journal of Environmental Science and Health , Part A, Vol. 47, PP. 435-440.
- USEPA, 2012, *Furfural Technical*, U. S. Environmental Protection Agency, EPA-75753-2. Washington DC.
- Wang, P., Brenchley, J. E., and Humphrey, A. E., 1994, *Screening Microorganisms for Utilization of Furfural and Possible Intermediates in its Degradative Pathway*, Biotechnology Letters, Vol. 16, No. 9, PP. 977-982.
- Win, D. T., 2005, *Furfural - Gold from the Garbage*. Australian Journal of Technology, Vol. 8, No. 4, PP. 185-190.
- Yaghmaei, S., Asar, R., and Moslehi, P., 2005, *Experimental Comparsion of Two Modification of Activated Sludge for Treatment of Furfural containing Wastewater*, Iranian Journal of Chemical Engineering, Vol. 2, No. 1, PP. 1-9.
- Zhang, Q., and Yang, G., 2011, The Removal of COD from Refinery Wastewater by Fenton Reagent, IEEE Conference (RSETE), China, PP. 7974-7977.

Table 1. Oxidation potentials of some oxidants in volts compared with the normal hydrogen electrode (NHE, E0 = 0V).

Oxidant	**Oxidation Potential (V)**
Fluorine	3.03
Hydroxyl radical ($HO^{\bullet}$)	2.80
Ozone (O_3)	2.07
Hydrogen peroxide (H_2O_2)	1.78
Potassium permanganate ($KMnO_4$)	1.68
Chloride dioxide (ClO_2)	1.5
Chlorine (Cl_2)	1.36
Bromine (Br_2)	1.09

Table 2. List of chemicals used.

Compound	**Formula**	**Vender**	**Assay**
Hydrogen peroxide	H_2O_2	Hopkin and williams	>35 %
Ferrous sulphate	$FeSO_4.7H_2O$	Panreac	99.9 %
Sulfuric acid	H_2SO_4	Riedel-deHaën	97 %
Sodium hydroxide	NaOH	BDH	99%
Acetonitrile HPLC grade	C_2H_3N	Sigma-Aldrich	99.9%

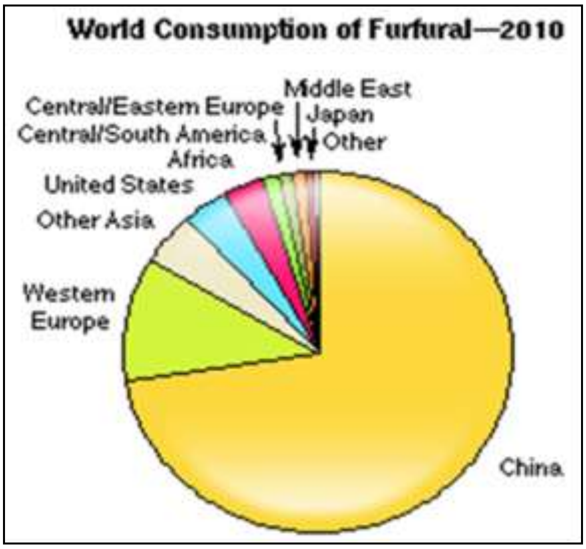

Figure 1. World consumption of furfural at the year 2010.

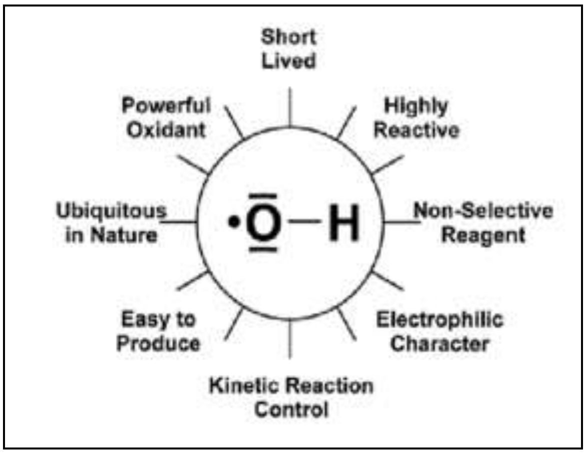

Figure 2. Some characteristics feature of hydroxyl radical.

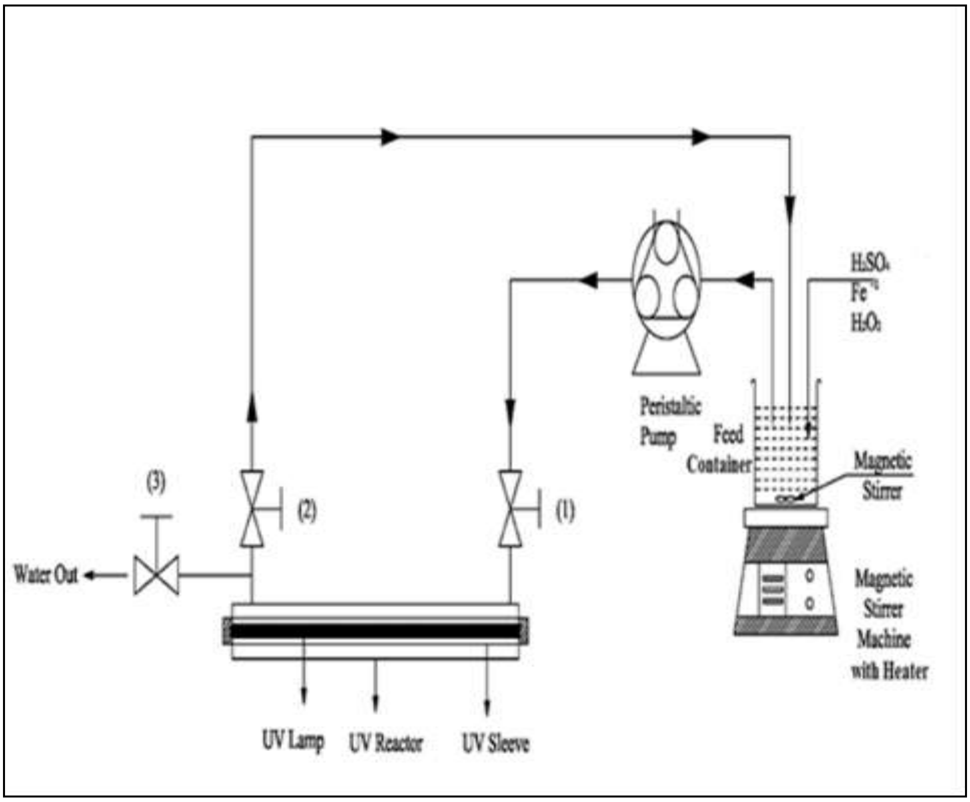

Figure 3. Schematic diagram of AOP system experimental set-up.

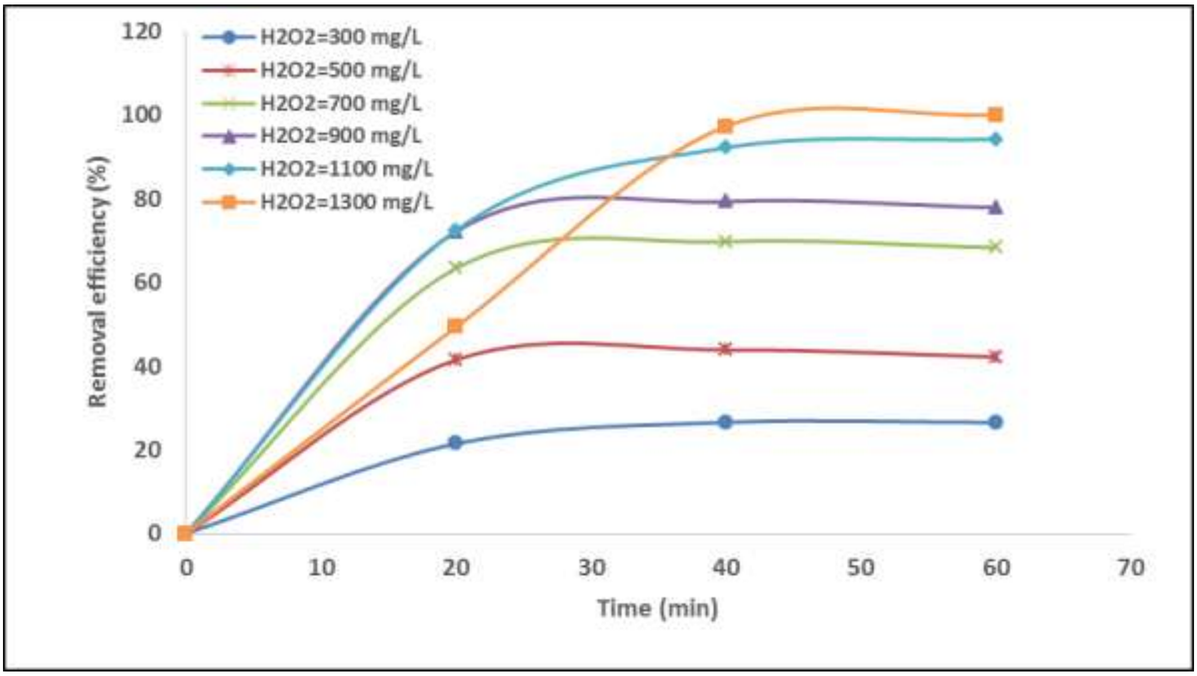

Figure 4. Effect of initial H_2O_2 concentration on the mineralization of furfural by photo-Fenton system at Fe^{+2}=30 mg/L, pH =3, Temp. =30^oC and furfural conc. =300mg/L.

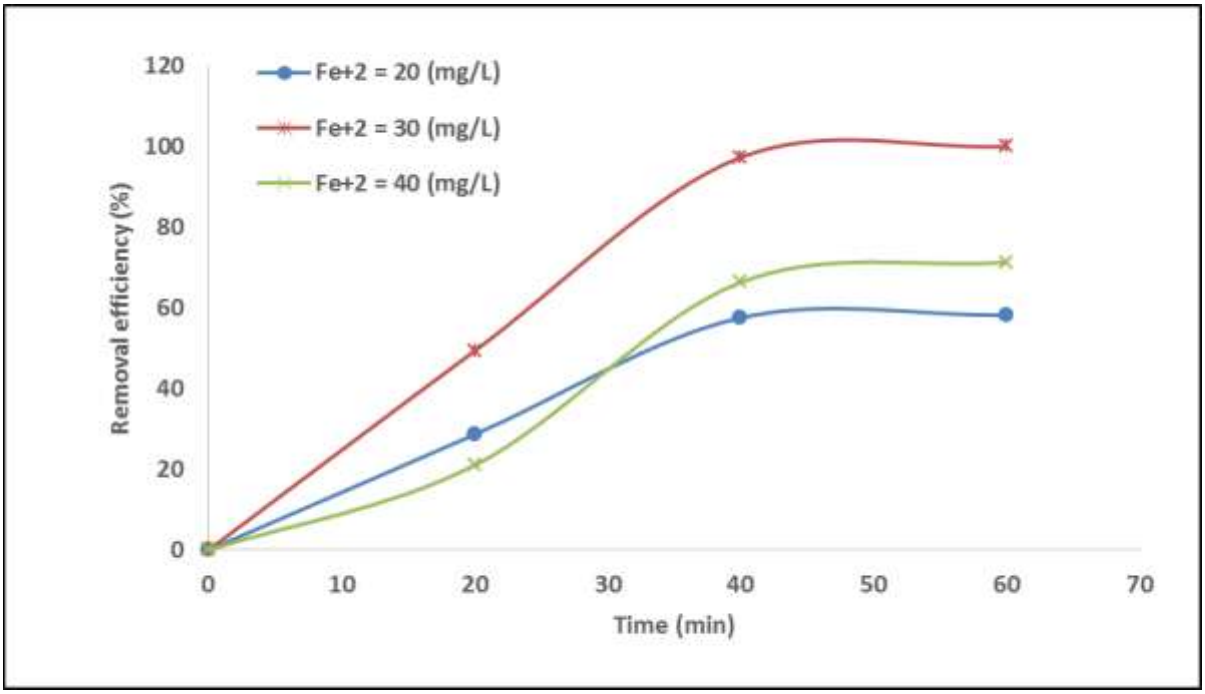

Figure 5. Effect of initial Fe^{+2} concentration on the mineralization of furfural by photo-Fenton system at H_2O_2=1300 mg/L, pH=3, Temp =30°C and furfural conc. = 300 mg/L.

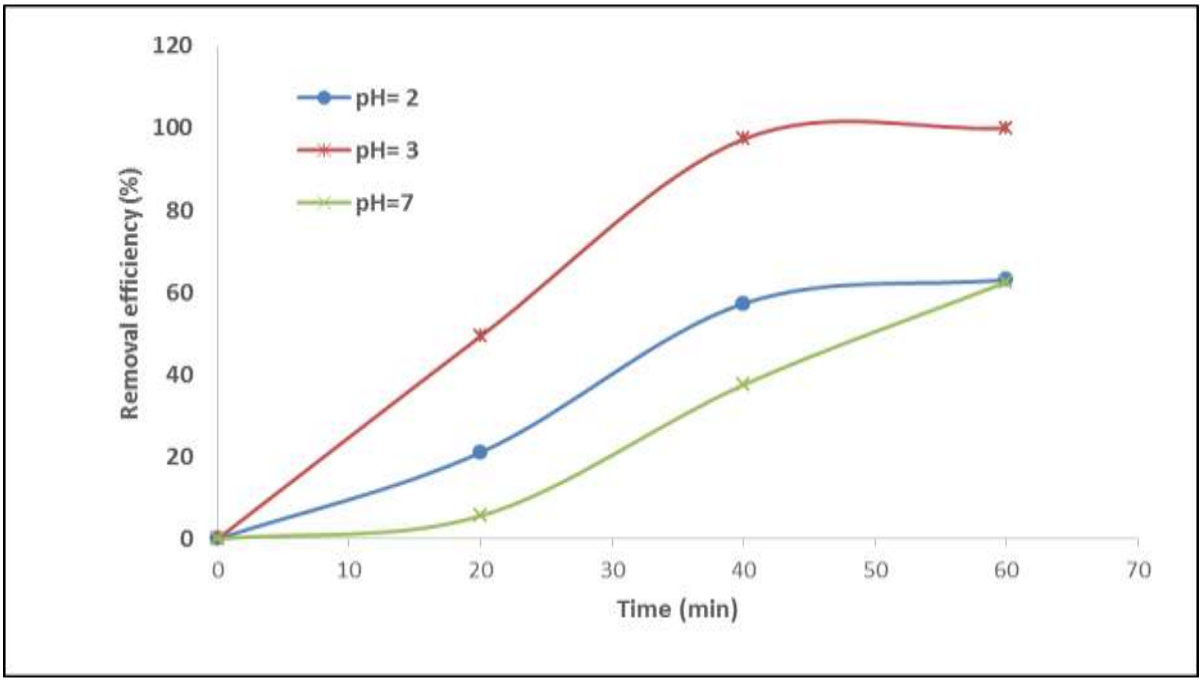

Figure 6. Effect of different pH on mineralization of furfural using photo-Fenton system at H_2O_2=1300 mg/L, Fe^{+2} = 30 mg/L, Temp. =30°C and furfural conc. =300 mg/L.

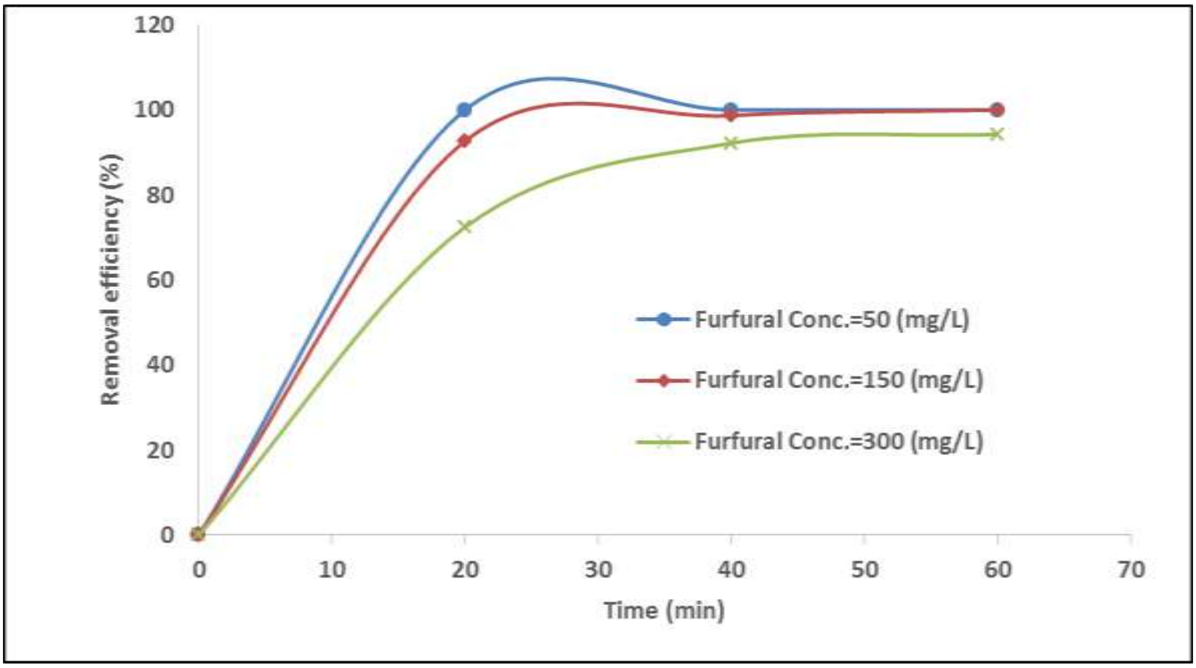

Figure 7. Effect of initial furfural concentrations on the mineralization of furfural by photo-Fenton system at H_2O_2=1100 mg/L, Fe^{+2}=30 mg/L, pH=3 and Temp. = 30^{o}C.

Digital Orthophoto Production Using Close-Range Photographs for High Curved Objects

Fanar Mansour Abed
Assistant Lecturer
College of Engineering- University of Baghdad
fanar.mansou@coeng.uobaghdad.edu.iq

ABSTRACT

Orthophoto provides a significant alternative capability for the presentation of architectural or archaeological applications. Although orthophoto production from airphotography of high or lower altitudes is considered to be typical, the close range applications for the large-scale survey of statue or art masterpiece or any kind of monuments still contain a lot of interesting issues to be investigated.

In this paper a test was carried out for the production of large scale orthophoto of highly curved surface, using a statue constructed of some kind of stones. In this test we use stereo photographs to produce the orthophoto in stead of single photo and DTM, by applying the DLT mathematical relationship as base formula in differential rectification process. The possibilities and the restrictions of the used programs for the extraction of digital surface model & orthophoto production were investigated. The accuracy of the adjusted images using the digital differential rectification package, are checked using 3 check points and the RMSE was computed in 3-dimensions. Conclusions for usefulness and reliability of this test for such special applications were derived.

Key words: photogrammetry, close-range, orthophoto, DLT

انتاج الصور ذات الاسقاط العمودي باستخدام تقنية المسح التصويري ذو المدى القريب لاجسام ذات سطوح معقدة

فنار منصور عبد
مدرس مساعد
كلية الهندسة- جامعة بغداد

الخلاصـــة

ان الصور ذات الاسقاط العمودي تعتبر احد قابليات الوصف الدقيقة والمهمة في الكثير من التطبيقات وخاصة المعمارية وتطبيقات علم الاثار. فعلى الرغم من ان الصور ذات الاسقاط العمودي المستحصلة عن طريق المسح التصويري الجوي سواء كانت الصور المستخدمة ملتقطة من ارتفاعات عالية او واطئة يمكن ان نعتبرها صور مثالية ، الا ان تطبيقات استحصال الصور ذات الاسقاط العمودي من صور ارضية ذات المدى القريب وبمقياس كبير والملتقطة لاهداف تمثل اي نوع من انواع التماثيل او التحف الفنية (كالقطع الاثارية مثلا) ، لا تزال تحتاج الى الكثير من التجارب والمحاولات الخاصة بمسالة دقة مواقع النقاط على هذه الاهداف. ولهذه الاسباب تم اعداد هذا البحث والمتمثل بانتاج صورة ارضية ذات اسقاط عمودي وبمقياس كبير لهدف يتكون من نوع من انواع التماثيل والمصنوع من احد انواع الاحجار والذي يتميز بسطحه الحاوي على

الكثير من المعالم الحادة والكثيرة الانحناءات وذلك من خلال التقاط صورتين للهدف (يمنى ويسرى) من على بعد مناسب للحصول على منطقة تداخل بين الصورتين من اجل الحصول على البعد الثالث. ان الية العمل في هذا البحث اعتمدت على استخدام زوج الصور في انتاج الصورة ذات الاسقاط العمودي بدلا من الطريقة الشائعة والمتمثلة في استخدام صورة واحدة وDTM. حيث تم العمل في هذا البحث من خلال تطبيق الموديل الرياضي للتقويم التفاضلي بالاعتماد على التحويل الخطي المباشر (DLT).

الكلمات الرئيسية: المسح التصويري, المدى القريب, الصور ذات الاسقاط العمودي, معادلات التحويل الخطي

1. INTRODUCTION

Orthophotography is a powerful tool for aerial photogrammetric applications, already tested with excellent results, cost effective and extremely flexible in its digital version ,loannidis, et al., 2003. In terrestrial and especially in close-range applications digital rectification and the development of mathematically developable surfaces are mostly applied when stereoscopic photogrammetric procedures are used. In architectural and especially in archaeological applications, however, one is very often faced with surfaces, one which these procedures cannot be applied, while at the same time the desired result is an image ,**Hemmleb, 2002**. In this case the production of an orthophotography seems to be the only solution, capable of providing reliable and accurate results.

The idea for carrying out this test described in this article was the investigation of the undisputed possibilities presented and the problems which arise when applying orthophoto techniques in difficult cases of geometric documentation of monuments and any other applications in archaeological field. It goes without saying that this particular product is extremely valuable, especially as coverage of a Spatial Information System. The investigation in this test concerns the possibilities of producing satisfactory results for close-range archaeological applications on highly curved objects, using a package of digital differential rectification that is based on Direct Linear Transformation (DLT) equations.

2. PROCEDURES OF THE WORK

2.1 Field Work

The used target was some kind of statues that have been chosen because of its high curved surface with tiny details having 15 marked points on it, to be the control points, see **Fig.1** These points were circles with diameter of 0.5mm, have been lately computed very accurately in 3-dimensions using T2 theodolite with its accessories and steel tape. These points includes 3 check points that used later to find the RMSE.

The structure of the field work was:-

- Creating a base line (AB between two very accurate ground points A & B) far away from the target about 1.735m vertical from the middle.
- Observed the points on the target from stations A&B and record both horizontal and vertical angles, using sets for high accuracy.

- Compute the X&Y ground coordinates for the 15 points using intersection I and also compute the height (Z) of these points by sum the vertical distance to the height of instrument, see **Table 1**.
- Taking the left and right photos to the target from different stations (C & D), see **Fig.2** using a non metric digital camera (Fujitech, 5.1 megapixels) mounted on a level tript in front of the target. The specifications of the digital camera are listed in **Table 2**.

2.2 Geometric Correction of Digital Images

Geometric errors and displacements in digital images are caused by the characteristics of the acquisition process and the geometric characteristics of the object being imaged. These geometric corrections consist of two steps:

1. Model the geometric errors in the image by an appropriate mathematical formula. This formula can be either:
   - A rigorous mathematical model describing the relationship between the image and the ground, in our case Direct Linear Transformation (DLT) formula have been used which represented by the differential rectification process.
   - An empirical relationship such as 1^{st} through n^{th} order polynomial equations which do not model the true geometric relationships between the image and the ground, this is represented by the polynomial rectification process.
2. Resample the image by computing a new image with the pixels in known positions and known dimensions, such that the image will represent the correct geometry of the object. Resampling produces a new data set from an existing old one. It usually involves both geometric and intensity domains. Resampling comprises two basic stages :
   - Calculation of the new pixel locations.
   - Interpolation of the corresponding intensity levels from the neighboring old pixels.

2.2.1 Differential rectification

In the case of digital differential rectification, each pixel is separately transferred from the original image to the resulting image using the indirect approach (from ground to image). A Digital Train Model (DTM) is needed to correct for relief displacements in the image. It is assumed that the DTM is stored in the same format as the digital image, which in this case expresses elevations instead of densities. In general case, digital differential rectification is done using one image and existing DTM in the following manner:

Measuring the digital image coordinates (column, row) for control points where corresponding ground control coordinates of these measured image coordinates are input and used to solve the DLT formula. A least squares solution is employed to include any number of redundant measurements and assess the quality of the solution matrix. The DEM is then interpolated to produce coordinated ground point locations at required intervals. Rectified image coordinates corresponding to these ground point locations are then computed using the inverse condition of DLT. The final step is to compute the gray value for each pixel by interpolation using one of the resampling methods. The density is stored at the X,Y location of digital orthophoto.

In this paper we did not use the DTM for our study spot; therefore we used a method for digital orthophoto production which depends on the use of stereo pair images instead of the use of one image and DTM.

2.2.2 Direct linear transformation (DLT)

Among the approaches particularly suitable for non-metric photography is the Direct Linear Transformation (DLT) approach. The solution is based on the concept of direct transformation from image coordinates into object-space coordinates, thus by passing the traditional intermediate step of transforming image coordinates from machine system to photo system, ,**Sharki, 2002**. The method is based on the following pairs of equations:

$$x+\frac{L_1X+L_2Y+L_3Z+L_4}{L_9X+L_{10}Y+L_{11}Z+1}=0 \qquad \ldots.(1)$$

$$y+\frac{L_5X+L_6Y+L_7Z+L_8}{L_9X+L_{10}Y+L_{11}Z+1}=0 \qquad \ldots.(2)$$

Where:

x & y are the measured digital image coordinates
X, Y & Z are the object space coordinates
L_1 to L_{11} are eleven unknown constants

If we added for Eqs. (1) and (2) the errors due to the optical and de-centering distortion, they become:

$$(x+\Delta x)+\frac{L_1X+L_2Y+L_3Z+L_4}{L_9X+L_{10}Y+L_{11}Z+1}=0 \qquad \ldots.(3)$$

$$(y+\Delta y)+\frac{L_5X+L_6Y+L_7Z+L_8}{L_9X+L_{10}Y+L_{11}Z+1}=0 \qquad \ldots.(4)$$

Where:

$$\Delta x=x\left(L_{12}r^2+L_{13}r^4+L_{14}r^6\right)+L_{15}\left(r^2+2x^2\right)+2L_{16}yx \qquad \ldots.(5)$$

$$\Delta y=y\left(L_{12}r^2+L_{13}r^4+L_{14}r^6\right)+2L_{15}xy+L_{16}\left(r^2+2y^2\right) \qquad \ldots.(6)$$

$$r^2=x^2+y^2 \qquad \ldots.(7)$$

L_{12} to L_{14} are the coefficients of optical distortion
L_{15} & L_{16} are the coefficients of de-centering distortion

By substituting the values of $\Delta x \,\&\, \Delta y$ to Eqs. (3) and (4), simplified and re-arranged, we obtain:

$$x = L_1 X + L_2 Y + L_3 Z + L_4 - xL_9 X - xL_{10} Y - xL_{11} Z - xL_{12} r^2 R - xL_{13} r^4 R - xL_{14} r^6 R - \left(L_{15}\left(r^2 + 2x^2\right)\right)R - 2L_{16} xyR \quad \text{....} \quad (8)$$

$$y = L_5 X + L_6 Y + L_7 Z + L_8 - yL_9 X - yL_{10} Y - yL_{11} Z - yL_{12} r^2 R - yL_{13} r^4 R - yL_{14} r^6 R - 2L_{15} xyR - L_{16}\left(r^2 + 2y^2\right)R \quad \text{....} \quad (9)$$

Where:

$$R = L_9 X + L_{10} Y + L_{11} Z + 1 \quad \text{....} \quad (10)$$

To obtain the DLT parameters using the least square method, we have to solve Eqs. (8) and (9) in matrix form.
In this test we used the 15 ground points to solve the 16 parameters, so, each point gives 2 equations and the total number of equations will be 30 equations. At first we measured the digital coordinates of these points on both photos , see **Table 3.** then by solving these equations using L.S. we gain the parameters listed below:

LEFT PHOTO:-

$L_1 = -0.00300897657871246$

$L_2 = 0.0892554074525833$

$L_3 = -0.205902293324471$

$L_4 = 1.0034114074707$

$L_5 = 0.137721985578537$

$L_6 = -0.135213151574135$

$L_7 = -0.106498301029205$

$L_8 = -8.93060302734375$

$L_9 = -0.000532188263605349$

$L_{10} = -4.21748918597586E-005$

$L_{11} = -0.00145815122232307$

$L_{12} = -8.71862795293055E-007$

$L_{13} = 2.88788825887837E-013$

$L_{14} = -3.25629802096636E-020$

$L_{15} = -1.093368337024E-005$

$L_{16} = -4.72695683129132E-006$

RIGHT PHOTO:-

$L_1 = -0.2379578637332$
$L_2 = 0.071085112169385$
$L_3 = -0.201956253498793$
$L_4 = 2.17296390533447$
$L_5 = -0.147681787610054$
$L_6 = 0.0615520495921373$
$L_7 = -0.129928223788738$
$L_8 = 1.36469879150391$
$L_9 = -0.00120378778683516$
$L_{10} = 0.000344896406204498$
$L_{11} = -0.000825379638627055$
$L_{12} = -1.56502965609207E-006$
$L_{13} = 6.52899424723684E-013$
$L_{14} = -9.84681762699648E-020$
$L_{15} = 0.000101436824479606$
$L_{16} = 5.93337208556477E-005$

2.2.3 Preparation of (TIN) for the study spot

Most of the previous works in the field of digital orthorectification depend upon the standard DTM, ,**Mikhail et al., 2001**. In this work, a method of preparing Triangulated Irregular Network (TIN) is presented. This method is done through two steps:
The first step: is the matching between the two images, using manual matching in this case, by selecting 35 dispersed points on the target and record the digital coordinates of these points for both left & right photos, the distribution of these points on the target is shown in **Fig.3** and the digital coordinates (column,row) of these points are listed in **Table 4**.
The second step: is computing the ground coordinates of these matched points, and this is done using the following equations:

$$(L_1 + x_i L_9)X_i + (L_2 + x_i L_{10})Y_i + (L_3 + x_i L_{11})Z_i + x_i + L_4 = 0 \quad \text{…. (11)}$$

$$(L_5 + y_i L_9)X_i + (L_6 + y_i L_{10})Y_i + (L_7 + y_i L_{11})Z_i + y_i + L_8 = 0 \quad \text{…. (12)}$$

Having computed the eleven unknowns coefficients (L_1 to L_{11}) for each one of the two photos, the object-space coordinates of any object point which is imaged in both photos can be computed using the above equations. So, if there is ground point A and its image appears in two photos, where a1 is the image of A in the left photo and a2 is the image of A in the right photo, two equations of the form (11 and 12) can be written for point a1 and two more for point a2. This yields a system of four equations which contain only three unknown that are the ground coordinates of point A, (X,Y&Z). The values of X,Y&Z are computed in a L.S. solution. Depending upon this procedure the ground coordinates of matching points (TIN) are computed for later use.

2.2.4 Interpolation process

In this step, the elevation Z of the desired point must be interpolated from the surrounding data, and this is done by using the bilinear polynomial. The general form of this polynomial is ,**Ahmed, 1999**.

$$Z = a_0 + a_1 X + a_2 Y + a_3 XY \qquad \text{…. (13)}$$

Ground coordinates (X,Y & Z) of the matching points that have been computed in the previous section, are often called (as mentioned before) Triangulated Irregular Network (TIN). TIN is used here directly to find the elevation value (Z) for each pixel of the orthophoto, and this is done by interpolation process using multi-surfaces of bilinear polynomial equation Z=f(X,Y), for representing the study spot, depending on the ground coordinates of matching points.

The solution of this polynomial is by standard L.S. method. The calculated coefficients of the polynomial equations are used to find the elevation Z at each pixel ground (X,Y) of the orthophoto region. After that, these calculated ground coordinates (X,Y,Z) for each pixel in the orthophoto and the previously calculated parameters (L_1 to L_{11}) are used in the DLT Eqs. (1) and (2) to compute corresponding digital image coordinates directly then interpolate the gray value.

2.2.5 Resampling

One of the digital images (left image in our case) can now be transformed into an orthophoto. It is necessary to find the gray value for each pixel in the orthophoto as a final step, and this is done by interpolation the intensity levels for the new pixel locations from the neighboring old pixels using one of the following resampling methods, **Habib, 2004.** and **,Wolf & Dewitt, 2000.**

1. Nearest neighbor

Uses the value of the closest pixel to assign to the output pixel value.

2. Bilinear interpolation

Uses the data file values of four pixels in a 2*2 window to calculate an output value with bilinear function.

3. Cubic convolution

Uses the data file values of sixteen pixels in a 4*4 window to calculate an output value with a cubic function.

Cubic convolution interpolation is the best of these resampling methods, and for that reason we used this method in our case, applying the following equation in computing the gray value for each new pixel, (for understanding the equation below, seek for help using **Fig.**

$$g = g_{11}r_1c_1 + g_{12}r_1c_2 + g_{13}r_1c_3 + g_{14}r_1c_4 +$$
$$g_{21}r_2c_1 + g_{22}r_2c_2 + g_{23}r_2c_3 + g_{24}r_2c_4 +$$
$$g_{31}r_3c_1 + g_{32}r_3c_2 + g_{33}r_3c_3 + g_{34}r_3c_4 +$$
$$g_{41}r_4c_1 + g_{42}r_4c_2 + g_{43}r_4c_3 + g_{44}r_4c_4 \quad \text{…. (14)}$$

Where:

g's are the intensity values of old pixels
r's are the rows
c's are the columns

The final orthophoto is represented in fig. 5

3. ACCURACY

The accuracy test was carried out in the middle of the processes of our final product, using 3 check points whose coordinates were determined with very high accuracy with terrestrial methods. After we compute the coordinates of these check points as mentioned in section (2.2.3) we compute the R.M.S.E. in 3-dimensions and the following deviations we obtained:

R.M.S.E. in X direction = 10.887 mm.
R.M.S.E. in Y direction = 8.302 mm.
R.M.S.E. in Z direction = 12.546 mm.

4. CONCLUSIONS

Carrying out comparative tests for the accuracy and functionality of the production procedures of digital orthophotos from aerial imagery established their usage in a wide range of applications. The use of orthophoto from close-range photos with high curved surfaces in architectural and archaeological applications has not been yet taken the range of hoping studies in investigate a lot of considerations that concerned with final accuracy to be achieved. I hope this paper be one of these papers that deals with some negligible cases in close-range photogrammetry and gained the hopeful results.

REFERENCES

- ,Ayman F. Habib, 2004. *Image registration & rectification*, Internet document,.

- ,C. loannidis, P. Pappa, S. Soile, E. Tsiliggiris and A. Georgopoulos, 2003, *Orthophoto Production Comparision Test for Close-Range Applications*.

- ,Edward M. Mikhail, James S. Bethel & J. Chris Mcglone, 2001, *Introduction to Modern Photogrammetry*, 1st edition.

- ,Maitham Mutasher Sharki, 2002, *Accuracy Assessment of Digital and Analytical Close-Range Photogrammetric Techniques*, MSc., Thesis, Baghdad University.

- ,Matthias Hemmleb, 2002, *Digital Rectification of Historical Images*, Internet document,.

- ,Paul R. Wolf and Bon A. Dewitt, 2000, *Elements of Photogrammetry with Applications in GIS*", 3rd edition,.

- ,Shaker Farhan Ahmed, 1999, *Automatic Production of Digital Orthophoto*, MSc. Thesis, Baghdad University.

\+ control points
Θ check points

Figure 1. The target showing the position of 15 marked points.

Table 1. Ground control points for target points (field work).

Point	Type	X m.	Y m.	Z m.
1	check	501.924178	500.880956	51.259153
2	control	501.921455	500.862285	51.243883
3	control	501.945059	500.895585	51.247527
4	control	501.948533	500.866530	51.221669
5	control	501.949258	500.881047	51.226763
6	control	501.947706	500.885826	51.199257
7	control	501.944425	500.856190	51.181453
8	control	501.931662	500.851477	51.194789
9	control	501.943788	500.861170	51.172069
10	check	501.928334	500.856569	51.164549
11	check	501.949616	500.870282	51.152067
12	control	501.933537	500.862130	51.140041
13	control	501.920173	500.836603	51.119302
14	control	501.934250	500.885378	51.117134
15	control	501.920305	500.866149	51.103992

Table 2. Digital camera specifications.

Sensor	5.1 megapixel CMOS
Lens	F 2.8 ~ 8.47
Built-in view finder	Field of view: 85%
Focus range	Normal: 100cm ~ infinity Macro: (w) 20cm
Sensitivity	Auto , 100 , 200 , 400
LCD display	1.5" color TFT LCD panel
Still image resolution	2560 x 1920 , 2048 x 1536 , 1024 x 768
Still image quality	Fine: 7x compression rate Normal: 10x compression rate
Exposure control	Auto & manual
Shutter control	Mechanical shutter , shutter speed: 1/2 -1/6458 sec. with CCD variable electronic shutter
Digital zoom	4x
Image file format	JPEG compression
Picture storage	Internal: 16 MB embedded Nandgate flash memory External: SD memory card / MMC
Communication interface	USB 1.1
Power supply	AAA-size alkaline batteries x 4 Rechargeable Ni-MH batteries (min.550mAh/1.2V)
Dimensions	Camera body: 97 x 28 x 63 mm
Weight	Camera body without battery: 110 g

Left photo

Right photo

Figure 2. The left and right photos for the target.

Table 3. Digital coordinates of ground control points.

Point	Left Photo		Right Photo	
	column	row	column	row
1	1362.67	418.67	1102.00	492.00
2	1398.00	508.67	1172.67	566.00
3	1226.00	484.00	1009.33	564.00
4	1292.67	620.00	1115.33	678.67
5	1230.67	591.33	1047.33	659.33
6	1266.00	721.33	1036.67	778.67
7	1328.00	807.33	1152.67	857.33
8	1396.67	747.33	1219.33	792.00
9	1307.33	856.67	1121.33	902.67
10	1413.33	876.67	1200.00	916.67
11	1285.33	955.33	1079.33	992.00
12	1364.00	1008.00	1136.00	1042.67
13	1451.33	1084.00	1256.00	1132.67
14	1297.33	1128.00	1032.67	1151.33
15	1414.00	1179.33	1145.33	1206.67

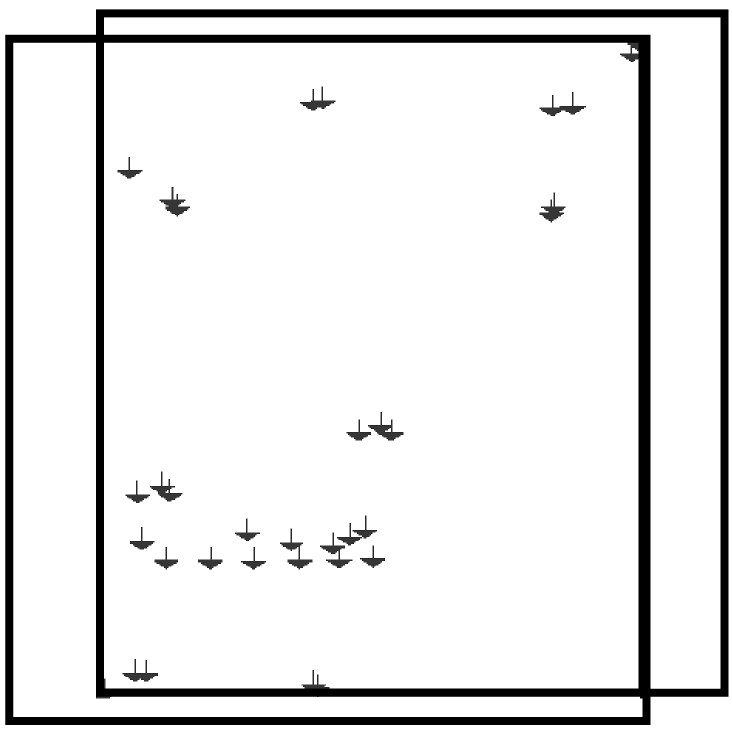

Figure 3. The distribution of matching points on the target.

Table 4. Digital coordinates of matched points.

Point	Left Photo		Right Photo	
	column	row	column	row
1	1182.00	102.67	1028.00	223.33
2	1188.00	102.00	1030.00	210.00
3	1346.00	113.33	1163.33	193.33
4	1343.33	121.33	1172.00	196.00
5	1210.67	151.33	1150.67	242.67
6	1218.67	150.67	1156.67	241.33
7	1357.33	482.00	1104.67	550.67
8	1326.67	491.33	1076.00	564.00
9	1370.00	505.33	1128.67	570.00
10	1294.00	517.33	1058.00	590.00
11	1381.33	524.00	1154.00	587.33
12	1216.00	493.33	1001.33	574.67
13	1212.67	615.33	1028.67	682.67
14	1236.67	618.67	1050.00	685.33
15	1230.67	638.67	1036.00	704.00
16	1376.67	776.00	1198.00	820.00
17	1400.67	776.33	1217.33	820.67
18	1392.67	794.67	1201.33	838.00
19	1206.67	1457.33	880.00	1438.67
20	1238.67	1380.67	919.33	1373.33
21	1242.00	1361.33	922.00	1357.33
22	1521.33	1364.00	1176.00	1384.00
23	1519.33	1346.67	1174.67	1368.67
24	1342.67	1634.00	919.33	1610.00
25	1350.00	1639.33	906.67	1613.33
26	1520.00	1619.33	1080.00	1621.33
27	1535.33	1624.00	1071.33	1627.33
28	1579.33	1761.33	1117.33	1763.33
29	1584.67	1788.67	1120.00	1791.33
30	1362.00	446.00	1104.00	519.33
31	1332.67	444.00	1075.33	520.67
32	1298.67	443.33	1046.00	524.00
33	1266.67	444.00	1024.00	526.00
34	1234.00	444.67	1007.33	528.67
35	1387.33	448.67	1136.67	518.67

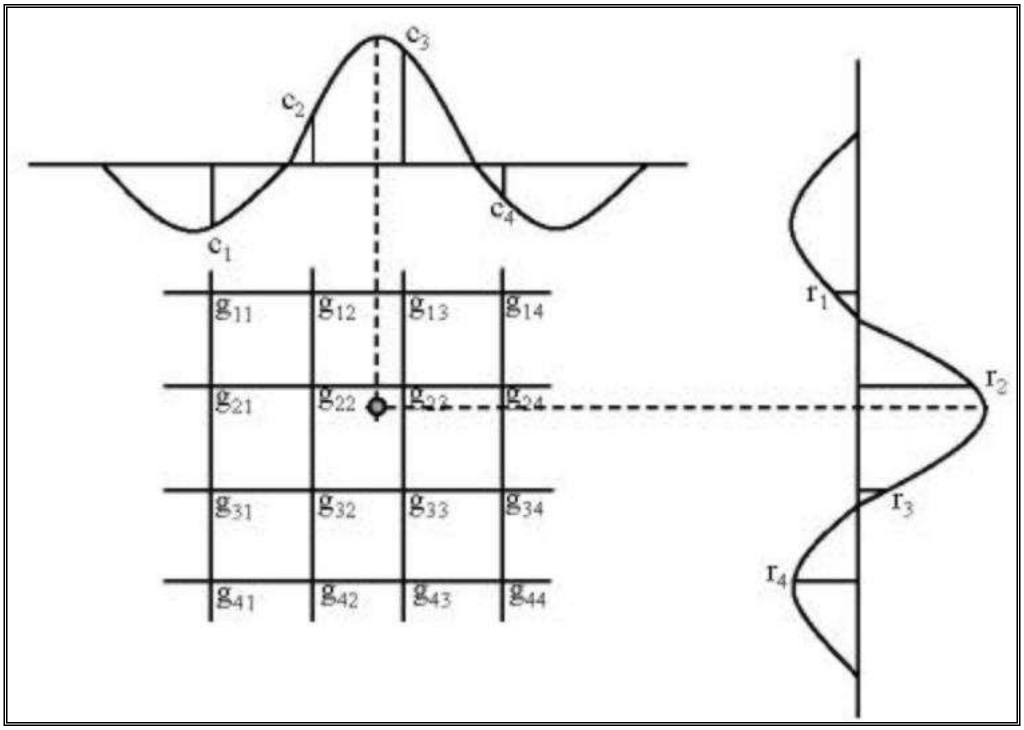

Figure 4. Bicubic convolution.

Figure 5. Digital orthophoto of case study.